LPI SUMMER INTERN PROGRAM IN PLANETARY SCIENCE

2018

Papers Presented at the

34th Annual Summer Intern Conference

August 9, 2018 — Houston, TX

LPI

NASA

USRA

Papers Presented at the

Thirty-Fourth Annual Summer Intern Conference

August 9, 2018
Houston, Texas

2018 Summer Intern Program for Undergraduates
Lunar and Planetary Institute

Sponsored by
Lunar and Planetary Institute
NASA Johnson Space Center

LPI Contribution No. 2110

Compiled in 2018 by

Meeting and Publication Services
Lunar and Planetary Institute
USRA Houston
3600 Bay Area Boulevard, Houston TX 77058-1113

The Lunar and Planetary Institute is operated by the Universities Space Research Association under a cooperative agreement with the Science Mission Directorate of the National Aeronautics and Space Administration.

HIGHLIGHTS

Special Activities

Date	Activity	Location
June 4	Lunar Curatorial and Stardust Lab Visit	NASA JSC
June 28	Meteorite Lab Visit	NASA JSC
July 20	Robotics Systems Technology Branch Visit	NASA JSC
July 20	Human Exploration Research Analog (HERA)	NASA JSC
July 20	Neutral Buoyancy Laboratory (NBL)	Sunny Carter Training
Aug 1	Orion, Crew Dragon and CST-100 Starliner Mock-up	NASA JSC
Aug 1	Ascent Abort-2 (AA-2)	NASA JSC
Aug 3	Modular Robotic Vehicle (MVR)	NASA JSC

LPI Summer Intern Program 2018 — Brown Bag Seminars

Wednesdays, 12:00 noon – 1:00 p.m., Lunar and Planetary Institute

Date	Speaker	Topic	Location
June 6	Liz Rampe	MSL Mission	Hess Conference Room
June 13	Kevin Righter	Osiris Rex Mission	Hess Conference Room
June 20	David Kring	From the Earth to the Moon	Hess Conference Room
June 27	Cyrena Goodrich	Meteorites	Hess Conference Room
July 6	Interns	Mid-Term Reports	Hess Conference Room
July 11	Walter Kiefer	Terrestrial Planet Interiors and Insight	Hess Conference Room
July 18	Edgard Rivera-Valentin	Astrobiology: "Follow the Water"	Hess Conference Room
July 25	Nicholas Castle	Small Body Differentiation: Conflicting Views from the HED Meteorites	Hess Conference Room
August 1	Justin Simon	Heat Pipe Planets	Hess Conference Room
August 8	Julie Stopar	LROC Views of Lunar Volcanism	Hess Conference Room

LPI Summer Intern Tag Up and Science Fiction Film Series

Thursdays, 6:30 p.m., Lunar and Planetary Institute

Date	Title	Location
June 6	The Martian	Hess Conference Room
June 15	Apollo 13	Hess Conference Room
July 12	October Sky	Hess Conference Room
July 18	Interstellar	Hess Conference Room
July 25	Contact	Hess Conference Room

LPI Summer Intern Professional Development Seminar Series

12:00 noon – 1:00 p.m., Lunar and Planetary Institute

Date	Speaker	Topic	Location
July 6	Christine Shupla	Communications, Time Management, Commitment, and Respect	Hess Conference Room
July 12	Christine Shupla	Ethics in Science	Hess Conference Room
July 31	Christine Shupla	How to Give a Science Talk	Hess Conference Room
Aug 3	Christine Shupla	Discussing Issues for Marginalized Communities in STEM with Interns	Berkner Conference Room
Aug 6	Christine Shupla	Applying to Grad School	Hess Conference Room

AGENDA

8:00 a.m. Breakfast

8:25 a.m. Introductory Remarks by Drs. Louise Prockter, Allan Treiman, and David Draper

8:30 a.m. **NICHOLAS WAGNER, Colorado School of Mines**
Advisors: Jonathan Kay and Paul Schenk
The Orientation of the Bladed Terrain Feature in Tarturus Dorsa, Pluto and Possible Reorientation of Pluto **[#4001]**

8:50 a.m. **ANDY LÓPEZ-OQUENDO, University of Puerto Rico**
Advisor: Edgard Rivera-Valentín
Constraints on Crater Formation Ages on Dione from Cassini VIMS and ISS **[#4005]**

9:10 a.m. **MITZI CRUZ QUIJANO, Universidad Autonoma del Estado de Hidalgo**
Advisors: Jonathan Kay and Louise Prockter
Location and Degradation State of Chaos Across Europa: Is There Old Chaos? **[#4006]**

9:30 a.m. **ALEXANDER HOLMWOOD, Hamilton College**
Advisor: Kevin Righter
Mineralogy and Petrology of Dark Clasts in Polymict Eucrites **[#4004]**

9:50 a.m. **DEVIN McQUAIG, University of Houston**
Advisors: Justin Simon, David Mittlefehldt and Rosalind Armytage
Potassium-Feldspar Bearing Main Group and Stannern Group Eucrites: Petrographical and Geochemical Investigations of Mafic Crust Formation Processes on Vesta **[#4014]**

10:10 a.m. **YOANA BOLEAGA, City College of New York**
Advisor: Cyrena Goodrich
Xenolithic Fe,Ni Metal in Polymict Ureilite Meteorites **[#4008]**

10:30 a.m. Break

10:40 a.m. **ETHAN KUEHL, Washington University in St. Louis**
Advisors: Nicolas Castle and John Jones
Petrology and Geochemistry of Lithic Fragments in Elephant Moraine 79001 **[#4011]**

11:00 a.m. **FEDERICO STACHURSKI, University of Glasgow**
Advisor: Yang Liu and Allan Treiman
Water Content and Mineral Abundance at Gale Crater, Mars as Inferred from OMEGA and CRISM Observations **[#4012]**

11:20 a.m. **NATHAN HADLAND, Florida Institute of Technology**
Advisors: Valerie Tu and Liz Rampe
Acidic Dissolution of Phosphate-Rich and Phosphate-Poor Basalts: Implications for the Stimson Sandstone Unit, Gale Crater **[#4003]**

11:40 a.m. **JACOB OTT, Harvard University**
Advisors: Liz Rampe, Allan Treiman, and Richard Morris
Chemistry and Crystallography of Diagenetic and Authigenic Potassium Feldspar: Implications for Sedimentary Petrology in Gale Crater, Mars **[#4013]**

12:00 p.m. Lunch

1:00 p.m. **STEPHEN SLIVICKI, University of Wisconsin, River Falls**
Advisors: Martin Schmieder and David Kring
Petrologic Analysis of Green-Black Impact Melt Breccia with a History of Hydrothermal Alteration at Chicxulub **[#4002]**

1:20 p.m. **ELISHA JHOTI, University of Edinburgh**
Advisor: Yang Liu
LRO LAMP Far Ultraviolet Investigation of Cold Spots and a New Impact Crater on the Moon **[#4009]**

1:40 p.m. **HANNAH O'BRIEN, University of Notre Dame**
Advisors: Katharine Robinson and David Kring
Tracing a Lunar Magmatic Epoch Through Apollo 14 Samples **[#4015]**

2:00 p.m. **FRANK WROBLEWSKI, Northland College**
Advisors: Allan Treiman and Sriram Bhiravarasu
Anomalous Radar Properties at Venus' Mountaintops: Refined Spatial Resolution from Stereo Altimetry **[#4007]**

2:20 p.m. Adjourn

CONTENTS

XENOLITHIC FE,NI METAL IN POLYMICT UREILITE METEORITES. Y. Boleaga[1] and C.A. Goodrich[2]. [1]Department of Geology, The City College of New York (City University of New York), 160 Convent Ave, New York, NY 10031. [2]Lunar and Planetary Institute, USRA-Houston, Houston, TX 77058.

Introduction: Ureilite meteorites are ultramafic rocks that come from the mantle of a differentiated asteroid. They are the second largest achondritic meteorite group and are olivine and pyroxene dominant with smaller abundances of elemental carbon, sulfide and metal [1-4]. In this study we are focusing on polymict ureilites. Polymict ureilites are breccias that represents regolith on a ureilitic asteroid [3-6]. They contain xenoliths from impactors that come from several types of asteroids and include fragments of ordinary chondrites, enstatite chondrites, carbonaceous chondrites, Rumuruti-type chondrites, and angrites.

In this study, we searched for xenoliths of iron meteorites in polymict ureilites. Xenoliths of iron meteorites have not previously been reported in polymict ureilites. An absence of such metal materials could mean that silicate materials preferentially survive during impacts due to their physical properties compared with those of metal. Alternatively, iron meteorite asteroids may not have been present where and when ureilitic regolith was forming.

The importance in identifying Fe,Ni metal in our sections led us to study the distribution of Fe,Ni-rich grains and their associated assemblages in polymict ureilites NWA 10657 and DaG 999. Our preliminary data are presented in this research.

Methods: We studied polymict ureilite sections NWA 10657 and DaG 999. Reflected light microscopy at the Lunar and Planetary Institute (LPI) was used to identify possible study areas in both thin sections. Using the JEOL 8530F field emission electron microprobe (EMPA) at Johnson Space Center (JSC), x-ray element maps (Al, C, Ca, Cl, Cr, Fe, K, Mg, Na, Ni, O, P, S, Si, and Ti) of section DaG 999_r2 were collected by energy dispersive spectroscopy (EDS). X-ray element maps of section NWA 10657_003 had previously been obtained by Goodrich. The JEOL 8530F was also used for identification of internal textures of metal using back-scattered electron images (BEI). Minerals were identified using EDS. Mineral compositions were obtained using quantitative wavelength dispersive spectroscopy (WDS). Natural and synthetic metals, sulfides, silicates, and oxides were used as standards. For analysis of metals and sulfides, Fe, Ni, Co, Cr, P, Si, S and Mg were routinely measured. EMPA of metal and sulfides was conducted at 40 nA beam current and 15 keV accelerating potential.

Photoshop was used to combine 40 reflected light images taken from DaG 999_r2 (Fig. 1). Excel was used to process the analyses from the electron microprobe. ImageJ software was used to process and combine X-ray maps. Origin was used for graph plotting of our analyses. The data (Ni, Co, Si, P, etc.) provided by the EMPA analyses were then compared with metal data (from previous research in the literature) in other type of meteorites such as, ordinary chondrites, enstatite chondrites, iron meteorites, and ureilite metal.

Using these methods we identified 8 metal rich clasts, 2 in DaG 999_r2 and 6 in NWA 10657_003.

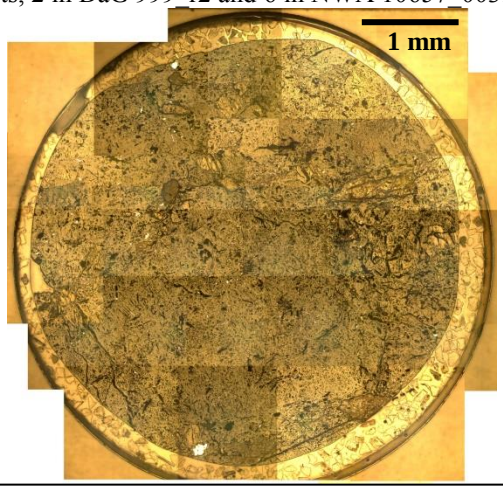

Figure 1. Collage of reflected light images of DaG 999_r2 section. Bright Fe,Ni metal grains in bottom left rim (grain 1) and top left rim (grain 2). Scale is 1 mm.

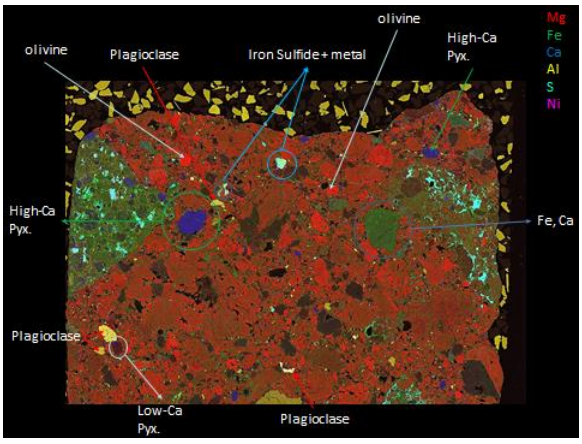

Figure 2. A combined six-element X-ray map of polymict ureilite DaG 999_r2 thin section. Red=Mg, Green=Fe, Blue=Ca, Yellow=Al, Cyan=S, Magenta=Ni. Darker blue is high-Ca pyroxene. Pale yellow is plagioclase. Bright red is olivine. Darker red is low-Ca pyroxene. Combination of cyan, bright green and slight magenta on the rims are iron sulfide and metal.

Results: We describe grain 1 from DaG 999_r2 and grain 5 from NWA 10657_003 in detail. Grain 1 in DaG 999_r2 (Fig. 3a,b) consists of metal (lighter gray) partially surrounded by sulfide (darker gray). Figure 3c shows Ni content along the profile marked in Fig. 3b. Figures 3 d-f show plots of Ni (wt.%) versus Co (wt.%), Si (wt.%) and P (wt.%), respectively for grain 1 compared with metal in various meteorites. These plots help identify the type of grain we have and what meteorite it came from.

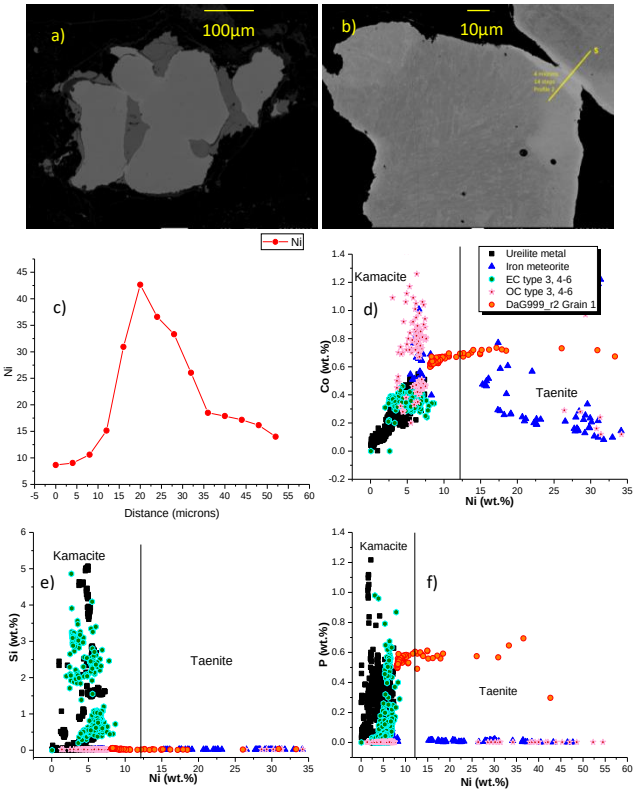

Figure 3. a) BEI of grain 1 in DaG 999_r2; b) BEI showing location of profile 2 (4 µm steps) crossing lighter gray rims (Ni rich); c) Distance(µm) vs. Ni (wt.%) of profile 2 shown in 3b; d) Ni (wt.%) vs. Co (wt.%); e) Ni (wt.%) vs. Si (wt.%); f) Ni (wt.%) vs. P (wt.%). Data for grain 1 shown by the orange circles. Ureilite metal data from [7], iron meteorite data from [8], enstatite chondrite data from [9-11]. Ordinary chondrite data from [12-16].

Grain 1 consists mostly of kamacite, with thin rims trending into the taenite field. The Ni vs. Co, Si plots show that grain 1 compositions overlap those of iron meteorites, ordinary chondrites and enstatite chondrites. However, Ni vs. P shows no overlap with ordinary chondrites.

The internal structure of grain 1 has no widmanstatten structure (an intergrowth of kamacite and taenite characteristic of iron meteorite metal) and is Ni-rich in the rims, Fe-rich in the center and has very low Si values (~0.02 wt.%). The overall assemblage and compositions of grain 1 match best with metal from ordinary chondrite.

Grain 5 in NWA 10657_003 (Fig. 4a,b) consists of metal (lighter gray) surrounded by an assemblage of enstatite grains (dark rounded grains), Cr-rich troilite, and graphite. Figures 4 d-f show plots of Ni (wt.%) versus Co (wt.%), Si (wt.%) and P (wt.%), respectively and compared to the same metals as in grain 1 (Fig. 3).

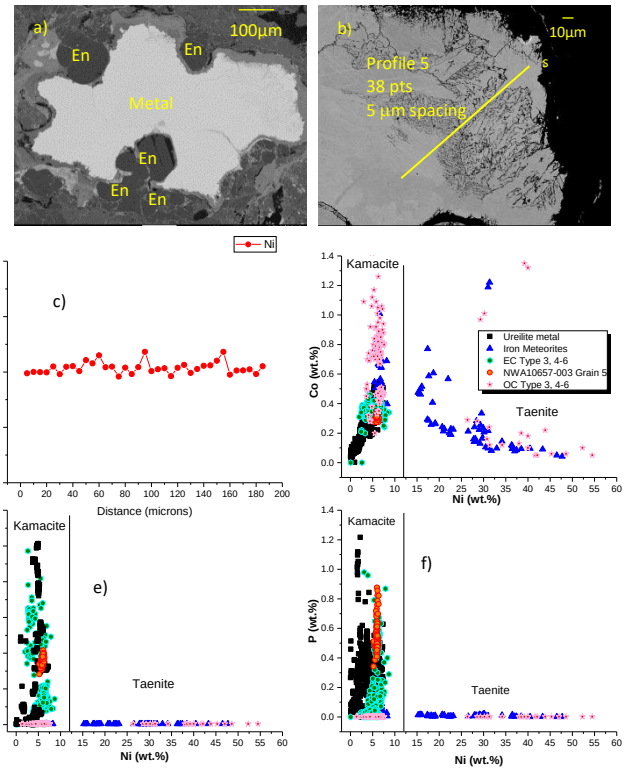

Figure 4. a) BEI of grain 5 in NWA 10657_003; b) BEI showing location of profile 2 (5 µm steps,) crossing across α_2 structure; c) Distance (µm) vs. Ni (wt.%) of profile 2 shown in 4b; d) Ni (wt.%) vs. Co (wt.%); e) Ni (wt.%) vs. Si (wt.%); f) Ni (wt.%) vs. P (wt.%). Data for grain 5 are represented by the orange filled circles. Data for other meteorites from same sources as in figure 3.

Grain 5 consists of kamacite (Fe~91 wt.%, Ni~6 wt.%) with small abundances of Si (~1.9 wt.%). The Ni vs. Co plot shows that grain 5 compostions overlap those of enstatite chondrite, ordinary chondrite, and ureilite metal. The Ni vs. Si, P plots show that grain 5 compositions overlap mainly those of enstatite chondrite metal.

The internal structure of grain 5 shows an intergrowth texture (Fig. 4b). However, compositional profiles show no variation across this structure (Fig. 4c). The structure (Fig. 4b) is an unequilibrated α_2 structure (martensite) that is the result of exceedingly slow

continuous cooling and then nickel-iron is reheated into austenitic region and cooled rapidly [17-19].

Grain 6 in NWA 10657_003 is similar to grain 5 in compositions, as well as associated minerals (enstatite, sulfides including niningerite). The analyses of the metal show kamacite and a small abundance of Si of about 3 wt.%. Both grain 5 and 6 also happen close to each other in the section which may indicate that they both came out of an enstatite chondrite at the time that the impact to the polymict ureilite regolith occurred.

Grain 2 from DaG 999_r2 is also similar to grain 5 from NWA 10657_003 in composition (kamacite with 1.5-2.5 wt.% Si), except that it has an Ni-enriched rim.

Grains 1 and 2 of NWA 10657_003 are similar to grain 1 of DaG 999_r2 in both composition and associated minerals (kamacite partially surrounded by sulfide). Like grain 1 from DaG 999, it has Ni-enriched rims.

Grain 7 is in a large (~8 mm max. dimension) clast of a Rumuruti-type chondrite and grain 8 is in a large (~8 mm max. dimension) clast of an LL chondrite in NWA 10657_003, both previously studied by Goodrich. The data for grain 7 showed Fe (~48 wt.%), Ni (~50 wt.%) metal and Co value of about 1.6 wt.%. Grain 8 had more than one profile analyses in EMPA, it showed sulfide surrounding the metal with low values of Ni (>0.2 wt.%).

Discussion: The abundance of metal grains found in sections DaG 999_r2 and NWA 10657_003 was small. Also, the metal grains we did observe were much smaller than previously described xenoliths in polymict ureilites. None of the Fe,Ni metal grains that we found appeared to be derived from iron meteorites. This result supports the hypothesis that iron meteorite asteroids may not have been present when and where the polymict ureilite regolith formed. These results should be looked as preliminary due to the limited number of sections examined.

The observed grains have properties consistent with derivation mostly from enstatite chondrites and ordinary chondrites. Grain 5 and 6 from NWA 10657_003 and grain 2 from DaG 999_r2 have metal compositions and associated minerals (enstatite, Cr-troilite, graphite, niningerite) very similar to those of metal-sulfide-silicate assemblages in enstatite chondrites [4, 9-11 and 20]. Grain 1 from DaG 999_r2 and grains 1 and 2 from NWA 10657_003 have metal compositions and associated minerals (kamacite partially surrounded by sulfide and Ni-enriched rims) similar to assemblages in ordinary chondrites [12-16]. However, the concentration of Ni decreases from rim to center (Fig. 3c), for grain 1 of DaG 999_r2, instead of increasing as it typically does in an ordinary chondrite [14].

Grains 7 and 8 found in clasts from NWA 10657_003 have properties consistent with metal in their respective chondritic clasts types [12-16 and 21].

Polymict ureilites have diverse foreign clasts with Rumuruti-type chondrites and L/LL chondrites being most abundant [22]. It is notable that half of the metal grains we studied appear to be derived from enstatite chondrites, since previous observations have shown that enstatite chondrite material is rare in typical polymict ureilites [22]. This would suggest that enstatite chondrites could be more common in polymict ureilite regolith, at least from what was observed in this study. Also, from what was previously observed in high abundance in Almahata Sitta [10].

Acknowledgements: I would like to thank Michael Weisberg for the data on enstatite chondrite and Kent Ross for guiding us through the use of the microprobe (EMPA) at JSC. Most of all, I would like to thank Cyrena Goodrich for the opportunity to work on this research project and the financial support from the LPI summer intern program.

References: [**1**] Goodrich, C.A. (1992) *Meteoritics*, 27, 327-352. [**2**] Mittlefehldt D. W., et al. 1998. Reviews in Mineralogy, vol. 36. Mineralogical Society of America. pp. 4-1–4-195. [**3**] Downes H., et al. 2008. *GCA* 72:4825-4844. [**4**] Goodrich C.A., et al. 2015. *Meteoritics* 50, 782-809. [**5**] Cohen B. A., et al. 2004. *GCA* 68:4249-4266. [**6**]Goodrich C. A., et al. 2004. *Chemie der Erde* 64, 283-327. [**7**] Goodrich C. A., et al 2013. *GCA*. 112. 340–373. [**8**]Goldstein J. I., et al. *GCA* 200 (2017) 367-407. [**9**] Michael K. Weisberg, Makoto Kimura. *Chemie der Erde - Geochemistry*, Volume 72, Issue 2, 2012, Pages 101-115. [**10**] Horstmann M., Humayan M., and Bischoff A. 2014. *GCA*, vol. 140. pp. 720-744. [**11**] Brearley A. J. and Jones R. H. 1998. *Planetary materials*. Reviews in Mineralogy, vol. 36. Mineralogical Society of America. pp. 3-1-3-398. [**12**] Rubin A. E. 1990. *GCA* 54:1217–1232. [**13**] Afiattalab F., and Wasson J. T. 1979. *GCA* vol. 44, pp. 431-446. [**14**] Reisener R. J. and Goldstein J. I. 2003. *Meteoritics*, 38, 1679-1696. [**15**] Reed S. J. B. 1964. Nature 204:374–375. [**16**] Zanda B., et al. 1994. Science vol. 265. 1846-9. [**17**] Buchwald V. F. (1975). Online at: http://hdl.handle.net/10524/33767. [**18**] Jones F. W., and Pumphrey W. I.: J. Iron Steel Inst, 163 (1949), 121-131. [**19**]Allen N. P., and Earley C.C. 1950.: J. Iron Steel Inst, 166:281-288. [**20**]Keil, K. (1968). Journal of Geophysical Research Atmospheres. 73. [**21**] Bischoff A., et al. 2011. *Chemie der Erde* 71, 101-133. [**22**] Goodrich et al., 2015. 78th MSM #5018.

LOCATION AND DEGRADATION STATE OF CHAOS ACROSS EUROPA: IS THERE OLD CHAOS?

M. Cruz Quijano[1], J.P. Kay[2], L.M. Prockter[2], [1]AACTyM, Universidad Autonoma del Estado de Hidalgo, Carretera Pachuca Tulancingo Km 4.5, Mineral de la Reforma 42184, Hgo., México, mitzi08uaeh@gmail.com, [2] Lunar and Planetary Institute, 3600 Bay Area Blvd, Houston,Tx 77058.

Introduction: Chaos terrain on Europa has been described as zones where the surface has been disrupted; possibly by diapirism (ascent of warmer material that disrupts the surface). The chaos is characterized by icy blocks within a matrix **[1]** and is described as disrupted plates of icy crust of different sizes, set in a hummocky matrix. One of the most representative chaos examples is Conamara (Fig. 1).

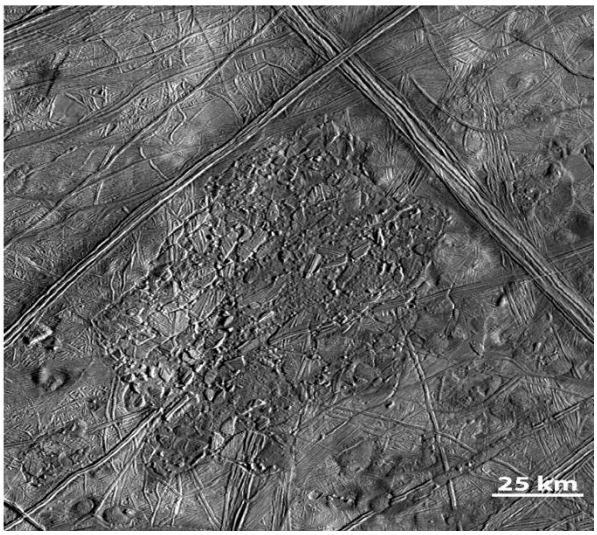

Fig. 1. Conamara chaos shown in and high resolution **[2]**.

It is has been proposed that chaos is the youngest material found on Europa **[1, 3]**. Traditionally, the boundaries (margins) of chaos appear to be inward-facing scarps or embayment by smooth low albedo plains material **[4]**. Chaotic terrain roughly correlates with what was termed mottled terrain in Voyager images **[5]** and two subunits are recognized, platy chaos, in which remnants of the plains units are visible as blocks within the chaos matrix, and knobby chaos, in which remnants of the former plains are not visible **[1]**. Chaotic terrain covers a significant portion of the surface, probably comparable to the fraction of earth's covered by continents **[5]**.

Europa's surface is covered by geologic features that formed in distinct episodes: the oldest observed unit being the ridge plains, which are characterized by bright surfaces overlain by other morphological features; followed by an episode where bands and double ridges have formed, then the formation of chaos terrain and finally another band formation episode **[6]**. Crater statistics suggest that the age of the surface less than 90 million years **[7]**. We use the term "old" if the chaos feature is older than the bands.

The principal objective of this work is to construct a catalog of chaos to quantify and differentiate the presence or absence of old chaos and show those differences in our study area. We compare this work with other authors like **[8, 9]** to identify differences in classification methods and the results about formation of chaos terrain in the stratigraphic column of Europa.

Methods: We use the E11REGMAP01 regional resolution (220 m/pixel) mosaic obtained by the Galileo spacecraft. We use ArcGIS 10.3.1 to digitized the potential chaos features in form of polygons, comparing the characteristics presented below:

Relative albedo (brightness): We use the assumption that features brighten with age [**10]**. We determined three levels of relative albedo characterized by the amount of light reflected by the surface**[10**], as a proxy for age. The highest relative albedo (brightest) corresponds to the oldest surface; intermediate albedo corresponds to intermediate age features, and lowest albedo (darkest) corresponds to young features.

Crosscutting relations (relative ages): Looking at relationships between the chaos and other features (ridges, bands and ridged plains) to assign a relative age, we set up a classification scheme for three different types of crosscutting relationships: the number one correspond to young age, number two for medium age and number three for old features.

Then the albedo and the crosscutting relationships were assessed to determine relative age of chaos. These features were divided into lenticulae (~10 km wide), lobated chaos and domes, microchaos (more than ~20 km wide) and macrochaos (areas with more than ~100 km wide).

Results: We can use relative albedo, possibly texture, and crosscutting relations to infer relative age. Here, we identify 82 chaos features (Table 1). In the case of lenticulae a total of 43 features were found , the lobated material is found in smaller quantity with only 7 mapped which have absorbing albedo (dark) and two similar features showing intermediate albedo, the microchaos was found in a total of 14 features with a variety of albedos, and finally total of 3 macrochaos were found with intermediate/high albedo. We find 8 features could not be easily differentiated, but they presented a predominant albedo of the absorbent (dark), In addition, we find 3 pits with a reflective albedo and 4 domes with a variety of albedos.

Using the methodology described above we determined relative ages and constructed a stratigraphic column (Fig. 4).

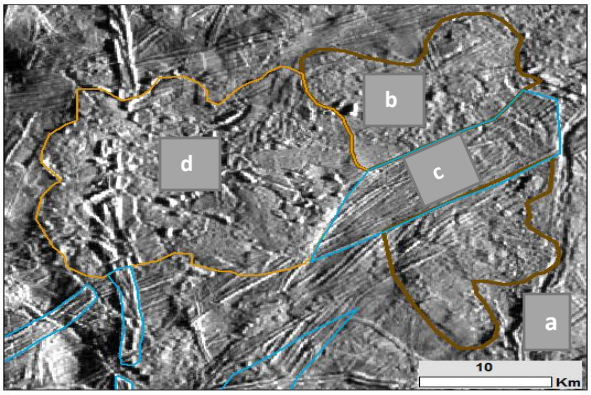

Fig. 2. a) Two chaos features (b and d) has identified by boundary and albedo differences. One band, (c) appears here to b and we can see the ridges plains (a).

Discussion: At the resolutions of the geologic map [**11]** our study area is shown as a single type of chaos (mottled). We found 30 features with high albedo which makes them candidates to be considered as a kind of old chaos. Only 3 microchaos were considered to have old chaos characteristics.

Similarities have been found with the mapping made by **[5]** where the texture was taken into account. We do not use that parameter to determine relative age, because is hard to differentiate the matrix material and the blocks inside the features. The chaos terrain is presented as a unit mapped in blue and subdivided in colors according to the timing of the formation. We find that the chaos in our area (including lenticulae) is presented in three episodes of formation (Fig. 4). Our stratigraphic column begins with ridged plains, then the first episode of bands, followed by the first iteration of chaos. Next we find a second overlapping episode of chaos, followed by further band formation, and finally a third episode of chaos. Ridges are throughout most of the geologic history on Europa crosscutting the preexisting surface, but do not crosscut the most recent episode of chaos. Finally, we note the presence of the impact crater Mannanan.

Future work: We want to expand our work to additional regions to correlate the chaos units found in this work and construct a global map of chaos terrain.

Akwnoldgements: This work has supported by University Space Reseach Asosiation (USRA). Thank you to Universidad Autonoma del Estado de Hidalgo (UAEH) and Instituto Nacional de Estadistica y Geografia.

References: **[1]** Greeley,R. et al. (2000) Geologic mapping of Europa, Journal of Geophysical Research, vol. 105, NO. E9, pages 22,559-22,578.**[2]** Cox, E., et al. (2008) Impact penetration of Europa's ice crust as a mechanism for formation of chaos terrain, Meteoritics & Planetary Science 43,pages 2027-2048. **[3]** Prockter, L.M., et.al (1999) Europa: Stratigraphy and geological history of the anti-Jovian region from Galileo El4 solid-state imaging data, Journal of Geophysical Research, vol. 104, NO. E7, pages 16,531-16,540.**[4]** Collins, G. C., and F. N. Nimmo (2009) Chaotic terrain on Europa, *Europa after Galileo*, pages 259–281, **[5]** Riley,J., et.al. (2000) Distribution of chaotic terrain in Europa, Journal of Geophysical Research, vol. 105, NO. E9, pages 22,599-22,615. **[6]** Figueredo, H. and Greeley, R. (2000) Geological mapping of northern leading hemisphere of Europa from Galileo solid-state image data, Journal of Geophysical Research, vol. 105, NO. E9, pages 22,629-22,646**. [7]** Bierhaus, E., (2009) Europa's Crater Distributions and Surface Ages, EUROPA, pages 161-178. **[8]** Parro, L.M. et al. (2016) Timing of chaotic terrain formation in Argadnel Regio, Europa, implications for the geological history, Planetary and Space Science 130 Elsevier, pages 24-29.**[9]** Leonard et al. (2017) Updating the global geologic map of Europa. Lunar and Planetary Science XLVIII **[10]** Prockter, L.M., et.al (2002) Morphology of Europan bands at high resolution: A mid-ocean ridge-type rift mechanism Journal of Geophysical Research, vol. 107, NO. E5, 5028. **[11]** Doggett, T. et. al., (2009), Geologic Stratigraphy and Evolution of Europa's Surface, EUROPA, pages 137-159.

Table 1. This tables (matrix) shows the amount of features that are classified depending on the relationship between albedo and cross-cutting relations. Example: in the lenticulae table, we have the total of 43 features, there are 6 that meet having reflect albedo and the cross-cutting relationships permit shown that have an old age. One feature in the undefined category was not able to be aged.

Sub unit: Lenticulae		Ages		
Total	43	Old	Medium	Young
16	Reflect	6	1	9
8	Absorb/Reflect	1	6	1
19	Absorb	0	1	18
Sub unit: Lobated		**Ages**		
Total	7	Old	Medium	Young
2	Reflect	1	0	1
2	Absorb/Reflect	0	1	1
3	Absorb	0	0	3
Sub unit: Microchaos		**Ages**		
Total	14	Old	Medium	Young
7	Reflect	3	1	3
1	Absorb/Reflect	0	1	0
6	Absorb	1	2	3
Sub unit: Macrochaos		**Ages**		
Total	3	Old	Medium	Young
0	Reflect	0	0	0
2	Absorb/Reflect	0	2	0
1	Absorb	0	0	1
Sub unit: Undefinied		**Ages**		
Total	8	Old	Medium	Young
0	Reflect	0	0	0
1	Absorb/Reflect	0	1	0
7	Absorb	1	1	4

Sub unit: Pits		Ages		
Total	3	Old	Medium	Young
3	Reflect	0	0	3
0	Absorb/Reflect	0	0	0
0	Absorb	0	0	0

Sub unit: Domes		Ages		
Total	4	Old	Medium	Young
2	Reflect	1 ?	0	1
1	Absorb/Reflect	0	1	0
1	Absorb	0	0	1

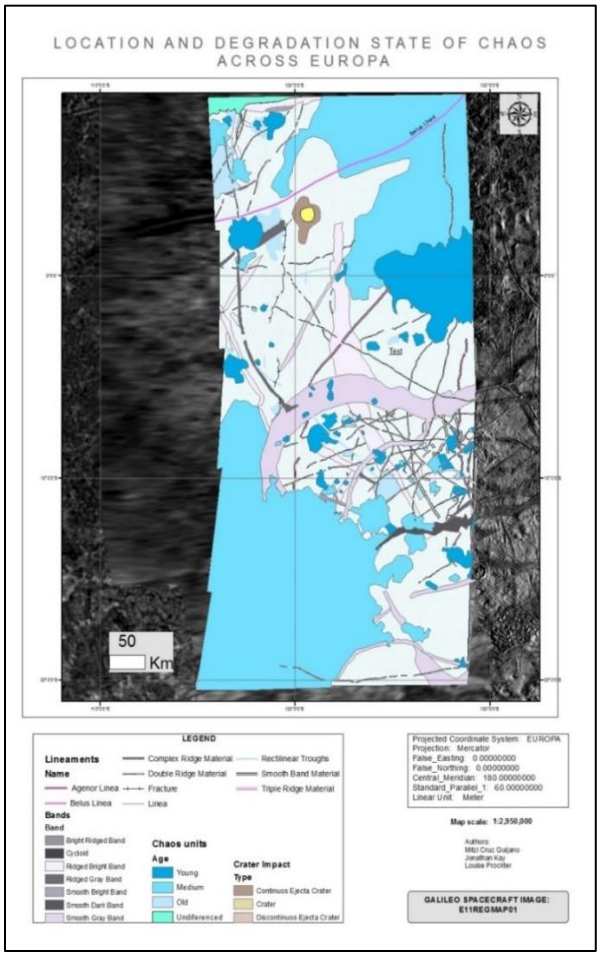

Fig. 3. Map of E11REGMAP: Shows the location of chaos features, location classified by ages.

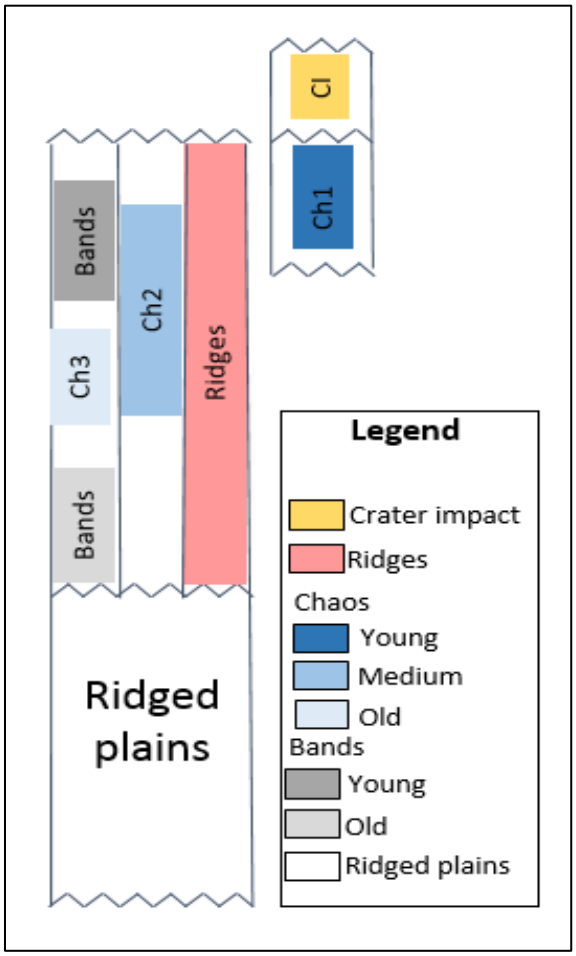

Fig. 4. Stratigraphic column constructed with the results of the chaos units, showing 3 episodes of chaos formation.

ACIDIC DISSOLUTION OF PHOSPHATE-RICH AND PHOSPHATE-POOR BASALTS: IMPLICATIONS FOR THE STIMSON SANDSTONE UNIT, GALE CRATER Nathan K. Hadland[1], Valerie Tu[2], Elizabeth Rampe[3]
[1]Department of Physics and Space Sciences, Florida Institute of Technology (nhadland2016@my.fit.edu), [2]Jacobs, NASA Johnson Space Center, [3]Astromaterials Research and Exploration Science, NASA Johnson Space Center

Introduction: The Stimson Formation is composed of fractured sandstone that unconformably overlies the Murray Formation in Gale Crater (Fig. 1)[1, 2]. The Mars Science Laboratory (MSL) rover, Curiosity, investigated Stimson at the Okoruso and Big Sky drill sites in 2015-2016. Samples of unaltered (parent) and altered rock within and around alteration halos at these sites were analyzed by the Chemistry and Mineralogy (CheMin) X-Ray diffractometer instrument. Bulk geochemical data from the Alpha Particle X-ray Spectrometer (APXS) demonstrate the presence of phosphate, and CheMin results suggest it may be present as fluorapatite [1]. However, it is uncertain whether fluorapatite is responsible due to the limited angular resolution of CheMin. Additionally, hydrothermalism has been reported to have occurred in Gale Crater, so the relatively young alteration halos in the Stimson Formation suggest acidic hydrothermal alteration of parent minerals [3]. Phosphate, a known mobile element, persists in acidic environments at comparable ratios to Ti, a non-mobile element, and the formation of Fe-phosphates may explain the unusual phosphate behavior in alteration halos [4].

Previous acidic alteration experiments of phosphate-rich basalts have subjected the material to various fluid:rock ratios to constrain the amount of water necessary for secondary product formation using synthetic materials [4, 5]. This study will impose additional environmental constraints using natural samples and will extensively characterize the phases of the resultant secondary minerals as well as subject the products to cryogenic and dry conditions, similar to the current Martian environment. Analysis of the resultant secondary phosphate-bearing phases from these experiments and their formation pathways aims to further constrain the hydrothermal fluid:rock interactions in the Stimson Formation.

Methods: Single-step, acidic batch dissolution experiments were performed based on the methods of Golden et. al 2005, Hausrath et. al 2013, and Marcucci and Hynek 2014, mimicking a closed hydrothermal system, such as the closed system seen in the Burns formation at Merdiani Planum [3]. HWPC100 (Puna Coast) basalt samples were used as the starting material with a composition of glass>olivine>plagioclase [6]. Using a Panalytical X'Pert Pro MPD, X-Ray Diffraction (XRD) patterns of HWPC100 powder mounts were measured over a range of $2-80^o 2\theta$ and were analyzed using the ICDD database in HighScore. HWPC100 basalt and fluroapatite samples were pulverized to <150 μm. Particle size analysis was performed and confirmed a size fraction of

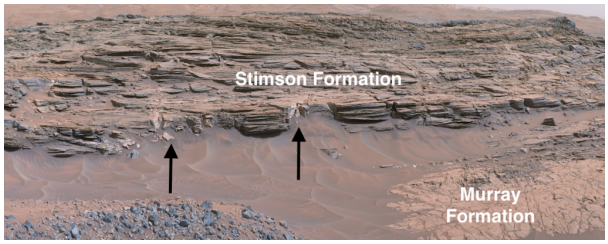

Figure 1: This image was acquired from Mastcam-100 on Sol 993. The arrows show fracture-associated alteration halos.

141 μm. 10 wt% Durango fluorapatite was added to half of the HWPC100 basalt samples based on the highest P_2O_5 findings from APXS on Curiosity in Gale Crater [1]. 1 M H_2SO_4 was titrated with NaOH to achieve a pH of 3 based on the reported jarosite pH range of 2-4[8]. The acid was added to 100 mg of sample to achieve the fluid:rock ratios of 4:1 and 10:1 [4, 7] at sufficient quantities for a complete reaction according to the equation[4]:

$$Ca_5(PO_4)_3F + 10H^+ \longrightarrow 5Ca^{2+} + HF + 3H_3PO_4 \quad (1)$$

Stainless steel Parr hydrothermal reaction vessels lined with Teflon were loaded with the samples and placed in an oven without shaking at 50^{o}C and 150^{o}C and durations of 24 hours, 72 hours, and 1 week. Solutions were removed, cooled to room temperature and effluent liquid was decanted off. The liquid was filtered with a 5 μm filter, acidified with HCl to a pH of 2 to retain dissolved species, and refrigerated at -20^{o}C for analysis of dissolved species at a later date. For the solid secondary products, half was flash frozen with liquid N_2 and the other half was subjected to dessication via rinse filtration with ethanol and air drying with cover for up to 5 days [7]. Powder XRD was used to identify secondary products. In addition, Scanning Electron Microscopy (SEM) using a JEOL 7600F and a JEOL 5910LV equipped with Energy Dispersive Spectroscopy (EDS) was used for surface topographic analysis using Backscatter Electron Imagery (BEI). XRD of select samples on the laboratory version of CheMin (CheMinIV) was also used.

Results: Characterization of the original basaltic material, HWPC100, through XRD indicates the presence of Mg-rich olivine (forsterite), pyroxene, and plagioclase feldspars (Fig 3). The alteration products of the acidic hydrothermal dissolution experiments via fluid:rock interactions are summarized in Table 1. In general, free sodium ions from the powdered natural basalt samples and NaOH in the liquid, reacted with sulfuric acid to form the secondary product of thenardite (Na_2SO_4). Additionally, unidentified amorphous material was formed (Fig 4). Thenardite consistently covered

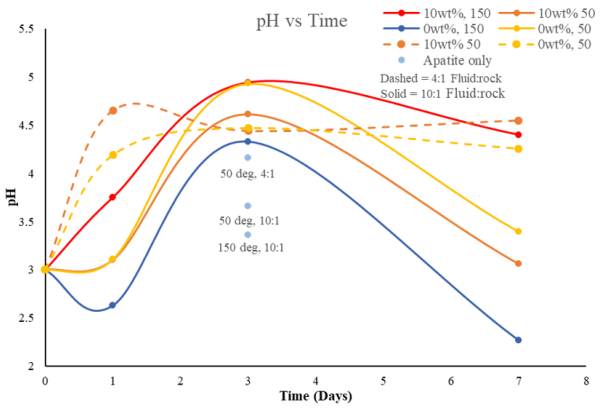

Figure 2: pH of decanted liquid samples over time.

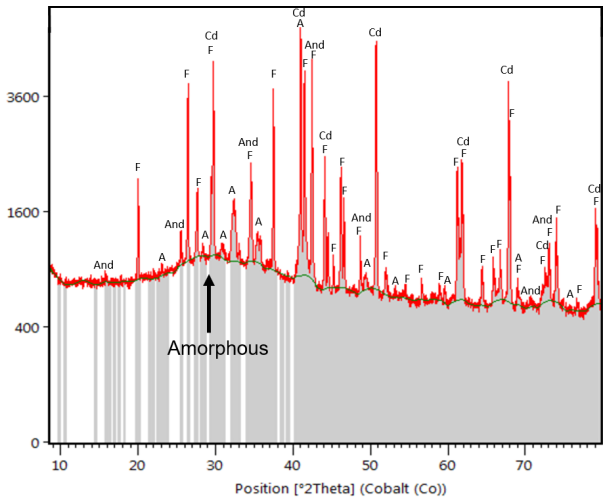

Figure 3: An XRD diffractogram of spiked unaltered HWPC100 basaltic material where F = Forsterite, Cd = Corundum, A = Augite, And = Andesine

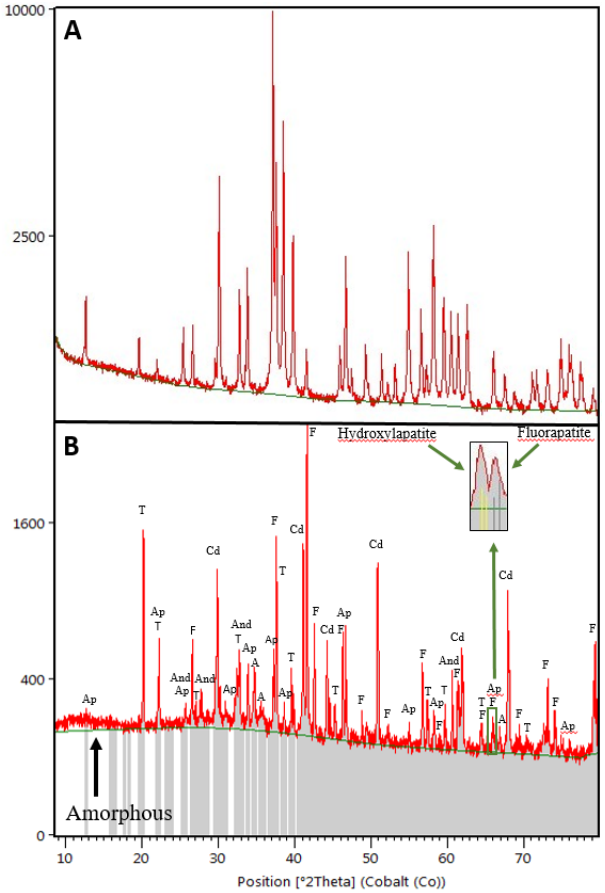

Figure 4: **A** depicts a XRD diffractogram of unaltered Durango fluorapatite and **B** is a spiked, altered basalt reacted at 150^{o}C with a 4:1 fluid:rock ratio and 10 wt% fluorapatite for 1 week where F = Forsterite, And= Andesine, Cd = corundum, Ap= Fluorapatite, T = Thenardite, and A= Augite

the surfaces of the basaltic material after the reactions. However, there were variances in morphology likely as a function of formation conditions (i.e. temperature and duration). Other significant phases detected by XRD include forsterite, augite, pigeonite, anorthite, andesine, and enstatite. There are indications of trace phosphate phases such as hydroxylapatite and chloroapatite arising from the phosphate rich experiments (Fig 4). Other possible trace phases include quartz, cristobalite, and ilmenite. The mean size fraction of the unaltered Durango fluorapatite was approximately 141 μm measured by the particle size analysis instrument, but after hydrothermal dissolution, the average grain size was approximately 5 μm. In general, experiments that reacted at low temperatures (50^{o}C), low fluid:rock ratio (4:1), and were flash frozen had a larger average grain size of residual phosphate minerals, and grain size decreased with increasing experiment duration. The secondary phosphate minerals largely persisted on the surface of the basalt grains in the presence of thenardite (Fig 5). In addition, there was little visual difference between flash frozen and rinse filtered samples, with a similar amount of residual salts.

For the 10:1 fluid:rock cases, the pH of the liquid after the reactions increased after 24 hours and then decreased after 72 hours (Fig 2). However, for the 4:1 fluid:rock experiments, the pH increased after 24 hours and stayed approximately the same for 1 week.

Discussion: The primary objective of this work was to identify secondary phases resulting from hydrothermal acidic dissolution of natural basalts spiked with fluorapatite to determine the characteristic mineralogy linked to fluid:rock interactions and other alteration conditions. Ultimately, the resultant secondary phases can help further constrain the formation pathways of minerals in Gale Crater during the last moments of liquid water on Mars as well as gain insight into phosphate availability for potential biological uptake. Specifically, we investigate the mineralogical impact of varying temperature, duration, fluid:rock ratio, and phosphate content. Despite the acidic dissolution conditions that phosphate rich basalts were subjected to, fluorapatite appears to persist in the acidic environment, with undissolved phosphate

	XRD	SEM/EDS
Unaltered Basalt (HWPC100)	Olivine*, Enstatite*, Andesine*, Pigeonite*, Augite*, Basaltic Glass*, Fluorapatite**	Ca-, Mg-, Si, Fe-, Ti-, Al- Cr-rich surfaces, Ca-phosphate**
4:1 Fluid:Rock Experiments		
P-rich (10wt%), 150^{o}C, 1 week	Fluorapatite, Anorthite, Thenardite, Hydroxyapatite**	Na, Ca-Phosphate, Sulfate
P-poor, 150^{o}C, 1 week	Thenardite	Na, Ca-sulfate
10:1 Fluid:Rock Experiments		
P-rich (10wt%), 150^{o}C, 1 week	Fluorapatite, Anorthite, Thenardite	Na, Ca-Sulfate, Ca-Phosphate
P-poor, 150^{o}C, 1 week	Thenardite	Na, Ca-Sulfate, Ca-phosphate

Table 1: Summary of select acidic dissolution experiments and resultant phases. A * denotes a phase detected in the original basaltic material that is detected throughout the experiments and ** denotes a possible trace phase.

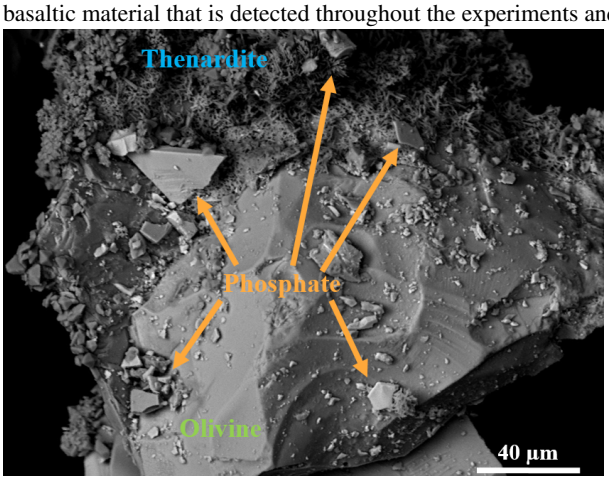

Figure 5: BEI image of a altered 10 wt% basalt ambient to 150^{o}C at 4:1 fluid:rock ratio for 1 week.

grains persisting, even after 1 week at 150^{o}C. However, the average size of the phosphate mineral grains was significantly reduced throughout the experiments, and a large amount of the material was washed out during the filtration step, which was expected due to the known mobility of fluorapatite. Additionally, we mimic a closed system which may affect the formation of surface salts. The Murray Formation has been suggested to model an open system. Therefore, flow through dissolution experiments are necessary subsequent studies [9]. Complex weathering reactions caused changes in pH and for both fluid:rock ratios, adsorption of phosphate and sulfate ions to a protonated basalt surface caused an increase in pH. However, potential desorption of sulfate ions back into solution caused a decrease in pH (Fig 2)[10]. The lack of significant variation of pH in 4:1 experiments after 24 hours, as well as the larger average phosphate grain size implies limitation of dissolution due to a low fluid:rock ratio (Eqn 1). Unlike the findings of Hausrath et. al 2013 in their acid-vapor experiments using synthetic samples (versus the liquid:rock experiments using natural samples discussed here), Fe-phosphates were not detected and fluorapatite still persisted which implies another mechanism, such as the formation of sulfate minerals or lower fluid:rock ratios, for the persistence of phosphates [4]. Indeed, much of the apatite grains were caught on the surface of the hydrothermally altered basalt grains with the significant quantities of thenardite, which suggests compatible surface charges to capture the phosphate minerals (Fig 5). In follow up experiments, rinsing with water in place of ethanol will dissolve the salts to allow SEM imaging of underlying features. The identification of secondary minerals, investigation of pH variation, effluent liquid concentration studies, and imaging topographical features through additional analysis will help reveal the fluid:rock chemical history of Gale Crater.

Conclusion: In a closed hydrothermal system, fluorapatite appears to persist in an acidic environment for one week. If fluorapatite explains the presence of phosphate in the Stimson Formation, sulfate minerals interacting with apatite at low fluid:rock ratios may allow phosphates to persist in an acidic environment for periods up to, and perhaps exceeding 1 week. The presence of phosphate in an accessible form has implications for Mars' past habitability due to its importance in biology. Continuing characterization of the mineralogy from dissolution experiments will reveal past Martian environmental parameters through the hydrothermal alteration conditions.

Acknowledgments: Thank you to Doug Ming, Dick Morris, Joanna Hogancamp, Amanda Ostwald, and Tanya Peretyazhko for their contributions to this project.

References

[1] Yen A. S. et. al. *Earth and Planetary Science Letters*, 471:186–198, 2017. [2] Blake D. F. et. al. *Space Science Review*, 2012. [3] Hausrath E. M. et. al. *Earth and Planetary Science Letters*, 491:1–10, 2018. [4] Hausrath E. M. et. al. *Journal of Geophysical Research (Planets)*, 118:1–13, 2013. [5] McCollom T.M et. al. *Journal of Geophysical Research (Planets)*, 123(5):1230–1254. [6] Golden D. C. et. al. *Journal of Geophysical Research (Planets)*, 110:E12S07, 2005. [7] Marcucci E. C. and Hynek B. M. *Journal of Geophysical Research (Planets)*, 119:679–703, 2014. [8] Elwood Madden M. E. et. al. *Nature*, 431:821, 2004. [9] Rampe E. B. et. al. *Earth and Planetary Science Letters*, 471:172–185, 2017. [10] D. Peak. *Journal of Colloid and Interface Science*, 218:289–299, 1999.

MINERALOGY AND PETROLOGY OF DARK CLASTS IN POLYMICT EUCRITES.

Alexander P. Holmwood[1] and Kevin Righter[2], [1]Department of Geosciences, Hamilton College, Clinton, NY 13323, aholmwoo@hamilton.edu, [2]NASA Johnson Space Center, 2101 NASA Parkway, Houston, TX 77058, kevin.righter-1@nasa.gov.

Introduction: NASA's Dawn mission obtained regolith spectral data from the asteroids 4 Vesta and 1 Ceres in order to investigate formation and differentiation processes on early solar system bodies. Laboratory analyses of meteorites from the howardite-eucrite-diogenite suite (HED) of achondrites, in conjunction with Dawn's spectral data, indicate a strong correlation between HEDs and Vesta. Evidence for this correlation includes, but is not limited to, compositional variability in HEDs and Vesta's surface mineralogy, similar pyroxene chemistry in HEDs and Vestan regolith, and the presence of carbonaceous chondrite material in Vesta's regolith and in howardites [1, 2]. Vesta has long been considered the HED parent body [1], and Dawn's data strengthened that connection. In addition, Dawn identified dark material, light material, and orange material on Vesta through its Framing Camera (FC), visible and infrared spectrometer (VIR), and Gamma Ray and Neutron Detector (GRaND) [1, 2, 3, 4]. Lithological identification by the Dawn mission has included both carbonaceous chondrite and impact melt lithologies.

Polymict eucrites of the Allan Hills (ALH) 76005 pairing group contain fine-grained dark clasts with various textures, mineral assemblages, and chemistries [5]. Analyzing the petrology of such dark clasts can reveal new information regarding eucrite source material, Vesta's crustal composition, or the composition of an impactor. The mineralogy and petrology of dark clasts in the ALH 76005 pairing group is not well known, yet may be related to the dark or orange material observed by Dawn. Detailed study of these clasts may thus bolster our understanding of the geology of Vesta.

This project aims to characterize representative textures, mineralogies, and chemistries of dark clasts in fifteen thin sections from the ALH 76005 polymict eucrites pairing group. Data acquired will help address questions regarding the dark clasts' properties and whether they describe a distinct Vestan lithology or the lithology of an exogenous impactor. In addition, data acquired will be used to hypothesize the dark clasts' mechanism of formation and relate this mechanism to hypotheses regarding the presence of dark material and orange material on Vesta's surface.

Methods: Preliminary observations of the dark clasts' texture and mineralogy were performed with a Nikon optical microscope equipped with a digital camera using plane- and cross-polarized light. Photographic mosaics were created for all thin sections and used for reference during SEM chemical mapping, electron microprobe analyses, and modal analyses.

The JEOL 5910LV conventional SEM was used for making preliminary qualitative chemical observations of representative dark clasts before observing them under the JEOL 7600F field emission SEM. In addition to these qualitative chemical analyses, representative dark clasts were analyzed using a CAMECA SX-100 electron microprobe in order to obtain quantitative bulk chemistry and mineral chemistry data. Microprobe point, line, and areal analyses were performed at an accelerating voltage of 15 kV, a sample current of 20 nA, and with a 30 μm beam diameter.

Results:

Textural variety: Backscattered electron images showed that eucritic clasts exhibit ranges of textures. The polymict eucrites are fragmental breccias and thus feature mostly subhedral to anhedral pyroxene and plagioclase embedded in a very fine, aphyric matrix. Ophitic and subophitic clasts are common in addition to singular pyroxene and plagioclase and can be quite large. ALHA81006,33 features a single ~3500 μm, subrounded and subophitic clast with cumulate plagioclase, for example.

Individual dark clasts featured several different textures. Eight textural groupings appeared upon observing representative dark clasts from each thin section:

1. Elongate, euhedral, randomly-oriented skeletal clinopyroxene phenocrysts embedded in a fine clinopyroxene and plagioclase matrix (Fig. 1).
2. Fine-grained, interlocking, blocky, and subhedral clinopyroxene and plagioclase.
3. Brecciated dark clasts with mineral fragments incorporated a fine pyroxene and plagioclase matrix.
4. Aphyric, quenched matrix of clinopyroxene and plagioclase with 200 μm-scale silica-plagioclase-troilite inclusions (Fig. 2).
5. Mostly aphyric matrix of subhedral-anhedral, elongate, and quenched pyroxene and plagioclase.
6. Euhedral clinopyroxene crystals within a trachytic matrix of fine-grained pyroxene and plagioclase.
7. Pilotaxitic clinopyroxene and plagioclase matrix.
8. Fan-spherulitic plagioclase and clinopyroxene with minor troilite and ilmenite clusters.
9. Matrix of blob-shaped anhedral clinopyroxene, silica, and ilmenite.

Textures 1 to 6 are the most common, whereas textures 7, 8, and 9 only appear in one dark clast each.

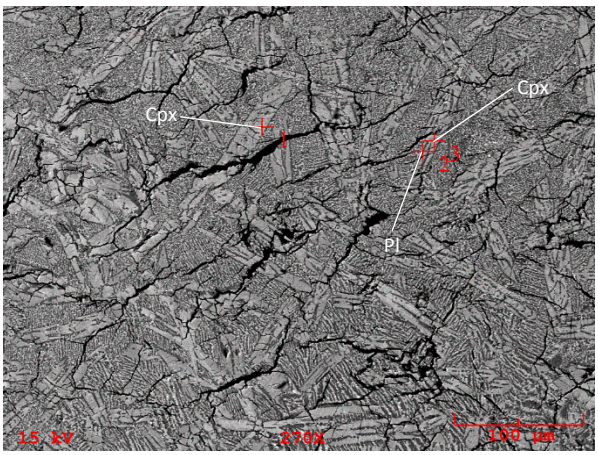

Figure 1: Backscattered electron image of dark clast ALHA76005,9-D01. Elongate, anhedral plagioclase and pyroxene matrix envelope skeletal clinopyroxene crystals. Numbers indicate locations of conventional SEM spectral analyses.

Mineralogical characteristics: The ALH 76005 polymict eucrites exhibit similar mineral phase assemblages. Major phases include plagioclase, clinopyroxene, and orthopyroxene, while minor phases include ilmenite, chromite, troilite, and rare Fe-Ni metal. Amorphous silica, while not a major eucritic phase, is also quite abundant and often occurs with troilite. Dark clast modal percentages from all fifteen thin sections range from approximately 2.9-38%, with an average of 10.7% and a median of 5.5%. Twelve thin sections have 3-10% dark clasts, while three have above 20%, showing the tendency toward having fewer dark clasts.

Qualitative chemical analyses: Spectral data revealed clinopyroxene, plagioclase, orthopyroxene, and silica as the major mineral phases in dark clasts, and it revealed some dark clasts to be oxide mineral phases (e.g. ilmenite and chromite). Color-coded x-ray mapping of texturally and mineralogically representative dark clasts also aided differentiation among phases and illustrated relative abundances of major phases (Fig. 2).

Compositional trends: Electron microprobe analyses permitted chemical comparisons among polymict eucrite dark clasts and other meteorite groups. Average MgO values for dark clasts are low, ranging from approximately 4.2% to 6.9%. The amount of FeO increases with rising MgO content. Average FeO for dark clasts ranges from 12.2% to 19.9 %, while average TiO_2 for dark clasts ranges from 0.51% to 1.17%. The range of Al_2O_3 values is relatively high at 12.0% to 16.6%, and CaO is also quite high with values between 9.1% and 12.2%. Percentages for other minor oxide phases, in contrast, are minimal. Despite the abundance of chromite in the thin sections, values for Cr_2O_3 in dark clasts, for example, lie between 0.02% and 0.38%. All oxide values fit within a specific chemical region relative to other meteorites that will be discussed further [6, 7].

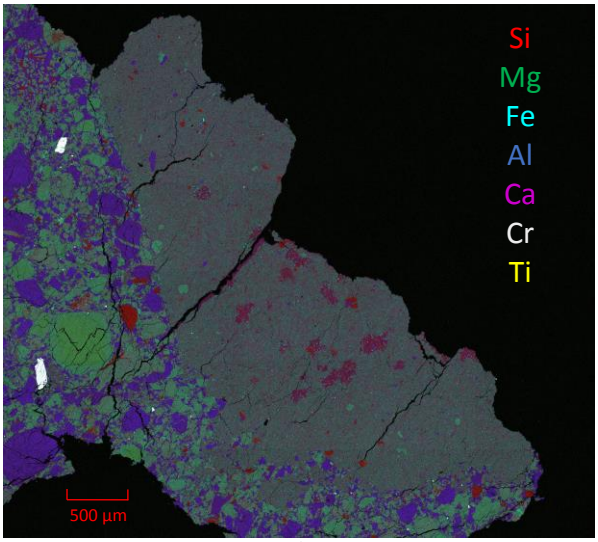

Figure 2: Chemical x-ray map of dark clast ALHA79017,46-D01. The clast composes the right-hand side of the thin section and features 150-200 µm silica-plagioclase-troilite (red- and magenta-colored) inclusions in a fine matrix.

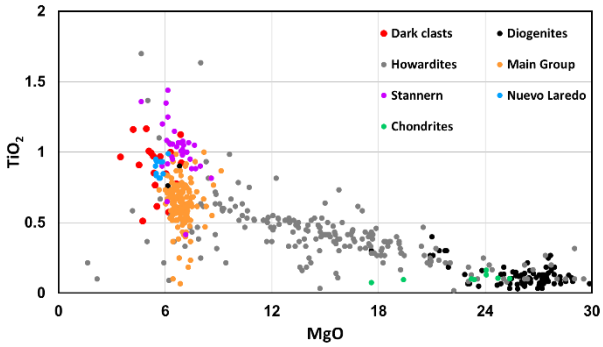

Figure 3: Scatter plot of TiO_2 versus MgO for ALH 76005 dark clasts, other HED samples, and chondrites from [6] Mittlefehldt (2015) and [7] Newsom (1995).

Discussion: Why are dark clasts dark?

Shock-darkening: Mobilization of certain phases in a meteorite via impact shock can cause darkening. Sulfide and metal mobilization through shock veins or as droplets in veins and glasses particularly contribute to shock darkening, as seen in the Chelyabinsk chondrite [8]. Troilite and ilmenite have been observed with amorphous silica-plagioclase inclusions in select dark clasts from thin sections ALHA76005,39, ALHA78040,94 ALHA78132,50, ALHA79017,46, ALHA81006,33 (Fig. 4), and ALHA81008,6, and independent of dark clasts in ALHA78040,19 and ALHA81009,4. Zhang et al. (2013) suggested impact-mobilized S-rich vapor as responsible for sulfurization of pyroxene and plagioclase in the NWA 2339 eucrite [9]. This process is a possible formation mechanism for silica-plagioclase inclusions in dark clasts and in matrix material, and it also provides enough troilite to cause darkening throughout the clast.

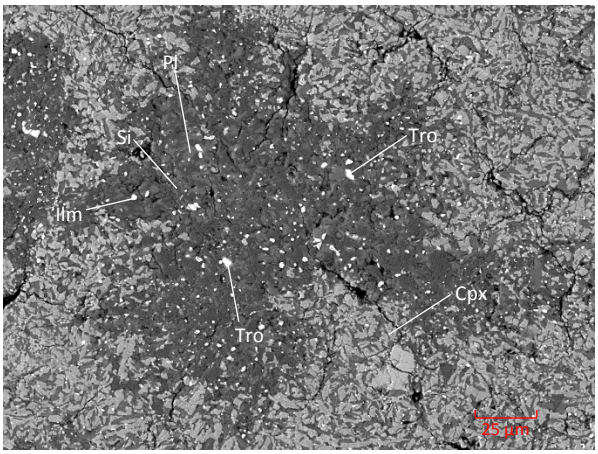

Figure 4: Amorphous silica-plagioclase inclusion with troilite and ilmenite in ALHA81006,33-D01.

Discussion: How did the dark clasts form?

We will now consider x-ray chemical data and bulk compositional data to evaluate the origin of the dark clasts. Plots of average TiO_2 versus MgO and average FeO versus MgO display compositional variability in eighteen representative dark clasts and show a distinct chemical trend relative to howardites, diogenites, Main Group eucrites, Stannern trend eucrites, Nuevo Laredo trend eucrites, and chondrites (Fig. 3) [6, 7].

Chondritic impactor hypothesis: Albedo and band depth values for dark material on Vesta's surface suggest a history of carbonaceous chondrite impacts, with HED breccias as good possible sources for carbonaceous chondrite fragments [2, 3]. However, chemical x-ray maps of representative dark clasts illustrate a lack of major or minor elemental C. Percentages of MgO and TiO_2 are too low and too high, respectively, to reflect chondritic compositions as well, and thus it is unlikely for the dark clasts to be sourced from these regions.

Eucritic compositions of dark clasts: Oxide plots suggest a eucritic origin for the dark clasts, as both TiO_2 versus MgO and FeO versus MgO plot with Main Group, Stannern, and Nuevo Laredo trend eucrites, while howardites, diogenites, and chondrites are separated by high MgO values [6, 7]. The dark clasts' eucritic nature suggests they are endogenous to Vesta or Vestoids and have been incorporated into eucritic breccias by impacts. The unique chemical signature of eucrites and HED meteorites in general makes these dark clasts being exogenous impactors unlikely.

Eucritic impact melt hypothesis: Many dark clasts contain a fine-grained, quenched matrix of plagioclase and clinopyroxene. For comparison, the HED meteorite NWA 1240 is an impact melt with skeletal low-Ca pyroxene crystals in a plagioclase and pyroxene matrix, and it is texturally similar to dark clasts with skeletal clinopyroxene crystals embedded in quenched pyroxene and plagioclase [10]. The combination of quenched textures in the dark clasts, the brecciated nature of the polymict eucrite thin sections, and the angular shapes of the dark clasts make impact melting and subsequent brecciation a possible candidate for dark clast formation.

Spectral properties of Fe in orange material around Vesta's Octavia and Oppia craters point to a basaltic eucrite to howardite composition [4]. In addition, eucrite-diogenite ratios from FC color data indicate that ejecta from the Octavia and Oppia craters are in eucrite-rich regions [4, 11, 12]. Le Corre et al. (2013) hypothesized that, based on chemical and spectral properties of orange material, that impact melting is a suitable candidate for formation of orange material [4]. The Oppia and Octavia crater ejecta are thus potential source regions for the ALH 76005 dark clasts.

Conclusions and future studies: Dark clasts of the ALH 76005 polymict eucrite pairing group contextualize impact processes on Vesta through their textures, mineralogies, and chemistries. Eucritic compositions of dark clasts and chemical x-ray maps suggest the dark clasts are endogenous to Vesta's regolith as opposed to from exogenous impactors. Textural similarities between the NWA 1240 impact melt and dark clasts point toward impact melting processes as generating the dark clasts, and the locations of Vestan orange material within eucrite-rich regions support this hypothesis.

The dark clasts occur in fragmental eucritic breccias, but whether they occur in regolith breccias or impact melt breccias has yet to be investigated and can help evaluate the impact melt hypothesis. Obtaining detailed elemental data for skeletal clinopyroxene, quenched pyroxene, and quenched plagioclase will complement bulk chemical data and may reveal a more distinct chemical TiO_2 versus MgO trend relative to other eucrite trends. Studying the effects of impact melting on dark clast chemistry can also supplement these chemical analyses.

References: [1] McSween et al. (2013) *Meteoritics and Planet. Sci., 48*, 2090–2104. [2] Reddy et al. (2012) *Icarus*, 221, 544–559. [3] McCord et al. (2012) *Nature*, 491, 83–86. [4] Le Corre et al. (2013) *Icarus*, 226, 1568–1594. [5] Righter (2011) 34th Symposium on Antarctic Meteorites, #20110023038. [6] Mittlefehldt (2015) *Chemie der Erde*, 75, 155–183. [7] Newsom (1995) *Global Earth Physics: A Handbook of Physical Constants*, 1, 159–189. [8] Righter (2015) *Meteoritics and Planet. Sci.*, 50, 1790–1819. [9] Zhang et al. (2013) *Geochimica et Cosmochimica Acta*, 109, 1–13. [10] Barrat et al. (2003) *Geochimica et Cosmochimica Acta*, 67, 3959–3970. [11] Peplowski et al. (2013) *Meteoritics and Planet. Sci.*, 48, 2252–2270. [12] Prettyman et al. (2013) *Meteoritics and Planet. Sci.* (2013), 48, 2211–2236.

LRO LAMP Far Ultraviolet Investigation of Cold Spots and a New Impact Crater on the Moon. E. L. Jhoti[1] and Y. Liu[2], [1]School of Physics & Astronomy, The University of Edinburgh, Edinburgh, UK, [2]Lunar and Planetary Institute, Houston, TX, USA, elisha.jhoti@gmail.com.

Introduction: The Moon is a prominent location for studying the crater formation processes and regolith modification post impact. Extensive modification has been observed around some fresh craters and newly formed craters, extending to tens of crater radii or more [1, 2]. For example, DIVINER, an instrument on-board the Lunar Reconnaissance Orbiter (LRO), has discovered thermal anomalies observed in rayed profiles around fresh craters, known as cold spots. These were defined by Bandfield et al., 2014 to be at least 2K lower than the global average nighttime regolith temperature [1]. They extend to ~20-101 crater radii outwards around the craters, with a profile similar to proximal ejecta deposits (Figure 1). All cold spots are associated with young impact craters but not all more mature impact craters have cold spots. Their formation mechanism is elusive. They cannot be explained by the displacement of ejecta alone and there is no topographic evidence for their presence. Interestingly, there is no spectral or albedo evidence of their formation in the visible or infrared [1].

Formation mechanisms proposed in past literature included granular flow of solid materials, due to cascading secondary impacts. However, this would require minimal deposition and excavation of the material. Another mechanism proposed was gas flow across the surface derived from either the impactor or target [1], and localized churning due to jetted vapour [2].

Cold spots have been observed to fade over time on a scale of hundreds of thousands of years, possibly due to space weathering [3]. Once the cold spot has faded to a certain extent, they can no longer be observed in temperature maps, and can only be seen by their differing H parameter values. H parameter is a measure of the rate of regolith density increase with depth. The churning up of the upper layers of the regolith during impact leads to a surface layer of lower thermal inertia, with a corresponding higher H parameter value [4].

Numerous new impact events have been found by the Lunar Reconnaissance Orbiter Camera (LROC) team using Narrow Angle Camera (NAC) paired observations [2]. Speyerer et al. [2] found that the cratering rate is higher than predicted by the Neukum production function, which implies that the regolith is being stirred up on a much shorter timescale than previously thought, it is believed that all new impact craters might have cold spot features initially [1]. Indeed the analysis of a 70m new impact crater formed in 2012 by the DIVINER team shows cold spot features around it (personal communication). The study of these new impact craters is key to understand the formation mechanism of cold spots as well as impact processes.

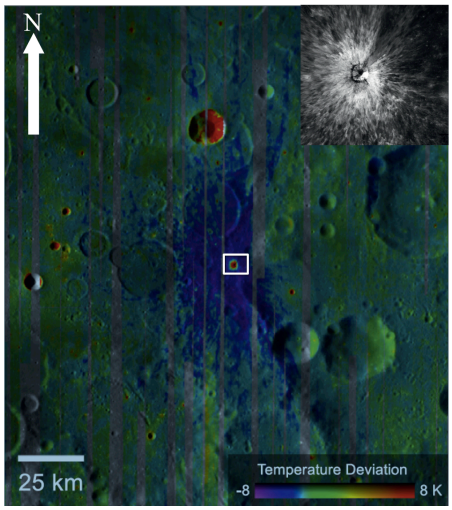

Figure 1: DIVINER nighttime regolith temperature map of a cold spot near 90.8°E, 5.4°S around a fresh crater, adapted from Figure 4 of Bandfield et al 2014 [1]. The cold spot regions are seen in blue. The white square indicates the region shown in the top right LROC image.

In this study, cold spots and new impact craters were investigated using observations from the far ultraviolet (FUV) spectrograph on-board LRO known as the Lyman Alpha Mapping Project (LAMP). For cold spots, the objective is to explore their possible formation mechanisms and their degradation due to space weathering. For the new crater, the objective is to investigate spectral properties of the regolith before and after impact and implications for impact processes.

Methodology: The primary dataset used in this study is the FUV data from the LRO LAMP instrument. LAMP is nadir pointing and provides global coverage of both nightside and dayside of the Moon in the wavelength range 57-196 nm, with a spatial resolution of ~250m/pixel. It has two observation modes: lunar nightside, when the aperture door is open and faint Lyman alpha sky glow and UV bright stars are used for illumination; and lunar dayside, when the aperture door is closed and sunlight illuminates through a pinhole [5].

Only dayside LAMP data were analyzed so far in this study, and analysis of nightside data will be included in the future. The dayside observations measure bidirectional reflectance, which depends on the incident, emission and phase angles, as well as soil properties. This results in data with different viewing geometries, therefore to compare the data over the same area, photometric corrections are required to normalize the reflectance. The data used in this work are all photometrically corrected using the method of Liu et al., 2018 [6]. To improve the signal-to-noise ratio, data between the beginning of the mission (i.e., September 2009) and December 2017 were summed and averaged.

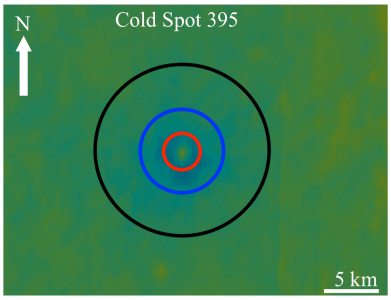

Figure 2: DIVINER nighttime temperature map of cold spot 395 (-7.1993°, -113.61°) with annuli used in analysis. The red annulus circles the center crater with elevated temperatures, the blue the cold spot regions and the black the surrounding terrain.

For the cold spot analysis, a comparison was performed between the spectral slopes of the cold spot regions, the surrounding areas, and the center young crater. Three annuli were used to isolate each of the three regions and extract the average FUV spectra, as shown in Figure 2. The spectra were then normalized at 154 nm, since the region between 160 and 190 nm is diagnostic to regolith maturity, i.e., spectra show redder slopes at this wavelength range for less space weathered, more immature areas. For the new impact crater study, the annulus approach was also utilized to extract the data from the crater region, and the average albedo at 165 nm over a 5km diameter annulus as a function of distance was plotted before and after the impact.

Results and Discussion: *Cold Spots.* The cold spots investigated in this study are listed in Table 1. For each cold spot, the spectra of the crater region, cold spot region and surrounding terrain were all plotted. Figures 3 and 4 show example spectra for two cold spots, where the spectra over cold spot surfaces show a bluer spectral slope compared to the fresh crater, but a redder slope than the surrounding terrain. Investigation of cold spots listed in Table 1 showed consistent spectral slope differences between cold spot regions and surrounding terrain. The spectral slope in FUV is indicative of space weathering, and therefore regolith maturity. The longer the regolith is exposed to the surface, the more space weathering it endures, and therefore the region appears more mature. Space weathering results in a bluer spectral slope in FUV wavelengths due to the formation of opaque nanophase iron particles [7]. These results imply that the cold spot regions are less mature than the surrounding regolith but more mature than the fresh crater. This is even more distinct for cold spots with high H parameters. For example, cold spot 395 has a higher H parameter value than cold spot 2349, and shows a larger difference in maturity between the cold spot regions and surrounding terrain (see Figures 3 and 4). In contrast, analysis on fresh craters without cold spots showed no corresponding trend.

Cold spot index	Longitude (°)	Latitude (°)	Diameter (km)	H Parameter
2084	109.185	8.09573	0.426	0.1537
395	-113.61	-7.1993	0.421	0.1505
1960	90.766	-5.3947	0.884	0.1222
2239	135	7.71	0.220	0.0085
336	-122.83	4.76924	0.287	0.0846
383	-114.85	0.49368	0.526	0.0674
171	-152.25	0.86864	0.602	0.0554
2349	151.684	-4.0819	1.538	0.0524

Table 1: Table showing properties of cold spots investigated. H parameter values were derived from DIVINER global albedo maps.

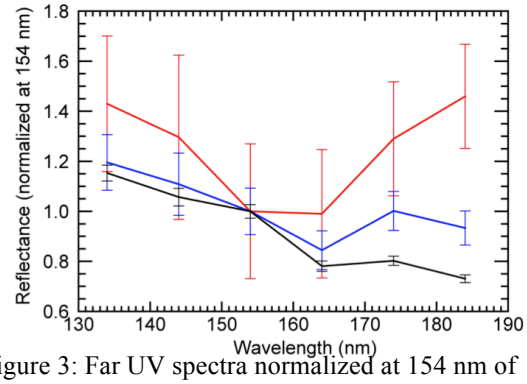

Figure 3: Far UV spectra normalized at 154 nm of three annuli from cold spot 395. Red is over center fresh crater, blue is over cold spot and black is over surrounding terrain.

New Impact Crater. A 70m new crater formed on Mare Humorum in October 2012 was analyzed. The LROC NAC images of before and after impact are shown in Figure 5 in which the dark ejecta and rays are evident in the after impact image. The top panel of

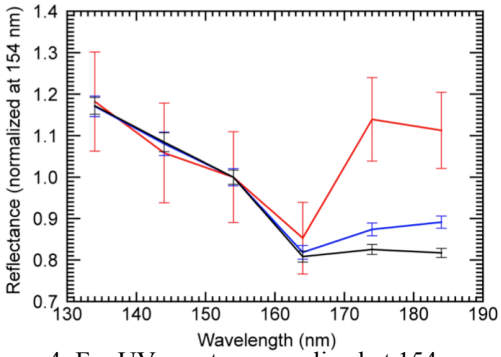

Figure 4: Far UV spectra normalized at 154 nm of three annuli from cold spot 2349. Red is over center fresh crater, blue is over cold spot and black is over surrounding terrain.

Figure 6 shows that, after impact, the albedo at 165 nm increases significantly especially within 100km radius of the impact. The bottom panel of Figure 6 shows that the albedo difference of before and after impact generally decreases with increasing distance, but the

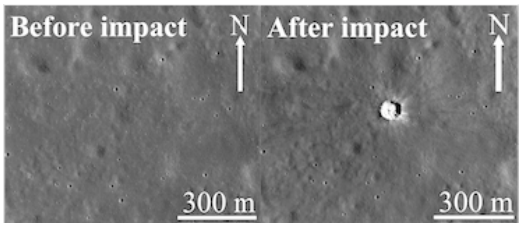

Figure 5: Left panel: Before impact at -22.3518°N, 320.2704°E. Right panel: After impact, showing the new 70m crater in the center. Images courtesy of Mark Robinson and the LROC team.

differences are even visible at 150 km away from the impact, indicating the great influence of the impact during the formation of this 70m crater. Since FUV light can only penetrate the top tens of nanometers of the regolith, LAMP might detect the more smaller scale materials which have been disturbed by impact processes, such as seismic shaking. Future work will include investigations of more new impact craters to see if similar albedo changes occur.

Conclusion and Future Work: In this study, several cold spots in the FUV wavelengths were investigated, and distinct spectral differences between cold spot surfaces and surrounding terrains were found. FUV spectra show that cold spot regions are more mature than the center fresh crater but less mature than the surrounding regolith. The results indicate that FUV data are likely to be more sensitive to the subtle changes in regolith maturity over the cold spot surfaces than visible and near infrared wavelengths. Thus these spectra might capture the materials' degradation processes due to space weathering. The new 70m impact crater identified by the LROC instrument was also investigated. The results show an overall increase in albedo after impact and an obvious albedo difference even at 150 km away from the impact. This could be interpreted to be due to the disturbance of lunar regolith by seismic shaking at a great distance during the impact.

Future work will include investigation of more cold spots and new impact craters using the LAMP FUV data. Further investigations will be carried out exploring the link between H parameter and cold spot maturity. LAMP nightside Lyman alpha albedo maps will

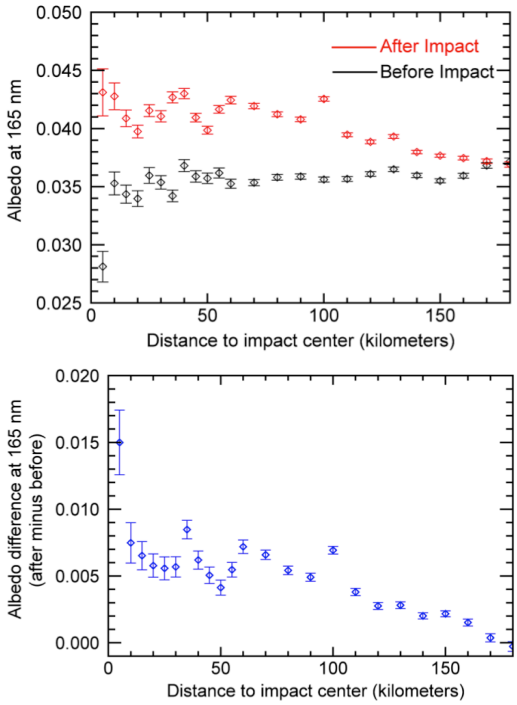

Figure 6: Top panel: Black data points (by summing 24 month data) are albedo before impact, and red data points (by summing 53 month data) are albedo after impact. Bottom panel: Albedo difference before and after impact. Both data are from a new 70m impact crater at -22.3518◦N, 320.2704◦E at a wavelength of 165 nm over a 5km diameter annulus.

also be explored and used to constrain the regolith porosity changes resulting from ejecta emplacement.

References: [1] J. L. Bandfield et al. (2014) Icarus 231 pp.221–231. [2] E. J. Speyerer et al. (2016) Nature 538 pp.215-218. [3] T. M. Powell et al. (2018) Lunar and Planetary Science Conference, LPI Contrib. No. 2083. [4] P. O. Hayne et al. (2017) JGR Vol. 122 pp. 2371-2400. [5] G. R. Gladstone et al. (2010) Space Science Reviews 150.1, pp.161–181. [6] Y. Liu et al. (2018) Lunar and Planetary Science Conference. Vol. 49. p. 2089. [7] A. R. Hendrix et al. (2016) Icarus 273.

Petrology and Geochemistry of Lithic Fragments in Elephant Moraine 79001. E. C. Kuehl [1,2], N. Castle[2], J.H. Jones[2], [1]Department of Earth and Planetary Sciences, Washington University in St. Louis, St. Louis, MO 63130 (ethan.kuehl@wustl.edu), [2]Lunar and Planetary Institute, 3600 Bay Area Blvd, Houston, TX 77058

Introduction: Elephant Moraine (EET) 79001A is a shergottite (i.e. Martian) meteorite that consists of four previously recognized lithologies: A, B, C, and X. Lithology A has been classified as an olivine-phyric basalt with a fine-grained (~0.15 mm) pyroxene-plagioclase groundmass, with entrained olivine ± orthopyroxene megacrysts (0.5-3.3 mm). Lithology B is a basaltic shergottite with a relatively coarse-grained (~0.30 mm) groundmass [1, 2]. The two lithologies are separated by an igneous contact [3]. Lithology C is comprised of shock melt veins and pockets, and is intertwined throughout lithologies A and B [4]. The olivine megacrysts and lithic fragments entrained in lithology A are believed to be xenolithic in origin [1-3,5], and comprise lithology X.

Previous work has closely examined the chemistry of a limited number of clasts and grains within lithology X [1-3,5,6] but a full description of the lithology has never been a major focus. In this study, we establish the major and minor element chemical zoning of olivine megacrysts and olivine-orthopyroxenite xenolith clasts within lithology A in an attempt to better establish the nature of lithology X. Our aim is to determine the compositional range of mineralogy in lithology X, and to evaluate whether the collection of olivine megacrysts and xenolith clasts originate from a single source lithology.

Methods: Seven thin sections of EET 79001A (68, 88, 441, 453, 494,, 555, and 556) were obtained from curation at the Johnson Space Center (JSC). Optical microscopy was used to identify xenocrysts and clasts within the thin sections. Backscatter electron (BSE) images were acquired using the JEOL Scanning Electron Microscope (SEM).

Mineral and glass compositions were determined using electron microprobe analysis (EMPA) on both the Cameca SX-100 and JEOL 8530F at JSC by wavelength-dispersive spectroscopy (WDS). EMPA was calibrated using well-characterized mineral standards. Olivine, pyroxene, and spinel were analyzed using a 20 keV accelerating voltage with a 20-30 nA current and a 1 μm beam diameter. Feldspar composition glasses (maskelynite) were analyzed using a 15 keV accelerating voltage with a 10 nA current and a 5 μm beam diameter.

Results: Lithology B can be readily distinguished from lithology A in BSE images and under a light microscope based on texture, as lithology B is generally coarser with tabular plagioclase. Olivine is readily identified by interference color in cross-polarized light; clasts typically contain olivine and are distinguishable from lithology A groundmass by the massive pyroxene morphology and lack of significant plagioclase. Clasts can be easily identified in BSE images by the presence of dark pyroxene with chaotic zoning. Olivine within xenolith clasts was found to be smaller (0.5-0.8 mm) than typical individual olivine megacrysts.

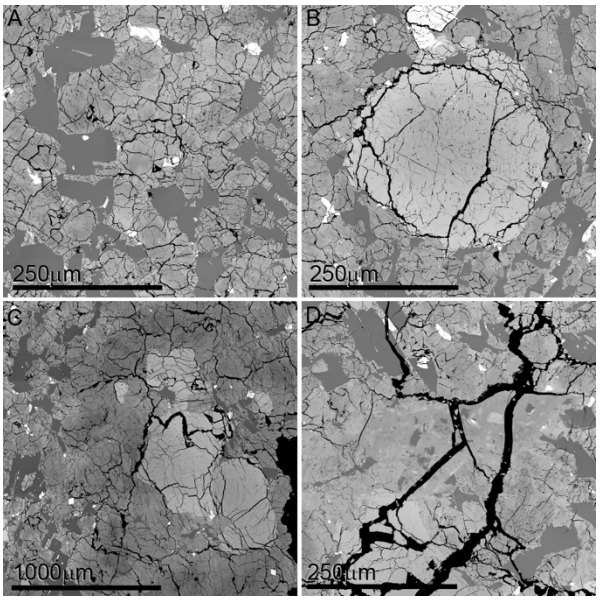

Figure 1: BSE images of EET 79001. (a) Lithology A groundmass consisting of pyroxene (brighter gray) and maskelynite (darker gray). (b) Olivine xenocryst (brighter gray) entrained within lithology A. (c) Clast entrained within lithology A comprised of anhedral olivine surrounded by chaotically zoned pyroxene. (d) A pocket of shock melt (lithology C) contained in lithology A [7].

Twenty-two olivine xenocrysts and four clasts were analyzed. Five distinct olivine populations were identified: two common populations comprised the majority of olivine megacrysts and olivine within xenolithic clasts, and three unique grains—two megacryst and one olivine within a xenolith clast in section ,453—were distinct from the common populations. The distinctive olivine grain from the xenolith clast is substantially different from the other olivines in xenolith clasts both chemically and morphologically. Most olivine in xenoliths are anhedral; the distinctive grain is euhedral. Further, it has very little major element variation [Mg#

60-66 (62-64, ~1.5σ)], whereas the typical olivine in xenolith clasts have extensive major element zoning (Mg# 53-78). All of the olivine measured, including the distinct grains, has high CaO cores with low CaO rims. The lack of Mg# zoning in the distinctive olivine results in a nearly vertical CaO/Mg# trend compared to the other olivine analyses (Fig. 3). Unlike the distinct olivine from a xenolith clast, the distinct olivine megacrysts are anhedral, like the majority of olivine in EET 79001A. Instead, the olivine megacrysts are distinct from the dominant population entirely because of their highly ferroan composition, narrow range of chemical zoning (Mg# 44-56 for the less ferroan and 41.6-44.9 for the more ferroan; Fig. 3), and their distinctive worm-like shape.

The pyroxene found within clasts is distinct from the pyroxene found within the lithology A groundmass in a number of ways. The clastic pyroxene has a more magnesian composition (Mg# 56.2-86.6) than the groundmass range previously reported (Mg# 43.7-73.1) [7]. The zoning pattern in the clasts is also distinct from the groundmass. The clastic pyroxene has chaotic zoning, apparent in BSE images. It consists primarily of very dark anhedral cores zoning out to bright ferroan rims with no obvious grain boundaries. All of the pyroxenes within the clasts are completely anhedral, coming close to looking like flow features. The cores and rims of the groundmass pyroxenes, by contrast, are brighter and therefore more ferroan. Unlike the clast pyroxene, the groundmass has a more gradual change in composition from the core to the rim, giving rise to patchy zoning that is consistent with rapid cooling of the basaltic groundmass. Pyroxene megacrysts in lithology B have normal zoning with the more magnesian cores surrounded by ferroan rims (Mg# 34.7 -75.9).

A xenolithic pyroxene was observed partly enclosed by a typical olivine megacryst. Unlike the general xenolithic pyroxene, this unique pyroxene grain has no apparent zoning (Mg# 57.1-59.2) and does not enclose the olivine grain. The shape of this grain suggests that it crystallized with the olivine, being partially included, but the rest of the grain was removed during the process that assimilated the xenolith into the lithology A groundmass.

Discussion: Six separate lithologies were found to exist within five olivine and two pyroxene populations. Olivine megacryst populations have contact with the lithology A groundmass, whereas the xenolithic clasts enclose the olivine. A petrographic survey of the olivine megacrysts reveals that they are in sharp contact with the lithology A groundmass, suggesting that they are in disequilibrium with the magma that crystallized lithology A. While all of the megacrysts display the same disequilibrium features, not all of the olivine megacrysts represent the same lithology, as discussed above.

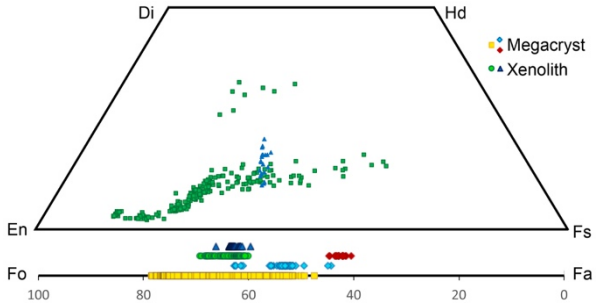

Figure 2: Major element compositions of olivine and pyroxene in lithology X.

Similarly, olivine found within xenolithic clasts are enclosed with pyroxene, but not all of these olivine crystals seem to have the same relationship to the pyroxene. The five populations of olivine identified represent five separate lithologies within lithology X, with each population having distinctive crystalline shapes and ranges in Mg# (Figure 3). The general olivine megacryst population has the widest range in Mg#. The olivine within xenolith clasts has a narrower range in Mg#, but is otherwise similarly zoned to the olivine megacrysts. The three distinct olivine grains almost entirely lack Mg# zoning; they are also chemically distinct from each other, with the euhedral olivine in a xenolith clast being much more magnesian than the distinctive anhedral olivine megacrysts. The fact that the olivine grains exhibit a larger range in Mg# further solidifies the argument that the highly magnesian pyroxene surrounding olivine grains are xenolithic rather than pyroxene armoring the olivine grain. Olivine grains armored by pyroxene suggests that the olivine would have been in direct contact with the groundmass because they and therefore would have had a range in Mg# similar to the general olivine megacryts lithology. A hypothetical liquidus olivine grown from the Lithology A groundmass would have had an Mg# of ~70., but most of the olivine xenocrysts are more evolved and have lower Mg#'s (Fig. 3)

A petrographic survey of the xenolithic clasts reveals that the pyroxenes in contact with the groundmass are also in disequilibrium. The common clastic pyroxene is more primitive than the groundmass pyroxene cores, suggesting that the pyroxene did not originate from the same melt as the groundmass. The relation between the pyroxene and the olivine found within the clasts also suggests that not all of the pyroxene in the clasts have the same relationship to olivine. This can be seen in the shapes and chemical diversity

of the two olivine xenolith clastic lithologies: both clastic olivine lithologies are enclosed by the same pyroxene lithology, but the common clastic olivine has anhedral shapes whereas the compositionally homogenous olivine has a euhedral shape. Trace element analyses are required to determine why this is the case.

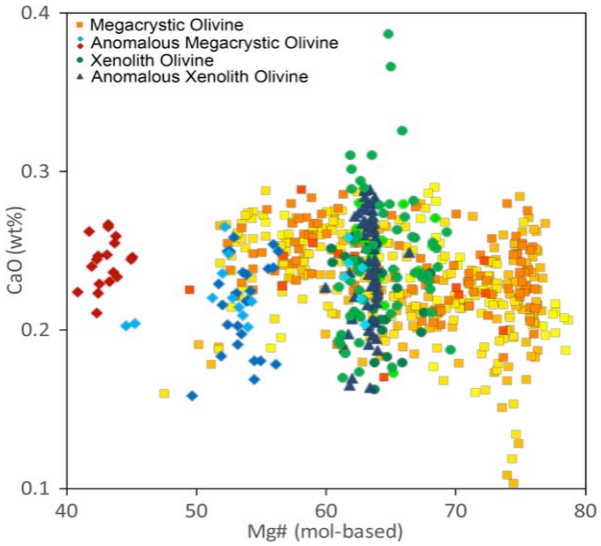

Figure 3: Plot of CaO vs. Mg# for olivine clasts and xenocrysts.

A second pyroxene lithology consisting of one pyroxene grain was discovered within the xenolithic pyroxene population. This unique pyroxene grain has no zoning and does not enclose the olivine grain it is beside, whereas the general xenolith clastic pyroxene is chaotically zoned and completely encloses the olivine grain. Also, unlike the other clastic pyroxene population, the olivine including the pyroxene is in direct contact with the lithology A groundmass, and chemically consistent with the general megacryst trend instead of the xenolith olivine trend. The presence of this unique grain suggests a different lithology grouping (i.e. neither an olivine megacryst nor xenolith clast) from those previously discussed. One trend that both xenolith clastic pyroxene with Mg# greater than 75 and the unique pyroxene grain have in common is a nearly vertical trend of Al_2O_3 vs Cr_2O_3. Goodrich suggests this trend is indicative of a disequilibrium feature and with the magma they were introduced to [1]. This further corroborates that the unique pyroxene grain is not native to the lithology A groundmass but xenolithic in nature.

The xenolith and megacryst grouping in EETA79001 has a modal mineralogy that is broadly consistent with a harzburgite or olivine-pyroxenite, but with substantially more compositional heterogeneity than previously described. Six independent lithologies were determined to exist within this grouping, but they can be broken down into 3 lithologic groups based on mineral type and relation to the lithology A groundmass:

1) Megacryst olivine
   a. The common xenocryst lithology with a broad Mg# range.
   b. The intermediate olivine megacryst lithology that is slightly less ferroan, and has a larger Mg# range than the most ferroan olivine megacryst.
   c. The most ferroan olivine megacryst lithology.
2) Xenolith clast olivine
   a. The common xenolith clastic olivine lithology that represents the largest number of olivines in clasts, and has a larger Mg# range than the unique olivine xenolith clast lithology.
   b. The compostitionally homogeneous olivine grain found in the ,453 xenolith clast.
3) Xenolithic clast pyroxene
   a. The unique pyroxene grain that has a narrow Mg# range compared to the common clast pyroxene.

Implications Analyses of pyroxene and olivine in lithology X have revealed a more complicated history of EET 79001A than previously described. Olivine megacrysts and xenolithic clasts are not one cohesive lithology, but are comprised of several sublithologies. Four olivine lithologies and two pyroxene lithologies have been described in this paper, but more sublitholgies may exist. Previous studies have focused on establishing the relationship between lithologies A and B, and between A and X, but more work needs to be done to establish the relationship between the sublithologies within lithology X. These relationships will help develop a greater understanding of the meteorite's origin and will further help constrain the composition of the lithology A parental melt. Additionaly, these xenoliths represent a new suite of related lithologies that will help extend our understanding of Martian petrogenesis. Further study is required to determine their origin, but the presence of plagioclase in these xenoliths suggests that they formed within the plagioclase stability field (<10 kbar), and therefore represent a cumulate lithology rather than samples of the deep Martian mantle.

References: [1] Goodrich C.A. (2003) *GCA, 67,* 3735-3771. [2] Mcsween H. Y. and Jarosewich E. (1983) *GCA, 47,* 1501-1513. [3] Treiman A.H. (1995) *JGR, 100,* 5329-5340. [4] Walton E. L. et al. (2010) *GCA, 74,* 4829-4843. [5] Ma M.S. et al. (1982) *LPS XIII,* 451-452. [6] Herd C. D. K. et al. (2002) *Meteoritics & Planet Sci., 37,* 987-1000. [7] Mellin M.J. (2007) *University of. Tennessee-Knoxville Master's Thesis.*

CONSTRAINTS ON CRATER FORMATION AGES ON DIONE FROM CASSINI VIMS AND ISS. A. J. López-Oquendo[1,2], E. G. Rivera-Valentín[1], C.M. Dalle Ore[3]; [1]Lunar and Planetary Institute, Universities Space Research Association, Houston, TX, [2]University of Puerto Rico, Humacao, PR, andy.lopez2@upr.edu, [3]SETI Institute, Mountain View, CA.

Introduction: The inner Solar System cratering flux has been partially constrained by geochronological measurements of returned lunar samples and Martian meteorites combined with cratering studies [1-3]; however, the flux for the outer Solar System, here specifically the Saturn system, does not have such constraints. The cratering flux for the outer Solar System currently depends on dynamical simulations of early Solar System sculpting [4,5], cratering studies [6,7,8], and historical observations of cometary impacts [9]. However, recently [10] found that the amorphous ice ratio on the icy moons of Saturn can be used to date crater formation on their surfaces.

The Saturnian satellites are primarily water ice [11]. Specifically, the 1.65-µm band indicates the surface of the mid-sized moons (MSMs) of Saturn contain hexagonal water ice [12]. During a hypervelocity impact onto such an icy moon, a shallow melt region is produced [13,14]. Crystalline ice then forms from the flash heating and cooling of the exposed melt [16]. Several of the Saturnian MSMs orbit within Saturn's magnetosphere. Because the magnetosphere revolves much faster than the MSMs orbit Saturn, their trailing hemispheres are preferentially exposed to ion bombardment. Over time, bombardment by ions and micrometeorites disrupt the crystalline structure of the impact-melt produced ice resulting in amorphous water ice [16]. The rate of this transition depends on the ion bombardment flux, which has been measured by Cassini [17]. Therefore, the amorphous ice ratio can be used to constrain the formation age of craters on the Saturnian MSMs.

Here we follow the work by [10] for Rhea and apply it to Dione in order to study the global ice phase distribution to provide new estimates on crater formation ages independent of cratering rate models and cratering statistics. These ages, united with crater counts, can provide new constraints on the cratering rate of the Saturn system and by extension the outer Solar System.

Ice Phase Distribution: H_2O ice phase can be determined based on a few key differences in the spectral signature. The most obvious and commonly adopted is the depth of the 1.65-µm band. In the case for the presented data, we are precluded from using this band as it corresponds to one of the Cassini instrument filter junctions. Furthermore, the band is highly biased by the presence of even traces of crystalline H_2O ice [16] and so does not yield a precise measure of ice phase fraction. We therefore adopt the 2.0-µm band whose shape is affected by changes in phase [12] in a consistent way. The techniques by [10], which are briefly described here, are then applied on a global scale to measure the amorphous ice fraction on Dione.

Spectral data is clustered to find terrains of like spectral signatures. Here, we made use of a clustering tool based on a k-means supervised classification scheme modified by [18-20]. This tool was modified by consolidating its scripts and performing code optimization in order to develop a new "user friendly" clustering driver code. The clustering routine now successfully finds the optimal number of necessary clusters to classify the spectral categories in order to investigate terrains of like spectral features.

Based on the study by [12], the 1.5 and 2.0 µm bands can be modeled by a combination of 5 and 3 Gaussians, respectively. Variations in the ice-phase affect the relative strength of the Gaussians that compose these bands [21]. The asymmetry of the modeled Gaussian fit to the spectra defines the so-called 'delta' function, which varies systematically with changes in the relative amounts of crystalline and amorphous water ice. This 'delta' function is mapped across Dione to infer its global amorphous ice fraction.

Results: The resulting global amorphous ice fraction map for Dione is shown in Figure 1, following a clustering of 30 spectral categories of the 1.5 µm band, differing in composition, grain size, and temperature. The color bar shows the amorphous water ice fraction (φ) from brightest regions (less amorphous ice) to darkest regions (more amorphous ice fraction). On average, globally, the amorphous water ice fraction is 0.43±0.21, with a range of $0.07 \leq \varphi \leq 0.9$.

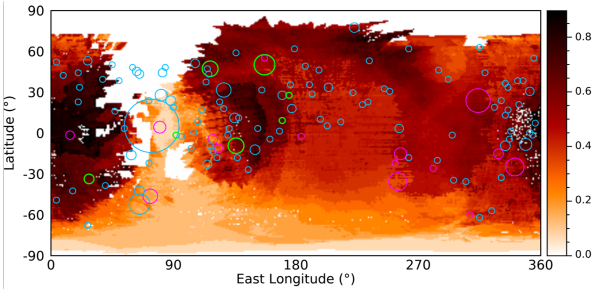

Figure 1. Global ice phase map of Dione. This map, based on 30 spectral clusters, shows the global surface distribution of amorphous ice fraction, with light colors representing low values and dark colors representing high values. Areas where data is not available is shown in white. In circles, we show the craters with diameters greater than 30 km (cyan), from which 22 craters passed our statistical test (magenta), out of which 6 craters were selected for age analysis (green) following our criterion and data requirements.

Due to the hemispheric asymmetries observed on Dione (*e.g.*, the wispy terrain is on the trailing hemisphere), we investigated the distribution of amorphous water ice fraction on the leading and trailing hemispheres. In Figure 2, we show the amorphous water ice fraction population per hemisphere and globally using a bin size of φ = 0.05. The surface coverage per φ is defined as the total number of pixels within the bin relative to the total number of non-zero pixels.

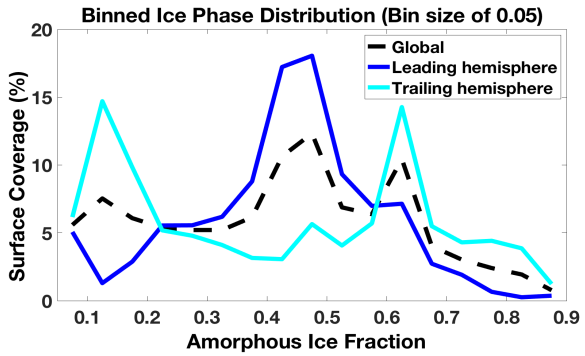

Figure 2. Global ice phase distribution over Dione's surface. Data is binned into boxes of size 0.05 in amorphous ice fraction and normalized to the number of nonzero pixels. The dashed black line is the global distribution, while the cyan and blue lines are the hemispheric distribution for the trailing and leading hemispheres, respectively.

As seen in Figure 2, the ice phase distribution between the hemispheres are significantly different from each other. The leading hemisphere follows well a Gaussian distribution centered around the mean value of 0.5 while the trailing hemisphere follows a bimodal distribution with peaks at φ = 0.13 and 0.63. This leads the global distribution to have a three peaked distribution with a gentle downslope towards high amorphous ice fractions. Though there is a striking and statistically significant difference in terms of amorphous ice fraction distribution between the hemispheres, the hemispheric average φ are statistically indistinguishable. The lowest φ values are primarily located in the south pole and along the chasmata on Dione; therefore, this terrain is correlated with high crystalline ice abundance.

Crater Aging: In order to find craters that are the best candidates for ice phase inferred aging, we paired the produced ice phase map with cratering studies on Dione [8]. Several criterion are required in order to infer crater ages: (*1*) There should exist a correlation between the ice phase distribution and the crater event itself. This is best quantified by a significant difference between the average ice phase in the crater floor and its continuous ejecta blanket. (*2*) The crater should lie on the trailing hemisphere, where charged particles preferentially impact and Cassini constraints on ion flux exist. (*3*) Sufficient data within and surrounding the crater is required in order to conduct the dating study. We choose the criterion such that ≥50% of both the inside and outside of the crater contains ice phase data. (*4*) As discussed previously, there is a noted alteration of the ice phase associated with the wispy terrain; therefore, we restrict our search to craters outside of the chasmata.

To test for our first criterion, we developed a statistical code using the two-sample *z* test, which follows

$$z = \frac{|\bar{\varphi}_i - \bar{\varphi}_o|}{\sqrt{\left(\frac{\sigma_i}{n_i}\right)^2 + \left(\frac{\sigma_o}{n_o}\right)^2}} \quad ,$$

where $\bar{\varphi}$ is the average amorphous ice fraction, σ is the standard deviation, n is the number of pixels, and the indices i and o represent the values for inside and outside of the crater. Our null hypothesis assumes the mean values are indistinguishable. The test is conducted to a 99% confidence. In Figure 1, craters that pass the *z* test are shown in magenta color while craters that also pass criterions 2 – 4 are show in green.

The best candidate craters are then further studied to obtain an ice-inferred formation age. Using the global ice map, we obtain the average amorphous ice fraction inside the crater and in the respective ejecta blanket as well as the range of φ values. We used the equation provided by [15], which describes the rate of transformation of H_2O ice from crystalline to amorphous due to irradiation by charged particles of different masses and follows an exponential behavior, such that the time (t) required to transform from crystalline to amorphous ice is given by

$$t = -\ln\left(1 - \frac{\phi_A}{\phi_{A_{max}}}\right) * k^{-1}F^{-1} \quad ,$$

where k is a fitting parameter strongly dependent on the surface temperature, F is the irradiation fluence, ϕ_A is the typical fraction of amorphous ice related to the crater, and $\phi_{A_{max}}$ is the maximum fraction of amorphous ice related to the crater. This relation was derived on the basis of a number of laboratory experiments by several groups who had used charged particles, UV irradiation, and electrons to bombard crystalline water ice and had measured the rate of ice phase transformation. Because the selected craters are in the trailing hemisphere, we assume they are predominantly bombarded by protons [22]. For the trailing hemisphere of Dione, we calculated the irradiation dose from the proton flux by [17], and define k=0.18 from [15, fig.16.3], giving kF = 0.0034 Ma^{-1}. The resultant kF was also adjusted for the number of H_2O molecules in a volume 1 cm^2 wide and 8 μm deep, where 8 μm is half the penetration depth for 0.8-MeV protons [16], relevant for Dione.

Results. The ages of the analyzed craters are presented in Table 1. The named craters are *Latinus*, *Allecto*, *Acestes*, *Silvius*, and *Coras* respectively in order of decreasing diameter. Because the other two craters are unnamed, we designate them as RL1 and RL2

respectively in order of decreasing diameter. The studied craters have ages ranging from ~ 80 Ma to 1 Ga, all younger than the proposed Late Heavy Bombardment. The ice phase correlation around older craters may be degraded by repeated and overlapping impacts, thus our *z* test has a selection bias against such craters. Furthermore, Allecto crater was previously found to be rather young given its low superposed crater density on its floor [8], which agrees well with our derived age, giving confidence to the technique.

Table 1. Ages for the studied best candidate craters.

Diameter (km)	Latitude (°)	East longitude (°)	H_2O-ice fraction (%)	Age (Ma)
133	52.5	157.3	53	400 ± 170
101	-7.6	135.8	56	350 ± 120
100	50.3	117.0	62	430 ± 140
63	-32.6	28.1	66	500 ± 150
41	0.5	92.1	8	120 ± 40
32	10.9	169.9	66	1050 ± 300
32	29.7	175.4	54	1030 ± 300

Discussion: An interesting feature of the global ice phase map (Figure 1) and the distribution of amorphous water ice fraction (Figure 2), is the potential association between high abundance of crystalline water ice and Dione's wispy terrain. The chasmata very closely follow areas of low φ, potentially suggesting that if the association is causal then a heating event, which may have occurred along with wispy terrain formation, led to the alteration of near-surface water ice. If ion bombardment indeed dominated the ice phase distribution on the leading hemisphere, then the distribution should more closely resemble a Gaussian, similar to that on the leading hemisphere. We interpret this deviation from the expected distribution as evidence for a process that has been superposed on the ion bombardment.

The studied crater Allecto has a superposed cumulative crater density on its floor for craters larger than 1 km of $N(1\text{ km}) = 0.026 \pm 0.002$. With an inferred age of 350 ± 120 Ma, the inferred cratering rate is 7.4 (±2.6) × 10^{-5} per 10^6 km^2 per year. Early studies on the bombardment of the outer solar system found two distinct populations for the Jovian system and Neptune's Triton [9]. Specifically, the Jovian moons were found to be deficient in small craters compared to Triton. Furthermore, recent work has also found the Uranian moons and the Pluto system have crater populations deficient in small craters (*i.e.*, Jupiter-like; [23]). The inferred cratering rate from these two impactor populations, named Case A for Jupiter-like and Case B for Triton-like, have distinct cratering rates [9]. Case B would follow a cratering rate on the order of 10^{-5} per 10^6 km^2 per year while Case A would follow 10^{-6} per 10^6 km^2 per year. Our inferred cratering rate from Allecto, best agrees with Case B (*i.e.*, Triton-like). Indeed, this case is further supported by the distribution of small craters on the MSMs [7,8] and from the ice-inferred age of Rhea's Obatala [24].

Conclusions: Recently, [10] found that the surface amorphous water ice fraction (φ) can be inferred for the Saturnian satellites using Cassini data. Furthermore, [10] found that the local φ associated with craters can be used to date their formation. Applying this technique to Dione, we investigated the global distribution of φ on its surface and dated selected craters. We found a global average amorphous ice fraction of 0.43±0.21 with a range of $0.07 \leq \varphi \leq 0.9$. Our population study indicates the leading and trailing hemispheres are significantly different from each other. The leading hemisphere shows a Gaussian distribution around a mean value of 0.5 while the trailing hemisphere shows a bimodal distribution with peaks at φ = 0.13 and 0.63, potentially indicating alteration caused by the wispy terrain.

Via a statistical *z* test along with other criterion, we selected craters for aging; seven craters were dated in this study. Crater ages vary from ~ 80 Ma to 1 Ga, younger than the proposed Late Heavy Bombardment. Of note, the formation age for Allecto (350 ± 120 Ma) along with its superposed cumulative crater density suggests a cratering rate of 7.4 (±2.6) × 10^{-5} per 10^6 km^2 per year. This value is consistent with a population enriched in small projectiles compared to the Jovian system [9]. This agrees with crater population studies on the MSMs [7,8] and previous rate estimates from the ice inferred age of Rhea's Obatala [24].

Acknowledgments: This material is based upon work supported by NASA partially through the LPI Summer Internship Program and through the Cassini Data Analysis Program under Grant No. NNX17AG01G.

References: [1] Cohen, B. A., *et al*. (2005) *Meteor. & Planetary Science* 40 (5), 755-777. [2] Culler, T. S. (2000) *Science* 287 (5459), 1785-1788. [3] Frey, H. (2008) *GRL*. 35, L13203. [4] Gomes, R., *et al*. (2005) *Nature* 435, 466-469. [5] Tsiganis, K., *et al*. (2005) *Nature* 435, 459-461. [6] Dones, L., *et al*. (2009) in *Saturn from Cassini-Huygens*, Springer, eds. M. K. Dougherty *et al*. pp. 613-635. [7] Kirchoff, M. R. and Schenk, P. (2010) *Icarus* 206, 485-497. [8] Kirchoff, M. R. and Schenk, P. M. (2015) *Icarus* 256, 78-89. [9] Zahnle, K., *et al*. (2003) *Icarus* 163, 263-289. [10] Dalle Ore, C., *et al*. (2015) *Icarus* 261, 80-90. [11] Matson L.D. *et al*. (2009) in *Saturn from Cassini-Huygens*, Springer, eds. M. K. Dougherty *et al*. pp. 574-609. [12] Grundy, W.M. and Schmitt, B. (1998) *JGR. Planets* 103, 25809–25822. [13] Pierazzo, E. *et al*. (1997) *Icarus* 127, 408-423. [14] Stewart, S.T., *et al*. (2008) *GRL*. 35 (23). [15] Baragiola, R.A. *et al*. (2013) *The Science of Solar System Ices*, pp. 527–549. [16] Mastrapa, R.M.E. and Brown, R.H. (2006) *Icarus* 183, 207–214. [17] Paranicas, C. *et al*. (2012). *Planet. Space Sci*. 61, 60–65. [18] Marzo, G.A. *et al*. (2006) *JGR*. 111. [19] Marzo, G.A. *et al*. (2008) *JGR*. 113. [20] Marzo, G.A., *et al*. (2009) *JGR*, 114. [21] Mastrapa, R.M.E., *et al*. (2008) *Icarus* 197, 307–320. [22] Moore, J.M. (1984) *Icarus* 59, 205–220. [23] Singer K. N., *et al*. (2018) *Icarus* 306, 214-224. [24] Rivera-Valentín E.G. *et al*., (2018) *LPSC* 49. Abstract #2083.

Potassium-feldspar Bearing Main Group and Stannern Group Eucrites: Petrographical and Geochemical Investigations of Mafic Crust Formation Processes on Vesta Devin R. McQuaig[1], Justin I. Simon[2], David W. Mittlefehldt[2] Rosalind M.G. Armytage[3], [1]Department of Earth and Atmospheric Sciences, University of Houston, [2]ARES, NASA Johnson Space Center, [3]Jacobs/JETS, NASA-JSC

Introduction: The howardite-eucrite-diogenite (HED) clan of meteorites represents a suite of mafic to ultramafic igneous rocks. They are linked together by similar O- isotope compositions [e.g.1] and likely originate from the same parent body. This small, differentiated body is widely accepted to be asteroid 4 Vesta, based on evidence from visible and near infrared reflectance spectra [e.g. 2]. HEDs represent the most abundant suite of igneous rocks available for study from an asteroidal body. Dating via short-lived isotopic chronometers indicate that differentiation occurred within 10 million years of the formation of the solar system [3-5] and can provide insight on the accretion and origin of planets [6].

Basaltic eucrites display diverse igneous to metamorphic textures that are consistent with endogenous crustal processes as well as impacts [7,8]. Basaltic eucrites have fine to medium-grained textures with mineralogy dominantly consisting of plagioclase, pigeonite, and augite with minor to accessory phases including spinel, ilmenite, troilite, Ca-phosphates, and sometimes Ni-poor metal [7]. The basaltic eucrites in this study also contain grains of potassium feldspar, which are not commonly noted in basaltic eucrites [e.g. 9].

Chemically, basaltic eucrites are divided into groups which are separated based on their Mg-number (=100*molar Mg/(Fe+Mg)), Ti abundance, and incompatible trace element (ITE) abundances [7,9-11]. Of the basaltic eucrites, the Main Group (MG) eucrites are the most abundant and demonstrate similar Mg-numbers (42-35) and ranges as an ITE enriched group called the Stannern Group (SG) [3]. The MG exhibits a relatively lower abundance of ITEs [7,9,10,12].

There are two prominent models used to explain the petrogenesis of these trends and, consequently, the geologic history of 4 Vesta. One is the magma ocean model [13-15] and the other is a partial melting of the Main Group that contaminates the eucritic magma to form the Stannern Group [9,7,12]. The purpose of this study is to investigate the petrology and geochemistry of a few MG and SG samples to contribute to further test the formation hypotheses of the parent body of Stannern Group eucrites.

Samples: This study is part of a collaborative project utilizing several MG and SG eucrites, including thin sections of MG: BTN 00300,28; GRO 95533,6; and HOW 88401,37; and SG PCA 82501,19; and PCA 91179,9. EET 90020,44 may be a melt-residue related SG magma formation [16], while GRA 98098 is difficult to classify [17]. Here we focus on GRO 95533,6 and PCA 91179,9 due to the occurrence of potassium feldspar (K-spar) found in each sample. We also discovered K-spar in HOW 88401,37 and report its feldspar composition.

Main Group sample GRO 95533 has a discrete internal boundary. We refer to one side of the boundary as GRO 95533 N (because it was up, or the "north" side of the section map) while the other will be referred to as GRO 95533 S.

Methods: Carbon coated polished thin sections were examined using an Olympus BX 60 petrographic microscope. X-ray element maps were created utilizing a JEOL JSM-7600 F, field emission scanning electron microscope (SEM) at JSC. Back scattered electron (BSE) images were also created and false color element maps were layered over the BSE to identify areas of interest. Electron microprobe analysis (EPMA) was gathered on each mineral phase using the JEOL JXA-8530 F at JSC utilizing conditions of [18].

Results: *General Petrography.* Main Group eucrite GRO 95533 S is classified as being unbrecciated. It mostly displays a sub-ophitic to ophitic magmatic texture, but also has fragmental texture in places. Plagioclase grains are anhedral to subhedral with rounded edges on most grains. Carlsbad twinning is prevalent, a few grains have albite twins, but some grains have no visible twinning. Potassium feldspar grains are less than 9 μm and are not readily identifiable in optical microscopy. They populate areas of silica-rich mesostasis or are intergrown with plagioclase. Pyroxene grains demonstrate exsolution from low-Ca pyroxene to high-Ca pyroxene with lamellae of variable widths, thinning as the grain transitions to rim augite. A few small areas of pyroxenes display subequant granular growth with grains ranging from 100-250 μm. Low-Ca pigeonite is the dominant pyroxene phase. Silica is disseminated throughout with one area of intergrowth with high-Ca pyroxene, measuring ~1.5 mm. Oxide and iron sulfide phases are spread throughout and Ni poor iron metal grains are also present.

The same mineralogies are present in GRO 95533 N, but it has textural differences from GRO 95533 S. Plagioclase grains range from anhedral to nearly euhedral. Grains of K-spar are again found in areas associated with silica, especially where it is intergrown with

high-Ca pyroxene, but also along some fractures and within plagioclase grains. Potassium feldspar, high-Ca pyroxenes, and silica are more abundant in GRO 95533 N than the southern counterpart, with multiple areas of silica and high-Ca pyroxene intergrowth. Oxides are spread throughout, but ilmenite is much more abundant than spinel. Iron sulfides are more abundant than in the 'north' side. Only a few small Ni-poor iron metal grains are present, compared with several in the south portion of this sample.

Stannern Group, PCA 91179, is a brecciated eucrite that displays sub-ophitic to ophitic texture, areas of fragmentation, and clasts of various sizes. Fine to medium sized grains make up a lithology of predominantly high-Ca plagioclase and low-Ca pyroxenes. Plagioclase twinning is not as common as that of GRO 95533 (N and S). Although relatively scarce, K-spar is more abundant in PCA 91179 with two identifiable populations. The majority of the K-spar grains are found in mesostasis areas with high amounts of silica, pyroxene,oxides, and phosphates (Figure 1). Other K-spar grains are found alongside or appear to be included within plagioclase grains. Low-Ca pyroxenes all demonstrate exsolution of high-Ca pyroxene. A few low-Ca pyroxenes are coarse, but the overall pyroxene sizes are very fine to medium. Ilmenite is the most abundant oxide phase with fine grains spread throughout the sample. Spinel grains and iron sulfides are much less abundant than the other K-spar samples examined. One grain of oxidized iron metal was observed.

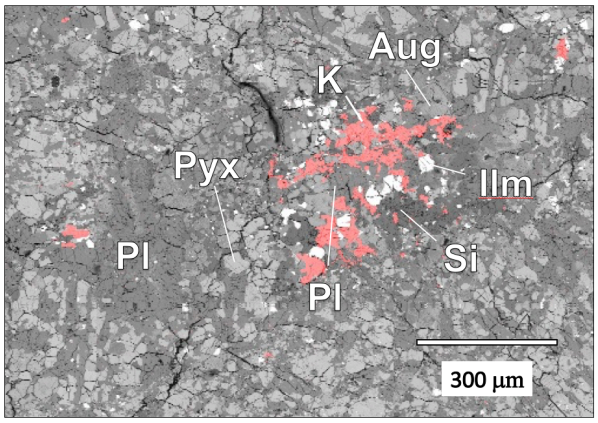

Figure 1. False color X-ray map (Red = K) overlain on a BSE of PCA 91179. (Aug: augite, Ilm: ilmenite, K: K-spar, Pl: plagioclase, Pyx: low-Ca pyroxene, Sil: silica). K-spar grains are concentrated near oxide, silica, pyroxene, and phosphate.

Mineral Compositions – Plagioclase. Plagioclase compositions are shown in Figure 2, plus fields of other samples in this collaborative study. The GRO 95533 S has a range of Ab_{8-13}, the smallest Ab range of the K-spar bearing samples. Plagioclase in GRO 95533 N has a wider range of albite content of Ab_{10-20}. HOW 88401 has the largest variance of all MG eucrites examined here with Ab_{8-20} in. The MG eucrite in this study, BTN 00300, has homogenous plagioclase grains with Ab_{10-11}. The SG eucrite, PCA 91179 has a variance of Ab_{12-21}. Eucrite GRA 98098 has a range of Ab_{7-12}. The SG related eucrite, EET 90020 displays more highly evolved metamorphic textures and has Ab_{9-13}. Patchy zoning of plagioclase is present in GRO 95533, HOW 88401, and PCA 91179, leaving some interior areas of the grain more sodic and some rims more calcic, which is verified by EMPA and shown in Figure 3.

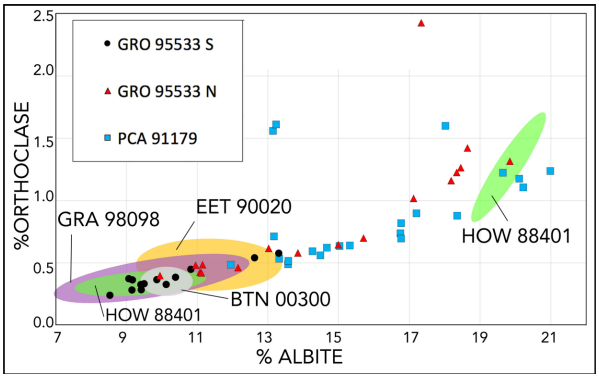

Figure 2. Point data from the EMPA is shown for GRO 95533, HOW 88401, and PCA 91179, plus fields of other eucrites examined in collaborative study.

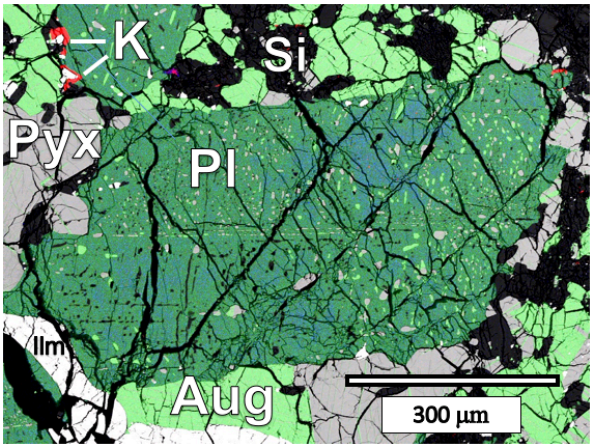

Figure 3. False color RGB X-ray map of a plagioclase grain in GRO 95533 N with patchy zoning. A few K-spar grains are also present in this image. (Aug: augite, Ilm: ilmenite, K: K-spar, Pl: plagioclase, Pyx: low-Ca pyroxene, Sil: silica) (Red = K, Green = Ca, Blue = Na)

Potassium Feldspar. Of the seven sections examined in this collabortive study, K-spar is only present in GRO 95533, HOW 88401, and PCA 91179. Within GRO 95533 S, the K-spar has a BaO content of 0.34 wt%. In GRO 95533 N, the BaO content is 0.66%.

The other MG eucrite, HOW 88401, has the least amount of K-spar with grains measuring less than 7 µm. The BaO content was much higherthan either GRO 95533 N or GRO 95533 S at 1.45%. The SG ecurite, PCA 91179, is the most abundant in K-spar with an average BaO content of 1.49%, (Figure 4). The orthoclase end member is high in each sample. 98.7 and 98.2 mole % in GRO 95533 S and N, 96.3 mole% in HOW 8840, and 96.8 mole% in PCA 91179.

Oxides	GRO 95533 S	GRO 95533 N	HOW 88401	PCA 91179
SiO_2	63.7	63.7	63.1	62.9
Al_2O_3	18.3	18.5	19.0	18.8
FeO	0.569	0.202	0.437	0.296
CaO	0.082	0.078	0.127	0.045
Na_2O	0.031	0.020	0.035	0.024
K_2O	16.2	16.2	15.8	15.9
BaO	0.343	0.656	1.447	1.486
Total	99.3	99.3	99.9	99.4

Figure 4. Average K-spar compositions for MG (first three) and SG PCA 91179.

Pyroxenes. Compositional plots for pyroxene in K-spar bearing eucrites are shown in Figure 5. Pyroxene phases present in all samples are pigeonite, and augite. Compositions are typical for MG and SG meteorites [e.g. 19].

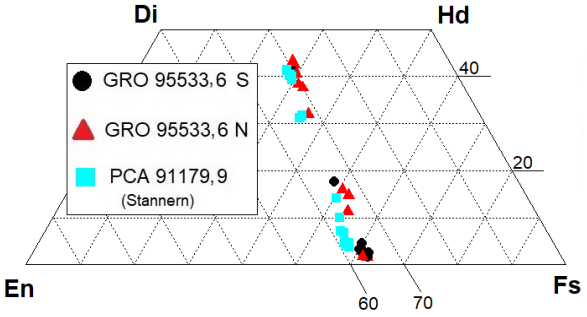

Figure 5: Pyroxene quadrilateral composition for GRO 95533 and PCA 91179. Compositions between the low and high-Ca pyroxenes are likely due to thin lamellae overlapped by the beam during EPMA.

Oxides. Spinels, ilmenites, and iron sulfides are present in all samples but only GRO 95533,6 S displays a grain over 1 mm in length. All other K-spar bearing samples have very fine spinel grains. Spinel compositions have narrow ranges in Al/Cr but wide ranges in Ti, as commonly observed for basaltic eucrites [7]. Every sample has ilmenite as the most abundant oxide phase. The ilmenites in all samples are homogenous with an average TiO_2 content of 51.7%. Some ilmenites share grain boundaries with spinels.

Discussion: Potassium feldspar is not commonly found in eucrites, but has been noted before in some clasts of Stannern Group eucrite NWA 4523 [e.g. 9]. The NWA 4523 K-spar was also found in intergrowths with plagioclase and in areas of mesostasis in association with silica, pyroxene, oxide phases, and sulfides [9]. Liquid immiscibility was proposed by [9] as an explanation for the texture in NWA 4523 and is a possible interpretation for our observations. Potassium feldspar is nearly pure in NWA 4523 as is the case for our samples, but [9] did not include analyses of BaO for comparison.

The BaO content of the MG HOW 88401 is similar to the SG PCA 91179 while the MG GRO 95533 N and S have much lower BaO contents. It would be reasonable to expect the SG eucrites to be more enriched in BaO if they are crystallizing from a contaminated melt of the MG. As noted before, the MG eucrites have relatively less ITEs and less minor incompatible elements, so the results of GRO 95533 N and S are not unexpected relative to PCA 91179. Conversely, the higher BaO content of HOW 88401 is unexpected. Given that K and Ba are both incompatible elements, it is surprising to find a MG's BaO having nearly the same amount found in a SG eucrite. If a partial melting model of the MG is a potential formation process of the SG, it seems that K-spar would be among the first mineral phases to melt. Partial melting of the MG would push K_2O and BaO, and into the melt, freeing those incompatibles to later redeposit into the ITE rich Stannern Group.

Future work could include investigating these counterintuitive BaO observations by conducting an expanded ITE study utilizing the ICP-MS at JSC.

References: [1] Scott E.R.D. et al. (2009) *GCA 73,* 5835-5853. [2] McSween H.Y. et al. (2013) *Meteoritics & Planet. Sci., 48,* 2090-2104. [3] Schiller M. et al. (2010) *GCA, 74,* 4844-4864. [4] Trinquier A. et al. (2008) *GCA, 72,* 5146-5163. [5] Touboul M. et al. (2008) *LPS XXXIX*, Abstract #2336. [6] Krot A.N. and M. Bizzarro (2009a) *GCA, 73,* 4919. [7] Mittlefehldt D.W. (2015) *Chemie der Erde-Geochemistry, 75,* 55-183. [8] Yamaguchi A. et al. (1996) *Icarus, 124,* 97-112. [9] Barrat J.A. et al. (2007) *GCA, 71,* 4108-4124. [10] Castle N. and C.D.K. Herd (2018) *LPS XLIX*, Abstract #2083. [11] Mayne R.G. et al. (2009) *GCA, 73,* 794-819. [12] Stolper E. (1977) *GCA, 41,* 587-611. [13] Neumann et al. (2014a) *Earth Planet. Sci. Lett., 395,* 267-280. [14] Righter K. And M.J Drake (1997) *Meteoritics & Planet. Sci., 32*, 929-944. [15] Warren P.H. (1997) *Meteoritics & Planet. Sci., 32,* 945-63. [16] Yamaguchi A. et al. (2001) *GCA 65,* 3577-3599. [17] Mittlefehldt D.W. (2016) *79th Annual Mtg of the Meteoritical Society,* Abstract #6324. [18] Mittlefehldt D.W. (2012a) *Meteoritics & Planet. Sci., 47,* 72-98. [19] Takeda H. and A.L. Graham (1991) *Meteoritics & Planet. Sci., 26,* 129-134.

TRACING A LUNAR MAGMATIC EPOCH THROUGH APOLLO 14 SAMPLES. Hannah C. O'Brien[1,2], Katharine L. Robinson[1], and David A. Kring[1], [1]Lunar and Planetary Institute, 3600 Bay Area Blvd., Houston, TX 77058; [2]Civil, Environmental Engineering and Earth Science Department, University of Notre Dame,156 Fitzpatrick Hall Notre Dame, IN 46556 (hobrien5@nd.edu).

Introduction: Roughly 4.4 billion years ago, the proto-Earth was struck by a large planetesimal, which led to the formation of our Moon. After that giant impact, the newly accreted Moon was surrounded by a global lunar magma ocean (LMO). As the LMO cooled and solidified, the density of minerals and the surrounding melt dictated whether phases sank to become a part of the mantle cumulate, or floated to form the lunar crust. [1,2]. These two major lunar lithologies are represented by the samples collected during the Apollo missions: Mare basalts formed by partially melting mantle cumulate, and the calcic plagioclase that floated to the top, forming the anorthosite-rich crust (or feldspathic highlands). Initial examination of the Apollo samples did not reveal weathering products and hydrous minerals - water was below instrumentation detection limits - and the Moon was believed to be dry [3]. However, recent research utilizing advanced analytical techniques has shown that not all water was lost during the volatile depletion, magmatic degassing and differentiation of the LMO and lunar formation [3,4]. In fact, the lunar interior has regions that contain as much water as the Earth's mid-ocean ridge basalts (MORBs) [5,6,7].

While there is still uncertainty about the true overall abundance of water in both the lunar interior and the surface, numerous studies of lunar volcanic glasses, melt inclusions, lunar apatite [$Ca_5(PO_4)_3(F,Cl,OH)$], and plagioclase from ferroan anorthosites have demonstrated that the Moon's interior contains water [5-8]. This has led to a reexamination of our understanding of the formation of our Moon.

Since 2008, analyses of water-bearing phases in lunar samples have primarily focused on pyroclastic glasses and mare basalts from younger mantle cumulates. Interestingly, more recent analyses of lunar samples coupled with numerical modeling suggest a period of enhanced magmatism circa 4.30-4.36 Ga may have been catalyzed by the impact event that produced the immense South Pole-Aitken impact basin [9], and an initial set of δD analyses of water bearing ~4.3 Ga rocks produced some of the lowest δD values measured thus far in Apollo samples [10].

Previous examination of lunar apatite, the only hydrous phase indigenous to the Moon, in these ancient highland samples (**Fig.1**), also suggested a correlation between age and δD [7]. Did this period of enhanced magmatism and the resulting processes tap a unique δD water reservoir or somehow fractionate a δD reservoir to produce the low values? For this investigation, we focus on Apollo 14 samples ranging in age from ~4.3-4.36 Ga. We have identified and characterized apatite and other phosphate minerals in Apollo 14 samples that will be targeted in subsequent analyses of H_2O, H, and Cl isotopes. Additionally, we located U-Pb carriers such as zircon which can be used to independently asses the ages of the samples for future comparison.

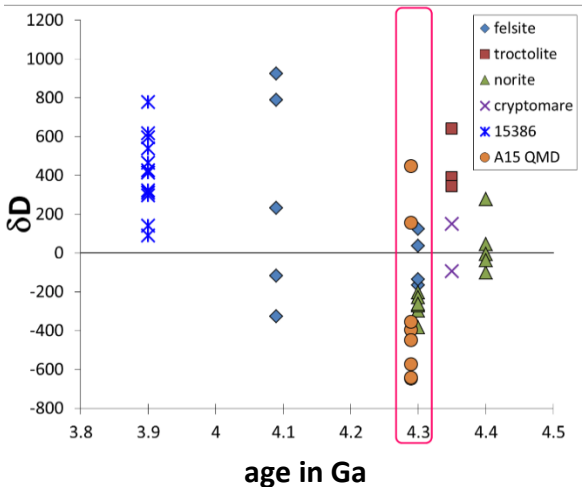

Figure 1: Plot of apatite δD versus sample age in Ga by rock type, including felsite, troctolite, norite, cryptomare basalt, KREEP basalt 15386, and Apollo 15 quartz monzodiorites (QMDs). The ages of a number of samples with low δDs cluster around 4.3 Ga. Data from Barnes et al. (2014), Robinson et al. (2016), Tartèse et al. (2014), Meyer et al. (1996), Carlson et al. (2014), Andreasen et al. (2013), Borg et al. (2013), and Terada et al. (2007).

Samples: We examined three Apollo 14 breccias during this study, including 14303,209; 14314,10; and 14306,60. All three samples likely originated from the Fra Mauro Formation (Imbrium ejecta) [20,21]. Clast-rich, crystalline-matrix breccia 14303,209 is a ~7.5 mm felsite ("granite") clast and is classified as pristine [11]. This sample is rich in K-feldspar, often intergrown with a silica polymorph, and plagioclase. Meyer et al. (1996) precisely dated the zircon in this granite clast to 4.308 ± .3 Ga [12].

Crystalline-matrix breccia 14314,10 contains a wide variety of clasts including mare basalt and annealed glass, and displays shock features in zoned olivine

xenocrysts [13]. An age has not yet been obtained for this sample.

Sample 14306,60 is a clast-rich, crystalline matrix breccia containing sodic ferrogabbro fragments. Apatite and large zircon grains are found in norite fragments, which have been dated to ~4.2 Ga by Compston et al. (1984), Meyer (1991), and Nemchin et al. (2008).

Methods: Initial study of the samples was conducted at the Lunar and Planetary Institute. Utilizing a petrographic microscope to determine mineralogy and gather textural context, images of the samples in plane polarized light and cross-polarized light were gathered and stitched together. Electron imagery and mapping was conducted at Johnson Space Center (JSC) with the JEOL field emission scanning electron microscope (SEM). Energy dispersive X-ray spectroscopy scans which detected characteristic X-rays maps for particular elements of interest were created. These raw element maps were then used to create false color maps [14]. Colors were assigned to each element, and the images combined using ImageJ **(Fig.2).** Combined P, Ca, and Fe maps as well as combined Al, Ca, Ti, Si, K, Fe, Mg maps were used to identify phosphate and zircon crystals and their distribution within each sample.

Silicate mineral chemistry was obtained using the Cameca SX-100 electron microprobe at JSC using a 15 kV, 20 nA beam. For phases susceptible to volatilization such as feldspars, the beam was defocused to 5 to 10 microns and the current reduced to 10 nA. Prior to analysis, the instrument was calibrated for Na, Mg, Al, Si, P, K, Ca, S, Ti, Fe, and Mn, using-characterized natural and synthetic mineral standards.

Phosphate chemistry was determined using the JEOL JXA-8530 electron microprobe. The instrument was calibrated for F, Na, Mg, Si, Ca, S, Ce, Cl, P, Sr, La, and Fe, using well-characterized synthetic and natural mineral standards. Fluorine was measured first to avoid volatilization during analysis.

Results and Discussion: *Sample 14303,209* is a crystalline matrix breccia [11], characterized as a large granitic clast by Warren et al. (1983). This sample contains multiple pyroxene phenocrysts with K-feldspar intergrowth. The largest pyroxene in this sample is surrounded by an exsolution silica polymorph and a large plagioclase clast. Sixteen phosphate crystals were identified in this sample. Of those phosphate crystals, seven of them may be suitable for ion microprobe (SIMS) analysis of H_2O, H, and Cl isotopes. As shown in **Fig.3**, a few of the apatite grains suitable for analysis present as an intergrowth or rim on merrillite grains, which our analyses revealed to be rich in rare earth elements (REE). REEs can be incorporated into merrillite due coupled substitution of $2REE^{3+}$ in Ca(B) sites + vacancy in Ca(IIA) for $2Ca^{+2}$ in Ca(B) sites and (Ca^{2+},Na^{+}) in Ca(IIA) [15].

14303,209, phosphate grains are typically surrounded by silica rich K-spar.

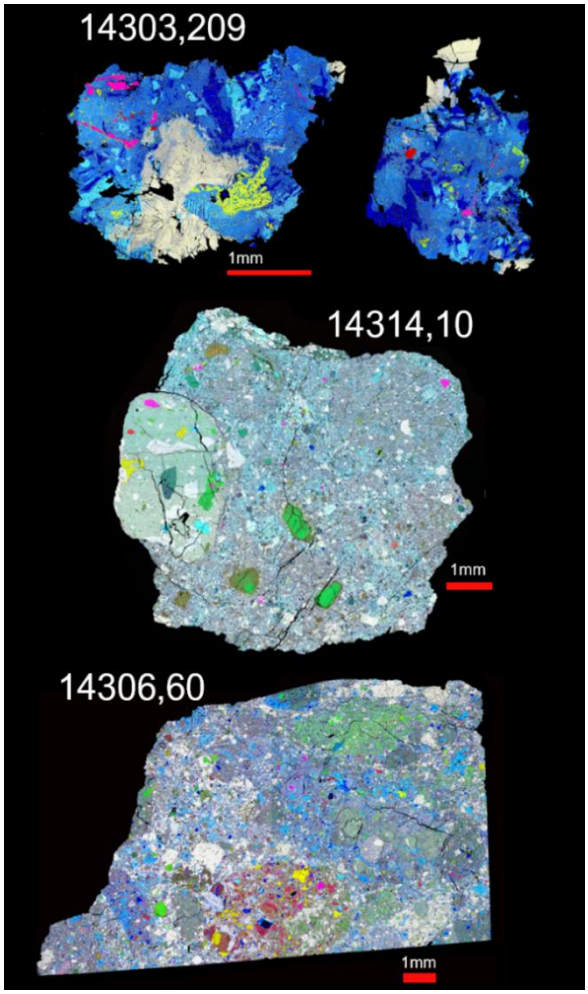

Figure 2: Seven element X-ray maps of the three Apollo 14 samples studied here. Al is white, Ca is yellow, Ti is pink, Si is blue, K is cyan, Fe is red, and Mg is green.

Sample 14314,10 is a crystalline matrix breccia [13] rich in plagioclase and a silica phase in the interstitial groundmass. Large, zoned olivine xenocrysts (ranging from ~.5mm to ~.8mm in length) in disequilibrium from the melt are present in this sample, with Mg# ranging from ~70 to 91, with Mg# increasing from rim to core. The largest phosphate crystals in this sample were identified within a large ~3mm impact melt breccia clast. The olivine grains in this clast range in Mg# ranging from 76 to 89, with lower Mg# corresponding to the olivine in the iron-rich zone in the clast **(Fig.3)**. This sample is also characterized by sodic

plagioclase, ranging from 0.57 to 3.15 weight percent Na_2O, with the highest sodium content present in the iron-rich region of the large impact melt breccia clast. Eleven phosphate crystals were identified in this sample. Only two of these phosphate crystals are apatite grains potentially suitable for SIMS analysis. As shown in **Fig.3a,** the largest apatite grains in this sample are inclusions in a REE enriched merrillite. In all three samples, REE enriched merrillite grains (ranging in size from ~5um to ~500um) are near plagioclase crystals.

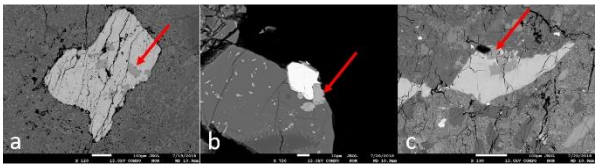

Figure 3: Back-scattered electron images of phosphate crystals for each sample. a: 14314,10 merillite grain with apatite inclusions; b: 14303,209 merillite grain with apatite rim; c: 14306,60 merrillite grain with apatite intergrowth**.** Red arrows indicate apatite.

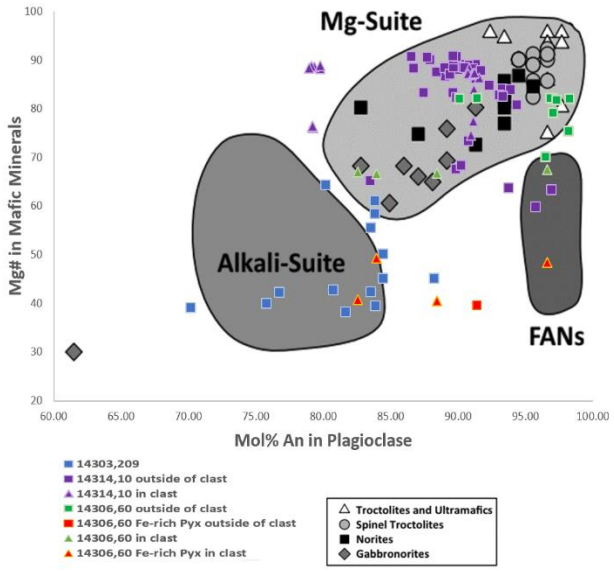

Figure 4: Mol% An in Plagioclase vs. Mg# in Mafic Minerals. Figure adapted from Shearer et al. (2016). Data gathered for each Apollo 14 sample within (triangles) and outside of clasts (squares).

Sample 14306,60 is a clast-rich crystalline matrix breccia [13], with large iron-rich, silica-rich and magnesian clasts. Phosphate crystals are most abundant in this sample, with 18 total identified phosphate crystals, including 13 apatite grains potentially suitable for SIMS analysis. Phosphate crystals in this sample were distinct from the other samples in that they are concentrated in a large, brecciated, phosphate rich, potentially gabbronorite clast. The plagioclase An content of this clast is similar to those in other lunar gabbronorites, 83 to 96 [16], however the Mg# in the iron rich pyroxenes is significantly lower from 38 to 49 **(Fig.4)** vs. lunar gabbronorites Mg# 64 to 78 [16]. However, the large number of phosphate grains in this clast indicate it may not be representative of its source lithology. This clast is also distinctive as it contains exsolved, Fe-rich pyroxene and zircon and silica intergrowths. One region of the clast is more plagioclase and Mg-pyroxene rich and contains fewer phosphate crystals relative to the clast as a whole **(Fig.1).**

Conclusions: All three Apollo samples studied are lunar breccias which originated from the Fra Mauro formation. Sample 14303,209 is granitic crystalline matrix breccia with sixteen phosphate crystals, found in K-feldspar and plagioclase rich regions. Sample 14314,10 is a crystalline matrix breccia with a large, distinct impact melt breccia clast, and eleven phosphate crystals were identified predominantly within the clast and near plagioclase crystals. Sample 14306,60 is a clast rich crystalline matrix breccia with multiple lithic clast. 18 phosphates were identified in this samples, with a concentration of apatite in a large iron rich potentially gabbronorite clast. Between all three samples, 45 phosphates were identified, 22 of which may be suitable for future SIMS analysis of H, OH, and Cl isotopes.

References:

[1] Smith et al. (1970) PLSC 1, 897-925. [2] Nekvasil H.D. et al. (2015) GRL 41, 10573-10579. [3] Robinson et al. (2016*) GCA* Pages 244-260. [4] Boyce et al. (2010) *Nature* 466, 466–469. [5] Saal et al. (2013) *Science* 1317-1320. [6] Hauri et al. (2015) *Earth Planet. Sci. Lett*. 252–264. [7] Barnes et al. (2014*) Earth Planet. Sci. Lett*. s 244-252. [8] McCubbin et al. (2010) *Proc. Natl Acad. Sci.* 11223–11228. [9] Kring et al. (2015) *Earth Planet. Sci. Lett*. 31-36. [10] Robinson et al. (2014) Nature Geoscience, 401–408. [11] Warren et al. (1983) *Earth Planet. Sci. Lett*. 64, 175-185. [12] Meyer et al. (1996) *Meteoritics & Planetary Science* 370-387 [13] Dence and Plant (1972) [14] Joy et.al (2012) *Science* [15] Joliff et al. (1993) *GCA* 4069-4094 [16] Shearer et al. (2016) *Mineralogy and Geochemistry* 365–518.

CHEMISTRY AND CRYSTALLOGRAPHY OF DIAGENETIC AND AUTHIGENIC POTASSIUM FELDSPAR: IMPLICATIONS FOR SEDIMENTARY PETROLOGY IN GALE CRATER, MARS. J. P. Ott[1], E. B. Rampe[2], R. V. Morris[2], and A. H. Treiman[3], [1]Department of Earth and Planetary Sciences, Harvard University, 20 Oxford St., Cambridge MA 02138 (jott@college.harvard.edu), [2]NASA Johnson Space Center, Houston TX, [3]Lunar and Planetary Institute, 3600 Bay Area Blvd., Houston TX.

Introduction: The Mars Science Laboratory Curiosity's Chemistry and Mineralogy (CheMin) instrument [1] performed X-ray diffraction (XRD) analysis of Gale Crater drill sample Windjana and found 21 wt.% potassium-rich feldspar and other phases shown in **Table 1** [2].

Felsic igneous rocks are rare on the Martian surface, and Windjana is the only potassic alkali-rich rock on Mars to be analyzed for its mineralogy [2,3,4]. The presence of potassic feldspar ($Or_{87\pm5}$, $Ab_{13\pm5}$) was made even more surprising by the highly disordered structural state of high sanidine suggested by unit-cell (UC) parameters derived from the XRD data [2]. WJ's sanidine has UC parameters **a** = 8.578 ± 0.006 Å, **b** = 13.016 ± 0.007 Å, **c** = 7.165 ± 0.007 Å, **β** = 116.0 ± 0.07°, matching those of nearly pure K-spar, suggesting little substitution by other elements (Na in particular). A comparison of the potassium content of the feldspar to the entire potassium budget of the sample revealed in bulk rock analysis indicates that practically all WJ's potassium comes from the K-spar [2], precluding abundances of other significant sources of potassium, such as illite. If there is more substitution for K^+ than estimated, then potassium sources such as illite could be present in greater abundance than initially interpreted [5].

Sanidine commonly forms during rapid cooling of potassium-bearing magmas; however, these sanidines are usually less potassic than Or_{87} [6]. Windjana's potassium-rich sanidine is more characteristic of metasomatic rocks [7]. The presence of olivine, plagioclase, pyrrhotite, and K-poor amorphous material suggests minimal effects of chemical weathering, and precludes in-situ diagenesis as a formation mechanism for the sanidine [2]. The coexistence of sanidine and pigeonite, which form in alkaline and subalkaline volcanic rocks respectively and rarely form together, suggests that the Windjana sandstone's sediment came from multiple sources [2]. The absence of common hydrothermal or metamorphic minerals like amphiboles, micas, chlorite, serpentines, and epidote could discourage a hydrothermal origin [2], but these phases could potentially be present as a source of potassium overshadowed by the K-spar [5].

Windjana's mineralogy, specifically its sanidine, is unfortunately not diagnostic of a specific formation environment, and this ambiguity could perhaps result from the lack of a comprehensive, precisely calibrated dataset on alkali feldspars: cell parameters, compositions, and formation conditions. Here, we begin to build that dataset. We hypothesize that the formation environment of sanidine influences its UC parameters such that those parameters and chemical compositions could be used to constrain the formation environment of Windjana's sanidine. To test this hypothesis, we assembled a large suite of terrestrial sanidine samples formed in igneous, hydrothermal, potassium metasomatic, and diagenetic conditions; we determine the UC parameters for each using powder x-ray diffraction and Rietveld refinement techniques, and determine their chemical compositions by electron microprobe.

Table 1. Mass proportions of phases in Windjana.

Mineral(s)	Mass % Total
Potassium Feldspar	21(3)
Augitic Pyroxene	20(3)
Magnetite	12(2)
Iron Oxide Spinel	12(2)
Pigeonite, Olivine, Plagioclase, Amorphous/Smectitic material	25(5)

Samples and Methods: A suite of 37 potassium feldspar-bearing rocks was assembled for analyses from a variety of locations and formation conditions, with an emphasis on basalts for their relevance to Mars. Sanidine was present and UC parameters were refined from 32 of these samples, 3 of which bear sanidine crystals thought to have formed igneously, 5 diagenetically, 14 by potassic metasomatism, and 5 by hydrothermal replacement of andesine. Literature data were compiled for 5 additional igneous sanidine samples [8,9].

Powder samples of grain size < 20 μm were produced for XRD analysis using a rocksaw and micronizing mill. These samples were then spiked with NIST standards 640e (Si metal) and 674b (Cr_2O_3 and ZnO) in approximately equal parts with an aggregate sample-to-standard ratio of 5:3. XRD data were obtained on a laboratory instrument (PANalytical X'Pert Pro MPD) at Johnson Space Center using: Co-Kα radiation; scans from 2-80º 2Θ; 0.02º step size; and 100 seconds per step. UC parameters and phase abundances were calculated via Rietveld refinements using JADE© software.

Sample offsets were adjusted within the refinements to achieve UC parameters for the standards that matched those reported by NIST.

Results: The distribution of UC parameters for the full range of alkali feldspars forms a quadrilateral with corners of high sanidine (K feldspar with full Al-Si disorder), maximum microcline (K feldspar with full Al-Si order), high albite (Na feldspar with full Al-Si disorder), and low albite (**Fig. 1, 2**). The distribution of samples on this quadrilateral shows the relationship between formation environment and UC parameters.

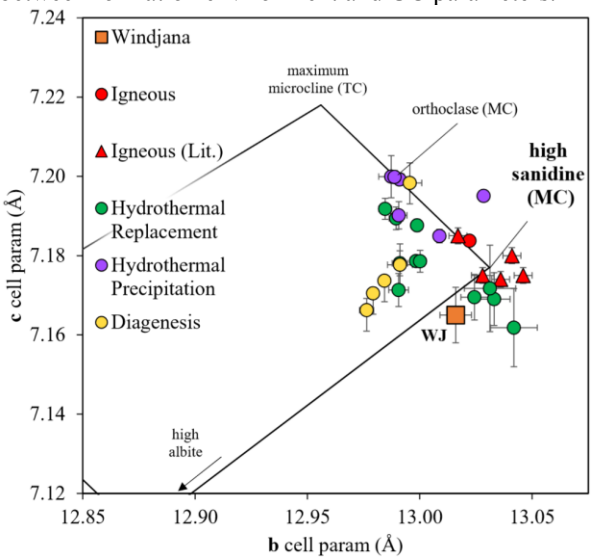

Figure 1: Sanidine **c** and **b** unit-cell dimensions, comparing terrestrial sanidine samples and their formation mechanisms to Windjana. Low and high albite endmembers occupy the lower left and lower right corners, respectively, of an alkali feldspar quadrilateral enlarged in this view. Error bars are calculated in JADE© during refinements.

In **Fig. 1**, we compare the **b** and **c** cell lengths of Windjana's sanidine to those from our sample suite, which are categorized by formation mechanism. Excluded from the plot are potassium feldspar samples that were analyzed but found to be in more ordered structural states. The samples reported on here are within the range of literature K-spar and plot near the high sanidine corner of the quadrilateral. Windjana plots slightly down the high sanidine-high albite series ($Or_{87\pm5}$).

Fig. 2 gives a similar distribution, looking at the **a** parameter instead of **c**. Most samples again plot near the high sanidine corner of the quadrilateral along with Windjana. The sodic endmembers of the quadrilateral lie just outside the plot area, ignored here to magnify the sanidine distribution.

Both distributions show some level of regionality according to formation mechanism, although noticeably less so in **Fig. 2**. This regionality is predicted by the hypothesis: if sanidine's formation environment controls its UC parameters, then one would expect samples that formed similarly to plot similarly on the quadrilateral, clustering together in distinct regions.

In **Fig. 1**, WJ plots just below the hydrothermal replacement region on the high sanidine-high albite series, while in **Fig. 2**, it plots again on the high sanidine-high albite series, between the igneous, hydrothermal replacement, and hydrothermal precipitation regions.

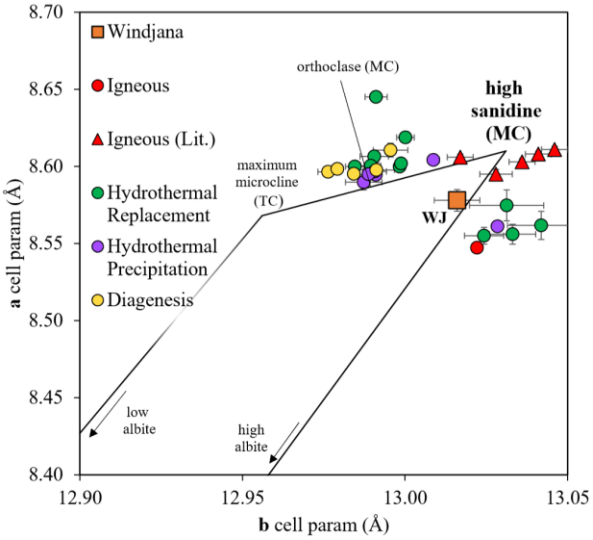

Figure 2: Sanidine **a** versus **b** unit cell dimensions.

Discussion: Initial interpretation of the distribution in **Fig.** 1 suggests the data can be divided into four distinguishable but overlapping regions: the igneous region centered around the high sanidine corner, the diagenesis region centered on the left-most edge of the distribution, the hydrothermal precipitation region in the upper left, and the hydrothermal replacement region scattered from the upper left to lower right bounds of the distribution. These regions can be further described by their centers (defined by an arithmetic mean) and standard deviations, shown in **Table 2**.

The hydrothermal replacement region of **Fig. 1** centers around **b** = 13.008 Å, **c** = 7.177 Å. In terms of standard deviations (σ) from the mean of hydrothermal sanidines' **b** and **c** lengths, Windjana plots 1.40 σ from the hydrothermal replacement region and between 3 and 6 σ from every other region (**Table 3**). In **Fig. 2**, Windjana is again closest to the hydrothermal replacement region (0.70 σ), although it nears the hydrothermal precipitation and igneous regions as well (1.44 and 1.72 σ). This is a result of Windjana plotting in the middle of these regions in the **a** versus **b** distribution. The overlapping nature of these regions must be inves-

tigated and measured to quantify the significance of WJ's proximity to each region.

Table 2. Means and standard deviations of observed formation-dependent UC regions.

Formation	Mean **a** (Å)	Mean **b** (Å)	Mean **c** (Å)
Igneous	8.595	13.032	7.179
Diagenesis	8.600	12.985	7.177
Hydrothermal Precipitation	8.590	12.999	7.195
Hydrothermal Replacement	8.593	13.008	7.177
	St. Dev. **a** (Å)	St. Dev. **b** (Å)	St. Dev. **c** (Å)
Igneous	0.022	0.010	0.004
Diagenesis	0.006	0.007	0.011
Hydrothermal Precipitation	0.014	0.015	0.006
Hydrothermal Replacement	0.027	0.020	0.009

Table 3. Comparison of WJ sanidine's unit-cell parameters' proximity to each formation-dependent UC region in **Fig. 1** and **Fig. 2**, or the **b-c** plane and **b-a** plane.

Formation	**Δa (σ)**	**Δb (σ)**	**Δc (σ)**	**Dist. in b-c plane**	**Dist. in b-a plane**
Igneous	0.78	1.53	3.13	3.49	1.72
Diagenesis	3.88	4.27	1.10	4.41	5.77
Hydrothermal Precipitation	0.89	1.13	5.30	5.42	1.44
Hydrothermal Replacement	0.55	0.43	1.33	1.40	0.70

To investigate overlap, we ask how likely it is that a sample's formation mechanism matches that of the nearest sanidine region. This probability can be estimated by compiling distances from each sample to each region's center in terms of the standard deviations in **Table 2**. Then, one can test an assumption that the closest region to a sample represents its formation mechanism. The percentage of samples for which this assumption is incorrect can be expressed as a measure of overlap.

According to this measure, hydrothermal replacement samples show 36% overlap with other regions, igneous samples show 33%, diagenetic samples show 20%, hydrothermal precipitate samples show 17%, and there is a net overlap of 29%. In the **b-a** plane, the overlap is much higher: 80% for diagenesis samples, 60% for hydrothermal precipitation, 45% for hydrothermal replacement, 33% for igneous, and 52% net overlap. These percentages should be expected to change as more samples are analyzed but give a good idea of the separation or lack thereof between different sanidine regions. As a result of this overlap, the formation environment of a sample cannot be determined with certainty by selecting the nearest region, especially if it plots between two strongly overlapping regions.

Conclusions: These data demonstrate that sanidine's formation environment does indeed affect its unit-cell parameters, at least to the extent that four distinguishable but overlapping regions can be seen in the **b** versus **c** parameter plot (**Fig. 1**). The hydrothermal replacement group is broad, possibly reflecting different progenitor compositions and/or fluid compositions. These regions are also present in the **b** versus **a** parameter plot, although they display significantly greater overlap and provide less insight in terms of the origin of Windjana's sanidine as WJ plots near the boundaries of overlapping regions.

The consistent proximity, in terms of σ, of Windjana's sanidine to the hydrothermal replacement region in both **Fig. 1** and **Fig. 2** is consistent with formation under hydrothermal replacement conditions, conceivably (given the setting of Windjana in an impact crater) impact-induced. However, the extent of overlap between the unit-cell parameters of igneous and hydrothermal sanidine, either precipitated from hydrothermal fluids or replacing preexisting minerals, does not preclude an igneous origin. The separation of Windjana from the diagenetic region sheds doubt on in-situ diagenesis as a formation mechanism for the Martian sanidine, but not to the point of exclusion.

If Windjana's sanidine were igneous, it would support models of it as a fluvial and eolian reworking of igneous progenitors from Gale Crater's northern rim [2]. If the sanidine is indeed a result of hydrothermal replacement of plagioclase progenitors, this would add to previous evidence of Martian hydrothermal processes (as would hydrothermal precipitation) and research on hydrothermal adularia as a process analogue for sanidine in Gale Crater [10,11,12].

References: [1] Blake D. F. et al. (2012) *Space Sci. Rev., 170*(1–4), 341–399. [2] Treiman A. H., et al. (2016) *J. Geophys. Res. Planets, 121*, 75–106. [3] Carter J. and F. Poulet (2013) *Nat. Geosci., 6*(12), 1008–1012. [4] Wray J. J. et al. (2013) *Nat. Geosci.,* 6(12), 1013–1017. [5] Le Deit L. et al. (2016) *J. G. R. P.*, 121(5):784-804. [6] Gupta A. K. (2015) 536 pp., Springer, New York, doi:10.1007/978-81-322-2083-1. [7] Le Bas M. J. (2008) *Can. Min.,* 46, 915–932. [8] Scambos T. A. et al. (1987) *Am. Min., 72*, 973-978. [9] Ferguson R. B. et al. (1991) *Can. Min., 29*, 543-552. [10] Morris R. V. et al. (2018) *LPSC49*, #2083. [11] Yen A. S. et al. (2017) *EPSL, 471*, 186-198. [12] Schwenzer S.P. et al. (2012) *Planet. Space Sci.* 70, 84-95.

PETROLOGIC ANALYSIS OF GREEN–BLACK IMPACT MELT BRECCIA WITH A HISTORY OF HYDROTHERMAL ALTERATION AT CHICXULUB. Stephen J. Slivicki[1,2], Martin Schmieder[1], and David A. Kring[1], [1]Lunar and Planetary Institute, 3600 Bay Area Blvd. Houston, TX 77058; [2]Department of Plant & Earth Science, University of Wisconsin River Falls, River Falls, WI 54022 (stephen.slivicki@my.uwrf.edu).

Introduction: With a diameter of ~180 km, the Chicxulub crater, linked to the end-Cretaceous mass extinction, is one of the largest impact craters on Earth [1,2]. The impact occurred ~66 Myr ago on a carbonate-evaporite platform on top of a complex crustal basement that today forms the northern Yucatán Peninsula [1]. Chicxulub is, therefore, among the geologically youngest and best-preserved large terrestrial impact structures, featuring an intact peak ring composed of shocked and uplifted basement rocks [1,2]. Impacts of this magnitude produce large volumes of impact melt [1–3]. At Chicxulub, impact melt is of andesitic composition and concentrated in a central melt pool inside the peak ring, as well as in the annular trough surrounding the peak ring [1,4–6]. The Chicxulub crater hosted an extensive, long-lived hydrothermal system after the impact [3,7,8] with an estimated lifetime of ~1.5 to 2.3 Myr [3]. Evidence for hydrothermal activity at Chicxulub is found in drill cores into the crater, such as Yucatán-6 (Y-6) and Yaxcopoil-1 (Yax-1), at radial distances of ~50 km and ~60 km from the crater center, respectively [1,2]. More recently, on Expedition 364, the International Ocean Discovery Program (IODP) and International Continental Scientific Drilling Program (ICDP) drilled into the northwestern Chicxulub peak ring at site M0077A, which is located ~45 km from the center of the structure [2]. Similar to rocks recovered from the Y-6 and Yax-1 cores, impactite and peak ring lithologies in core M0077A are hydrothermally altered [2, 8]. Of particular interest is a zone of black–green impact melt breccia between 1250 and 1316 meters below seafloor (mbsf) that lies underneath an upward-fining (reworked) suevitic breccia unit and above the shocked and uplifted crystalline (predominantly granitic) basement [2].

A puzzling aspect of the black–green melt breccia interval is the dichotomy between two distinct domains within the altered melt breccia (**Fig. 1**). The goal of this petrologic study is to resolve whether these two domains represent (1) intermingled types of now altered impact melt of different composition, (2) crystallized black impact melt juxtaposed with a domain of extensive hydrothermal alteration, or possibly a combination thereof. Petrologic results are compared with previous results for impact melt lithologies from other regions within the Chicxulub impact crater and its target rock, as well as altered lithologies from other terrestrial impact sites.

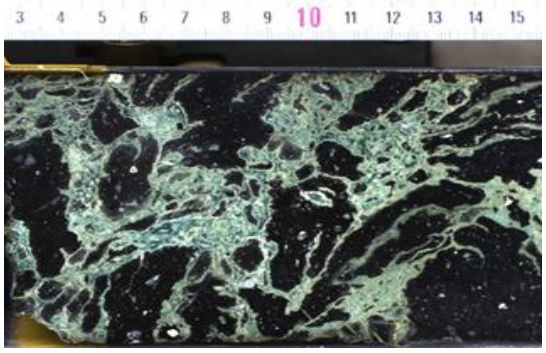

Fig. 1: Core segment 88–4 from IODP–ICDP Expedition 364 that displays both green and black domains of a hydrothermally altered impact melt breccia. Scale is in cm.

Samples and Analytical Methods: Sixcore and polished thin-section samples of the black–green melt breccia interval were examined in this study, including (1) 85-1-26-28 from a core depth of ~717 mbsf; (2) 88-3-48.5-50 from a depth of ~725 mbsf; (3) 89-3-13.5-15 from a depth of ~728 mbsf; (4) 90-3-70.5-72 from a depth of ~732 mbsf; (5) 89-3-39-43 from a depth of 729 mbsf; and (6) 92-2-91.5-93 from a depth of 737 mbsf. Samples (1) through (4) are representative of the 'black' melt domain, which locally grades into brownish and gray varieties, while samples (5) and (6) are representative of the green domain and the boundary between the two domains (**Fig. 1**). Thin sections were petrographically and geochemically examined using a Leica optical microscope at the Lunar Planetary Institute, and analyzed using a JEOL 5910 LV scanning electron microscope (SEM) and a CAMECA SX 100 electron microprobe (15 kV; 10/20 nA; 1–10 µm beam spot size) at the NASA Johnson Space Center.

Petrography and Geochemistry: The bulk of the black impact melt domain is a dark crystalline impact melt breccia that appears aphanitic in core sample, with brighter clasts up to several cm in size. When examined in thin section, the melt breccia groundmass contains ~65% feldspar (typical crystal sizes ≤10 µm), ~30% pyroxene (crystal sizes ≤8 µm), and microscopic opaque minerals. Groundmass feldspar has a wide compositional range of $An_{0–50}Ab_{1–70}Or_{3-99}$ (n=32). All pyroxene crystals analyzed are augite, $Wo_{38–50}$ $En_{22–46}Fs_{28–11}$ (n=60; FeO/MnO [wt%]=18–54; **Fig. 2**). Compared to samples (1) and (4), the melt groundmass in samples (2) and (3) is relatively poor in (and locally virtually devoid of) pyroxene and almost entirely

consists of feldspar; in those samples, pyroxene is mainly found in reaction rims (coronas) surrounding partially melt-entrained siliceous clasts (**Fig. 3a**). Corona pyroxene has slightly larger crystal sizes (up to ~10 μm) than groundmass pyroxene.

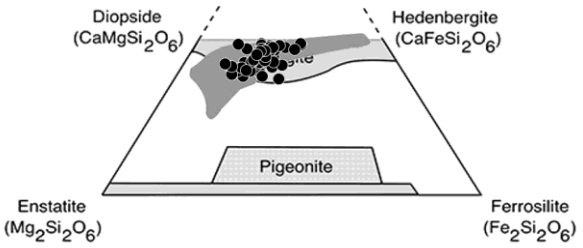

Fig. 2: Pyroxene quadrilateral showing composition of melt groundmass pyroxene (augite) in the black–green melt breccia interval, core M0077A (black circles, all samples), and results from cores Yax-1 and Y-6 [6,7,9] (gray field).

The black melt domain contains abundant mineral and rock clasts, most of which are siliceous in nature, i.e., quartz and/or granitoid clasts, while carbonate-bearing clasts are rare. Clast roundness is variable. Many siliceous clasts exhibit shock textures including multiple sets of planar deformation features (PDFs) in quartz, ballen quartz, and toasted (inclusion-rich) quartz [10]. Vesicles are abundant in the black melt domain, and commonly contain fillings of mafic sheet silicate, locally secondary K-feldspar (adularia), hydrothermal pyrite and magnetite and, in a few cases, hematite and barite. Many of the vesicles also have a hydrothermal phase of sparry calcite that entirely fills the rest of the void not occupied by sheet silicates. Scanning electron microscope analysis reveals an increasingly potassic composition of the feldspar around vesicles and cracks, especially in sample (1).

Samples (5) and (6) exhibit two distinct lithologic domains: first, a black domain, similar to the black melt breccia described above; and second, a 'green' alteration domain that consists of ~60% sheet silicate forming the bulk mass of the domain, ~25% interstitial calcite, ≤15% garnet, and minor opaque minerals. Scanning electron microscopy and electron microprobe analyses indicate the sheet silicate phase has a fibrous to flaky microtexture (**Fig. 3b**) and is rich in Mg, Fe, Al, and Ca, suggesting the sheet silicate is most likely the smectite-group clay mineral saponite (**Fig. 4**, [7,11, 12]). Hydrothermal garnet occurs in the form of euhedral, yellowish-translucent crystals, with andradite cores ($Gro_{12–28}And_{71–82}$) that have up to ~12 wt% TiO_2 and grossular rims ($Gro_{74–94}And_{26–5}$). This mineral is a pervasive phase within the green domain, and is found throughout the sheet silicate matrix. Garnet crystals seem to line the interface while keeping a roughly uniform distance from the black impact melt domain in the samples examined. The green domain is notably poorer in clasts than the black melt domain, and like the black domain contains a few clasts of locally microcrystalline-spherulitic silica. Moreover, one angular limestone clast was encountered. The boundary between the black and green domain appears to be a relatively sharp contact rather than a gradational one.

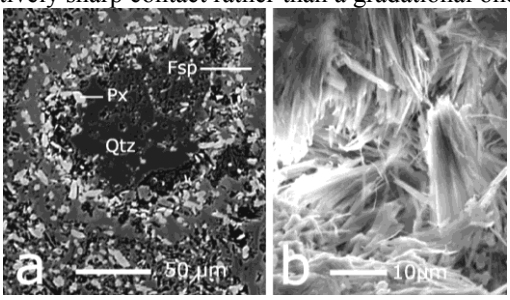

Fig. 3: Scanning electron images of green-black melt breccia domain. **a:** Pyroxene (Px) corona around a quartz grain (Qtz), with additional feldspar (Fsp) surrounding the corona, sample (6); backscattered electron image; **b:** Fibrous–flaky saponite in green breccia domain, sample (5); secondary electron image.

Discussion and Conclusions: The impact melt lithologies on top of the Chicxulub peak ring record a complex history of hydrothermal alteration [8]. In the black crystalline impact melt domain, pervasive hydrothermal alteration is evidenced by K-metasomatism along cracks and vesicles [8], the latter of which are commonly filled with secondary clay minerals and sparry calcite.

The composition of groundmass pyroxene in the black impact melt seems to be homogeneous across samples from core M0077A, and is similar to that of pyroxene found in impact melt-bearing lithologies from other sites at Chicxulub, such as the Y-6 and Yax-1 cores that sampled impactites in the annular trough surrounding the peak ring [6,7,9] (**Fig. 2**). Likewise, feldspar compositions are similar across the different cores [7]. The compositional similarity between pyroxene and feldspar in drill cores Y-6, Yax-1, and M0077A suggests that the Chicxulub impact melt was relatively homogenous across different impact crater domains, while local cooling rates and the amount of hydrothermal alteration those domains experienced may have been variable.

In contrast to the black melt domain, the green domain seems to almost entirely consist of secondary minerals that formed in a proposed crystallization sequence garnet – smectite (saponite) – sparry calcite, from high to low post-shock temperature [8]. While hydrothermal garnet is quite rare in other Chicxulub core samples [13,14], it appears to be a rock-forming mineral in green-altered zones within core M0077A, particularly in samples (5) and (6). The presence of garnet suggests minimum temperatures of ~280 to

300°C in the crater-hosted hydrothermal system [8,13–15].

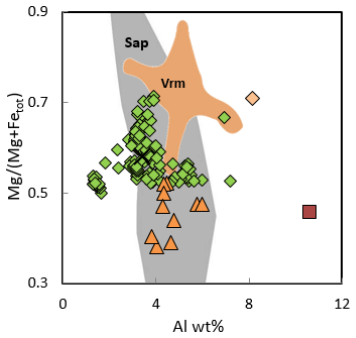

Fig. 4: Composition of mafic sheet silicates in black-green melt breccia domain (green diamonds), indicating saponitic compositions (Sap; gray field). Smectite-altered impact glass in the overlying suevite unit (orange triangles) seems to have a similar composition. Vermiculite (Vrm; tan field and diamond) and montmorillonite (red square) are shown for comparison. Diagram modified after [7]; mineral compositions from [11,12].

Due to the penetrative hydrothermal alteration, the source 'protolith' of the green alteration domain is difficult to reconstruct. However, looking at the macroscale features that are apparent in the core, it would seem that much of the green domain has a pseudofluidal texture that is also seen on a smaller scale in thin section. This suggests a number of possible formation mechanisms for the green domain. First, it may represent the alteration products of a melt or glass phase that was once intermingled with the black crystalline impact melt, but is otherwise not preserved in the samples analyzed. Saponite alteration has been reported from several terrestrial impact sites, where it replaces mafic minerals such as olivine and/or pyroxene [16,17], or mafic (basaltic) glass [18]. Mafic lithologies are, however, relatively rare inside the Chicxulub crater, and dolerite recognized in core M0077A, both as clasts in suevitic breccia and dikes within the peak ring [19], is typically shocked and hydrothermally altered but unmelted. Possible zones of near-glassy schlieren within the black melt, perhaps with a geochemical composition slightly different from the latter, may have been preferentially susceptible to hydrothermal alteration. Moreover, because of the dominance of saponite and a relatively low amount of calcite, a small number of clasts, and the lack of typical liquid silicate–carbonate immiscibility microtextures (e.g., [20]), an origin of the green domain as a zone of (altered) carbonate impact melt seems unlikely.

An alternative hypothesis and perhaps the more likely scenario is that the green domain represents a purely hydrothermal filling of large, elongated vesicles in the black impact melt, and/or open fractures between clasts of the black melt rock, similar to a model presented for garnet-bearing saponite domains in the Yax-1 drill core [14]. This process may have occurred after initial cooling of the melt, when the newly crystallized melt body experienced auto-brecciation and became permeable, which then allowed hot fluids, presumably seawater and/or saline brines, to circulate through open fractures [14]. Hydrothermal saponite formation is thought to occur at hydrothermal temperatures around ~100–150°C [21]. Magnesium, Fe, and Ca in the saponite may have been sourced from the overlying suevite unit that contains abundant fragments of target rock limestone and dolomite [1,2]; the survival of pyroxene in the black impact melt domain adjacent to the green alteration domain suggests the black melt was probably not the primary source for the saponite-precipitating fluids [14]. We, moreover, note a distinct compositional similarity between the green saponite alteration domain in the black-green melt breccia and smectite-altered impact glass in the overlying suevite body (**Fig. 4**). This suggests the enhanced flow of Fe-Mg-Al-Ca-rich fluids across different permeable domains of the Chicxulub peak ring and its overlying impactites, and possibly some vertical exchange of those fluids.

Penetrative, and locally rock-forming, smectite (saponite) alteration in the Chicxulub impactites underlines that post-impact hydrothermal clay-alteration domains are a frequent occurrence at larger impact sites [16]. Due to the long lifetime of hydrothermal systems in large impact craters, the high surface-to-volume ratio of clay mineral domains, and their potential significance in prebiotic biology, such domains may have provided a safe harbor for the origin and evolution of microbial life [22].

References: [1] D. A. Kring (2005) *Chemie d. Erde, 65,* 1–46. [2] Morgan J.V. et al. (2016) *Science, Vol 354,* 878–872. [3] Abramov O. and Kring D. A. (2007) *MAPS, 42,* 93-112. [4] Sharpton V. L. et al, (1996) *GSA Spec. Pap., 307,* 55–74. [5] Schuraytz et al. (1994), *Geology, 22,* 868-872. [6] Kring D. A. and Boynton W. V. (1992) *Nature, 358,* 141–144. [7] Zürcher L. and Kring D. A. (2004) *MAPS, 39,* 1199–1221. [8] Kring D.A. (2017) *LPS XLVIII,* abstr. #1212. [9] Ames et al.(2004), *MAPS, 39,* 1145–1167. [10] French B. M. (1998) *Traces of Catastrophe, LPI Contrib. 954,* 120 pp. [11] Handbook of Mineralogy, online. [12] Treiman A. H. et al. (2014) *Amer. Mineralogist, 99,* 2234–2250. [13] Newsom, H. E. et al. (2010) *LPS XLI,* abstr. #1751. [14] Nelson M. J. et al. (2012) *GCA,86*1–20. [15] McCarville P. and Crossey L. J. (1996) *GSA Spec. Pap., 302,* 347–376. [16] Allen et al. (1982) *JGR,* 87, 10,083-10,101. [17] Hart et al. (2002) *EPSL,* 198, 49–62. [18] Hagerty J. J. and Newsom H. E. (2003) *MAPS, 38,* 365–381. [19] Schmieder M. et al. (2017) *LPS XLVIII,* #1235. [20] Osinski G. R. and Spray, J. G. (2001) *EPSL, 194,* 17–29. [21] Osinski G. R. (2005) *Geofluids, 5,* 202–220. [22] Kring D.A. (2000), *GSA Today, 10,* 1–7.

WATER CONTENT AND MINERAL ABUNDANCES AT GALE CRATER, MARS AS INFERRED FROM OMEGA AND CRISM OBSERVATIONS. F. Stachurski[1] and Y. Liu[2], [1]University of Glasgow, Scotland, UK, [2]Lunar and Planetary Institute, Houston ,TX, USA, rico.stachurski@hotmail.com.

Introduction: Gale crater is a 154 km diameter impact crater on Mars, where the MSL Curiosity rover has been exploring since 2012. Previous studies using orbital remote sensing data have revealed the presence of hydrated minerals such as hydrated sulfates and clays, which record aqueous alteration in the crater [1]. Curiosity's *in situ* analyses of rocks and soils have turned up abundant evidence for ancient water-rich environments in Gale crater, which has raised the possibility of Mars' past habitability [2]. In this study, we quantitatively analyze the hydration state (i.e., water content) and mineral abundances at Gale Crater using hyperspectral visible/near-infrared (VNIR) data from the Observatoire pour la Minéralogie, l'Eau, les Glaces et l'Activité (OMEGA) instrument onboard Mars Express and from the Compact Reconnaissance Imaging Spectrometer for Mars (CRISM) instrument onboard Mars Reconnaissance Orbiter (MRO). Water contents derived from orbital data can be directly compared to results from *in situ* heating experiments of regolith materials by Curiosity, which can in turn validate our approach. Also, the derived mineral abundances help test and constrain the formation mechanisms of hydrated minerals at Gale crater at a regional scale, which will also help route planning to geologically-interesting sites for Curiosity, and for comparison to rover-based results.

Methods: *Data Sets.* The primary data sets used in this study are OMEGA and CRISM hyperspectral data. OMEGA consists of a visible near-infrared spectrometer, sensitive between 0.35 and 1.05 µm, a C spectrometer from 0.97 to 2.73 µm, and an L spectrometer from 2.55 to 5.1 µm [3]. OMEGA has varied spatial resolution from 0.3 to 3 km. CRISM has 544 channels covering 0.36–3.92 µm and has a spatial resolution of either full spatial resolution (FRT; 18 m/pixel) or 2 times spatially binned (HRL/HRS; 36 m/pixel) in targeted mode [4].

Atmospheric and Thermal Correction. We use the Discrete Ordinates Radiative Transfer (DISORT) program to simulate the I/F value observed by OMEGA and CRISM. DISORT simulations explicitly account for the atmospheric contributions caused by the absorption, scattering, and emission of gas and aerosols. A lookup table approach was used to retrieve the single-scattering albedos from the observed I/F. Specifically for OMEGA data, we also simulate thermal emission contribution, which allows us to perform thermal correction on I/F at > 3 µm wavelength region.

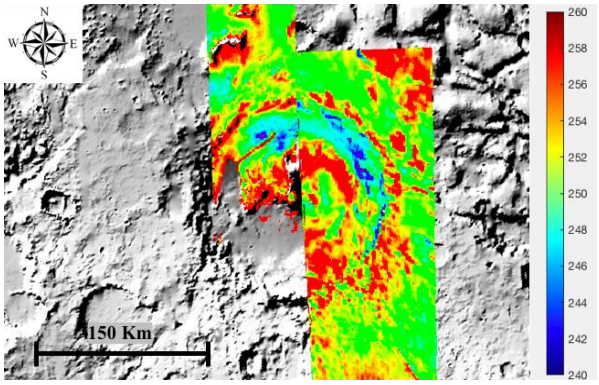

Figure 1: Temperature map over Gale crater using swath 2363_4 (left, local true solar time: 12:07:48, Ls = 324.43°) and 0436_2 (right, local true solar time 09:29:57, Ls = 37.87°).

Surface kinetic temperatures over Gale were derived at the time of each OMEGA observation using the method of [5]. First, the atmospheric corrected OMEGA reflectance at ~2.5 µm region was used to estimate the reflectance at 5 µm, based on the linear relationship linking 2.5 and 5 µm reflectance [5]. The OMEGA I/F data at 5 µm contains both reflectance and thermal emission. Thermal emission was calculated using Kirchoff's law (i.e. T = 1 – R, where T is thermal emission as a function of temperature and R is reflectance). This allows us to compute for temperatures by fitting a blackbody curve over the thermally emitted spectra. The computed temperatures are then used to correct for thermal emission contribution to the spectral data across 3-5 µm region.

Water Abundance Estimation. To quantify the water abundances at Gale crater, we used the method of [5]. The method consists of using the single scatter albedo to extract effective single-particle absorption-thickness (ESPAT). The single scatter albedos were extracted from the reflectance data using Hapke's simplified relationship for the bidirectional reflectance function (BDRF) [6]. The ESPAT parameter at a given wavelength is expressed as follows [6]:

$$ESPAT = \frac{1 - \omega_\lambda}{\omega_\lambda} \quad (1)$$

Where ω_λ is the single-scatter albedo. The ESPAT value at 2.9 µm was then used in the linear relationship relating wt.% H_2O to the ESPAT value [7]:

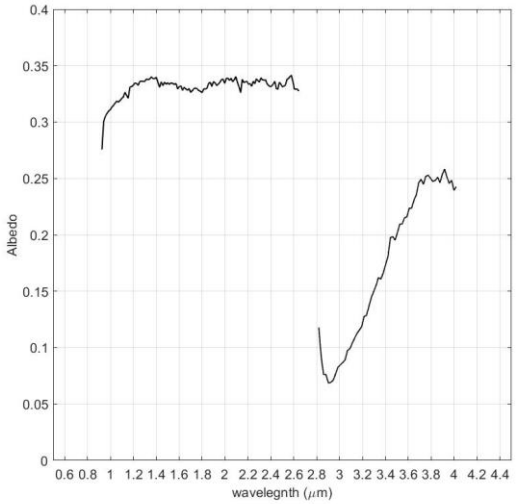

Figure 2: Atmospheric and thermally corrected reflectance from OMEGA data. The spectrum was take over Gale crater from observation 2363_4.

$$wt.\%\, H_2O = 4.0064 * ESPAT(2.9\ \mu m) \quad (2)$$

Spectral Unmixing of CRISM SSA. The CRISM atmospherically corrected single scattering albedo (SSA) data was run in a spectral unmixing software code, which models the single pixel spectra using non-negative least squares (NNLS) method [8]. The model reproduces the shape and depth of absorption bands, the continuum and the absolute value of the reflectance. The software runs a model with a set of endmembers and grain sizes carefully chosen and excludes unwanted endmembers and grain sizes. The SSA albedo spectrum of different endmembers can be added linearly, which allows a linear least square fit of the data using simulated single scattering albedos, producing the best fit with the lowest RMS error between the data and the model fit, yielding abundance and grain sizes of the minerals over each spectrum.

Results and Discussion: *Water Abundance at Gale Crater.* Figure 1 shows the map mosaic of temperature over Gale crater (from the two swaths of OMEGA data), which allows us to perform pixel by pixel thermal correction over the OMEGA long wavelength region and thus derive water abundance based on the 3 μm absorption band. Figure 2 shows the retrieved albedo spectrum, with both atmospheric and thermal emission contribution removed – the ~3 μm water absorption band is obvious. The 3 μm water absorption band allows estimate of water content through ESPAT parameter.

Figure 3 shows a map over Gale crater of the regolith's water contents, derived from the OMEGA images using the ESPAT coefficient. Regolith on the plains north of Gale crater contain ~2-3 wt% H_2O.

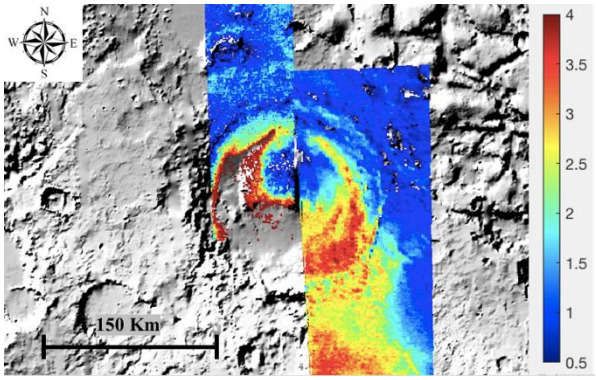

Figure 3: Water percentage per mass distribution covering Gale crater as inferred from the 2.9 μm value of ESPAT parameter.

The range is less than the estimate of [9], in which they show the water abundance to be ~4.7 wt% H_2O, although the two studies both follow the method of [7]. The possible reason for this discrepancy is that, they did not account for the influence of water ice clouds whereas our DISORT modeling approach has corrected the contributions from atmospheric water ice to the spectral radiance. The *in situ* measurement of the Rocknest sand shadow material by SAM instrument on Curiosity yield bulk water content values between 1.5 and 3 wt% H_2O [10], which is consistent with our estimates with orbital data. Our results also show that the equatorial region of Mars has water content of 2-3 wt% H_2O percent without much variations, and water content slightly increase with increase of the latitude.

Mineral Abundances Derived from Spectral Unmixing of CRISM Data. Spectral unmixing modeling was performed over phyllosilicate and sulfate rich-units using CRISM single scattering albedo spectra, respectively, to extract the abundances and grain sizes of both hydrous and anhydrous phases. The results are shown in Figure 4. The derived abundance of phyllosilicate (i.e., nontronite) is low (~6%) and is around our detection limit (~5%), mostly due to its generally weaker spectral signature and the presence of dust at Gale crater region. Curiosity is exploring the hematite unit at Vera Rubin Ridge, and will arrive at the phyllosilicate unit in the following months, which provides an opportunity to cross compare the results from the orbital and *in situ* observations over this unit and to see whether or not the *in situ* exploration reveal more abundance of clay minerals. Above the phyllosilicate unit are the hydrated sulfates layer. Our spectral unmixing analysis shows that there is 16% hydrate sulfates in abundance (Figure 4).

To investigate spatial distribution of the secondary mineral abundances, we applied our spectral unmixing model to CRISM image HRL0000BABA to generate the mineral abundance maps.

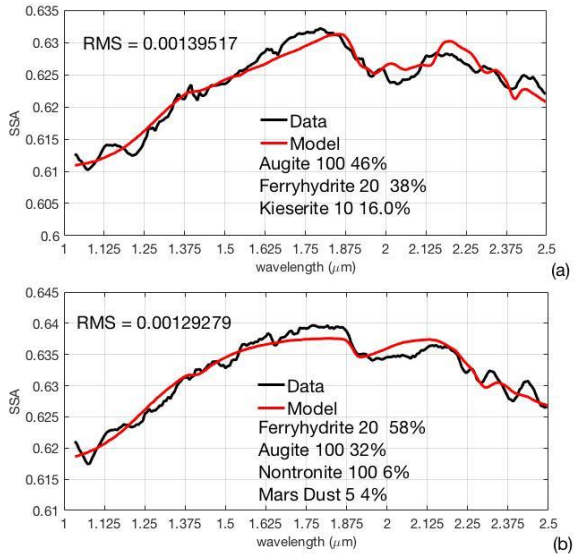

Figure 4: Derived mineral abundances and grain size. The numbers after mineral name are the grain size in micrometer, and the numbers of percentage indicate the mineral abundance in volume. (a) Hydrated sulfate-rich unit. (b) Phyllosilicate-rich unit.

Figure 5a shows the secondary phases mapped over Mount Sharp [11], and Figure 5b shows the result of the spatial spectral unmixing analysis over the selected region enclosed in the white box in Figure 5a. From Figure 5b it is possible to resolve the hematite, phyllosilicate and hydrated sulfate unit, and these units are consistent with spatial distribution with CRISM parameter map shown in Figure 5a. The spectral unmixing of CRISM image cube over Gale indicate that there are 39% hematite, 4% phyllosilicates, and 16% hydrated sulfates. These abundances show how the hydrated minerals are present, even if in small quantitates, over this region of Mount Sharp. *In situ* analysis of Curiosity will shine more light on this when it will start to traverse the phyllosilicate and hydrated sulfate unit, allowing direct comparison with our results.

Conclusions and Future Work: In this study, we estimated the water abundance over Gale crater based on the 3 µm water absorption feature using OMEGA data. Our results indicate that the water content over Gale is around 2-3%, which is consistent with the *in situ* measurement of the Rocknest sand shadow material by SAM instrument on Curiosity. The spectral unmixing of CRISM data over Gale crater was perform to derive mineral abundances in this region. Our results indicate that the area has relatively low abundance of phyllosilicate and relatively high abundance of hydrated sulfates. The future in situ analysis by Curiosity will provide ground truth for our modeling approach. Future work will consist in processing more orbital data from OMEGA, thus having a better coverage in water wt.% of Gale, especially in the west region, as well as performing spectral unmixing analysis of CRISM data covering other areas of Gale crater to provide a more complete mineral abundance map over Gale crater.

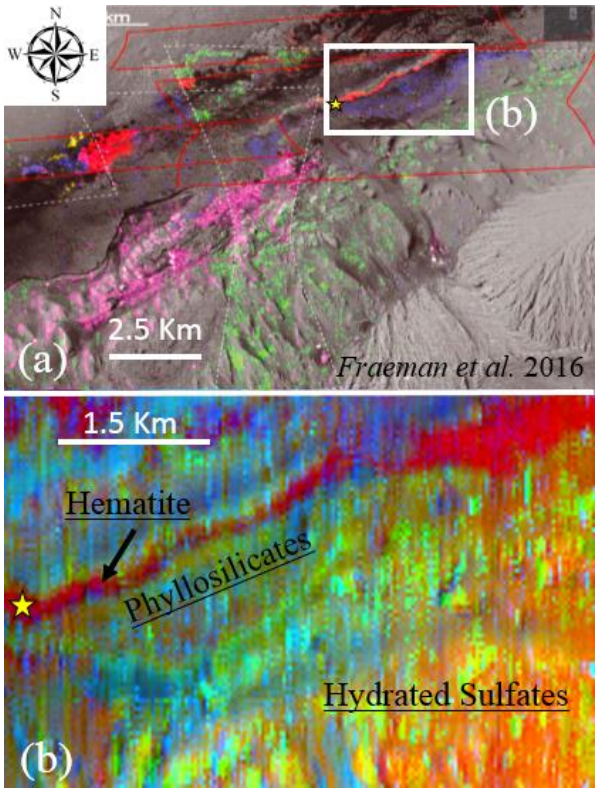

Figure 5:(a) Secondary phases mapped in Mount Sharp using CRISM ATO parameter map [10]. Red: hematite; Green: hydrated sulfates; Blue: phyllosilicates. (b) The RGB map of the spectrally unmixed data covering the same region showed in the white box in (a). The star shows the current position of Curiosity.

References: . [1] Milliken et al., (2010), *Geophysical Research Letters,* 37, L04201. [2] Grotzinger et al., (2015), *AAAS,* 350, 37-49. [3] Bibring et al. (2014) *Mars express: the scientific payload,*1240,37-49. [4] Murchie et al. (2014) *JGR, 112.* . [5] Milliken et al., (2007), *JGR, 112,* E08S07. [6] Hapke B., (1993), *Theory of Reflectance and Emittance Spectroscopy,* Cambridge University Press, New York, 455 pp. [7] Milliken and Mustard, (2007), *ICARUS, 189*, 574-588. [8] Ramsey, M. S., and P. R. Christensen (1998), J. Geophys. Res., 103(B1), 577–596.[9] Audouard et al. (2014) *JGR, 119,* 1969–1989. [10] L.A.Leshin et al., (2013) *Science(AAAS),*341, 1238937-(1-9). .[11] A.A.Fraeman (2016), *Science(AAAS)*, 121(9), 1713-1736

THE ORIENTATION OF THE BLADED TERRAIN FEATURE IN TARTURUS DORSA, PLUTO AND POSSIBLE REORIENTATION OF PLUTO N. L. Wagner[1], J. P. Kay[2], and P. M. Schenk[2], [1]Colorado School of Mines, 1500 Illinois St, Golden, CO, 80401(nlwagner@mines.edu), [2]Lunar and Planetary Institute, 3600 Bay Area Blvd, Houston, TX, 77058

Introduction: During the New Horizons flyby of Pluto in 2015, numerous interesting and puzzling features were observed on the dwarf planet. One such feature called bladed terrain is located in the Tarturus Dorsa region of Pluto covering roughly 200,000 km^2. It extends from 10°S to 40°N in latitude and is considered an uplands area, with elevations around 3 to 4 kilometers above the mean elevation of Pluto [1]. With little to no cratering observed the age of this feature is believed to be on the order of tens of millions of years [2]. The bladed terrain sits on a plateau with a surface consisting of individual ridges, or blades, which are a few hundred meters in height and stretch anywhere from 2 to 14 kilometers in length [1]. Through spectroscopy it is likely that these blades are comprised of methane (CH4) ice, and it is argued that they are formed through sublimation in a nature similar to penitentes on Earth [2].

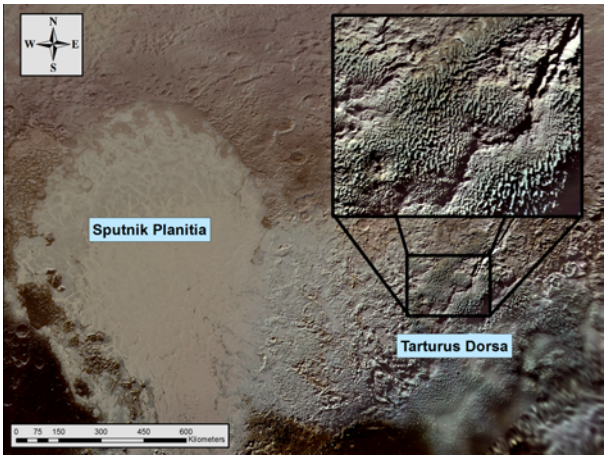

Figure 1: Cutout view of northern section of the bladed terrain with crater-like feature in bottom left of cutout. Sputnik Planitia is thought to be a deposit of nitrogen ice with an elevation a few kilometers lower than the surrounding uplands.

Penitentes form on Earth (figure 2) at high altitudes and low latitudes similar to where the bladed terrain occurs on Pluto. Some regions of the snow melt/sublimate faster than others, creating divots in the snow. These divots then melt faster due to sunlight reflecting off the sides, creating a positive feedback system. As the divot becomes deeper the sunlight reflects and bounces more off the side of the divot, eventually creating the penitentes we observe in mountain ranges such as the Andes [3]. On Earth penitentes only rise a few meters above the ground and have a seasonal life cycle. The transit of the sun greatly affects the orientation of penitentes causing them to orient along the path of the sun from east to west on Earth [3].

Penitentes on Pluto may form in a similar manner as they do on Earth and therefore form in a preferred orientation. Based on how penitentes form on Earth and Pluto's orbital parameters we expect them to form generally northeast/east to southwest/west [2]. We're looking for any deviation from this orientation which would suggest a reorientation event such as polar wander. Like other outer solar system icy bodies, such as Europa and Ganymede, Pluto is hypothesized to hold an internal ocean of water [4]. Any evidence that Pluto has become reoriented would help support this theory. With an internal ocean the icy outer shell is free to move based on deposition, removal, or movement of mass. Given the fact that the blades form in a preferred orientation any deviation from that would help provide insight into the degree to which Pluto may have been reoriented. There is additional evidence of reorientation from the large fractures around Sputnik Planitia that have been suggested to be caused from global stresses and possibly reorientation, but this work could place further constraints on the timing of that reorientation given the youngish age of the penitentes [4,5].

Figure 2: Penitentes found on Earth with an average height is around a meter or two. General orientation of penitentes in photo is roughly bottom left of figure to top right. Taken in the Andres, Chile. Photo courtesy of TripAdvisor.

In this study we mapped the orientation of the bladed terrain in order to determine if this is the preferred formation or if reorientation might have occurred. The average elevation, average longitude, average latitude, and length of each individual blade was also calculated using respective functions in ArcGIS in an attempt to determine if the blades indicated correlations between those parameters. If reorientation is possible, next steps will include using the Python program SatStressGUI to estimate the direction and magnitude of the reorientation. We also looked for any defining characteristics that may help determine how and why these features form.

Procedure: We used ArcMap 10.3.1 and a global basemap of Pluto with a cylindrical projection and a

300m/pixel resolution. Using ArcMaps the blades were traced as polylines along their highest extent using color, elevation, slope, and stereo data. The elevation data has a resolution of 315m/pixel with an orthographic projection. Sharp changes in the stereo data from light to dark were used to resolve a majority of the blades with color, and elevation was used to confine them to certain areas and elevations. Around the terminator in the Southeast region of the bladed terrain the elevation and slope data helped to resolve the blades.

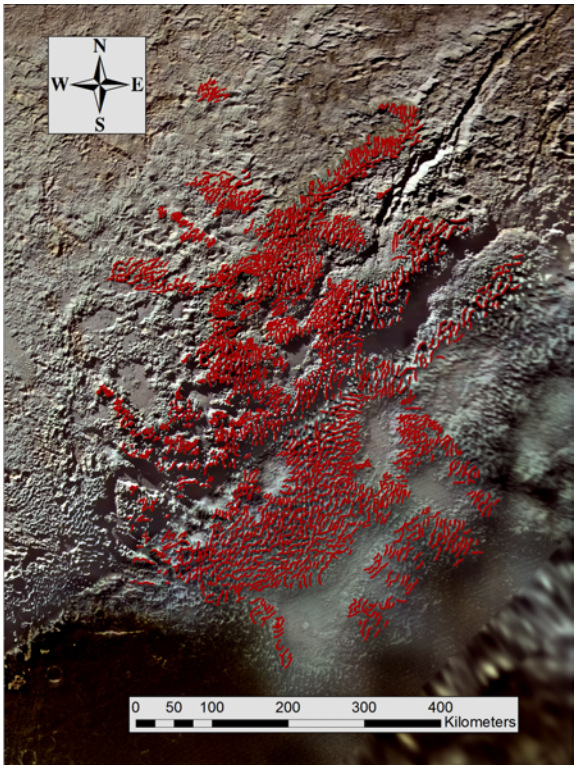

Figure 3: Total extent of the blades in Tarturus Dorsa. 2382 blades in total drawn in red.

Once the blades were mapped the length of each one was calculated using one of ArcMaps built in functions for finding the length of a polyline. The orientations were found by calculation through a Python function. Orientations from 0° to 360° were generated based on which direction the line started and ended. 180 was subtracted for each measurement that was over 180° to negate this preference for which direction the line was drawn. Using two more built in functions in ArcMaps, the X and Y coordinates of the midpoint of the blade were calculated. The value computed is not in degrees but in meters, akin to UTM on Earth. Finally the elevation was found using another ArcMaps function that calculates the Z coordinate of the midpoint of the line based on a base elevation map. To make the elevation profiles, a line was first drawn out as a polyline. The ArcMaps function *densify* was then used to create vertices along that line with regular spacing. These vertices were then converted to points where the *add surface information* function was used to add elevation information to each point.

Results: In total we mapped 2382 individual blades (figure 3). The blades range in length from 2 to 20 kilometers with an average length of 8 kilometers. There was a general trend of northeast to southwest or around 35° to 45° from North taken from figure 4. A majority of the blades are within 15 degrees of this preferred orientation. They range in latitude from 10°S to 40°N and in longitude from 215° to 240°. There appears to be no indication of multiple sequences of these features and detailed analysis does not show much, if any, degradation or variation in the morphology of these features.

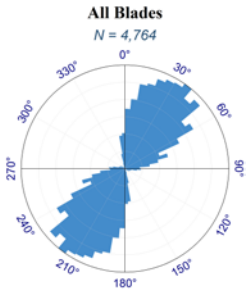

Figure 4: Rose diagram of all the blades, plotted with reverse azimuths to make it symmetrical. Binned at 5° with 0° as north.

Discussion: In determining the preferred orientation of the blades we looked at as many of the available characteristics as possible. Specifically, we looked at how the orientation of the blades changed as a function of latitude, longitude, elevation, and length. We also looked at how these other factors correlated with each other, outside of orientation, however no correlation was detected. We have an example below in figure 5 where we attempted to correlate the orientation with the blades latitude.

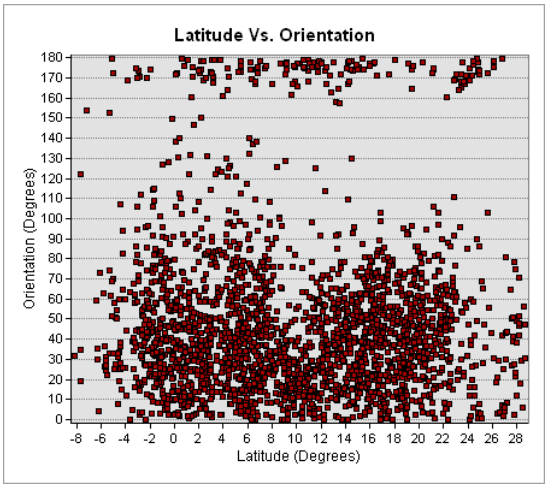

Figure 5: Orientation of the plots plotted as a function of latitude. Blades around 180° are in the same direction as those at 0° except taking magnitude into effect.

One important factor regarding penitente growth and orientation is the insolation angle of the sun which is directly affected by the latitude of the area in question. In figure 5, we plotted the orientation of each blade against its respective latitude. There does not seem to be a correlation between latitude and orientation.

We also looked at the morphological shape of the penitentes. Using elevation data, we found the shape of them to be almost symmetric across one wavelength, tending to lean towards the west slightly. Four elevation profiles were taken whose locations are shown in figure 6, and plotted in figure 7.

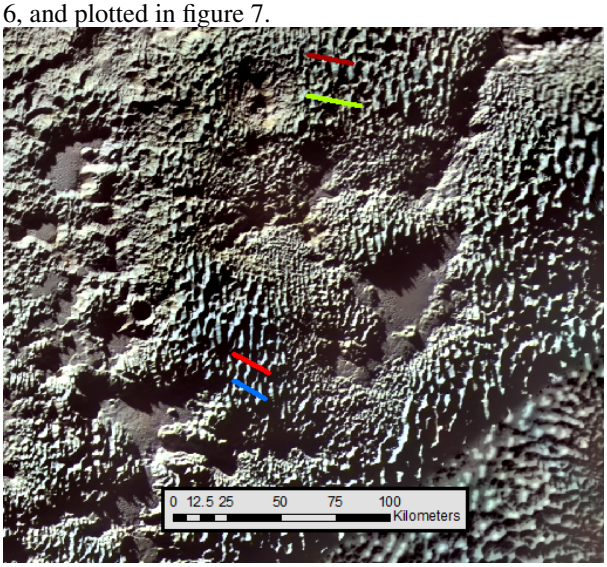

Figure 6: Location of the Profiles shown in figure 7

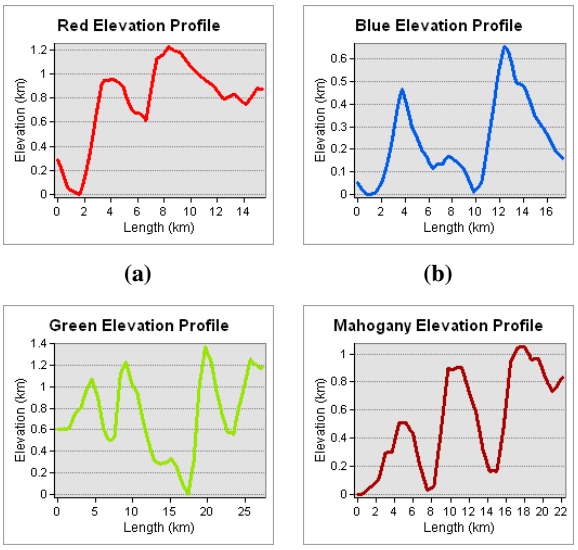

(a) **(b)**

(c) **(d)**

Figure 7: Elevation profiles of the blades.

We confirmed the average height of the blades to be around 400 to 500 meters. However, we noticed significant variance in the sizes of the blades, the smallest of them being about 100 meters in height to just over a kilometer. This could be due to the initial parabolic shape of the blades; as more sublimation occurs, the blades become distinct from each other and can be interpreted as separate blades. This variation could also arise from the elevation profiles being relatively near each other along the length of the blades. This causes the same blade showing up in both the red and blue profile and the green and mahogany profile but at different heights. More analysis should be conducted on the variation of the symmetries of the blades and if there is any correlation between elevation, length, location, or orientation.

Conclusion: We did not observe any noticeable change in the orientation of the penitentes with respect to any observational parameter. Therefore we think that it is unlikely that Pluto has reoriented significantly in the past tens of millions of years. We also did not find any correlations between elevation, orientation, and latitude that would lead us to suggest that reorientation occurred while these features were forming. Because of this result no further work on SatStress was conducted. This study does not preclude that Pluto reoriented, simply that it did not happen while these features were forming. Further work should include deeper analysis into the optimal formation periods of penitentes in Pluto's orbit and how the expected blade morphology changes over tens of millions of years.

References: [1] Jeffrey M. Moore, et al. Bladed Terrain on Pluto: Possible origins and evolution. *Icarus*, 300:129 – 144, 2018. ISSN 0019-1035. doi:https://doi.org/10.1016/j.icarus.2017.08.031. [2] John E. Moores, et al. Penitentes as the origin of the bladed terrain of Tartarus Dorsa on Pluto. *Nature*, 541:188, 2017. [3] L. Maclagan Cathles, et al. Intra-surface radiative transfer limits the geographic extent of snow penitents on horizontal snowfields. *Journal of Glaciology*, 60(219):147154, 2014. doi:10.3189/2014JoG13J124. [4] F. Nimmo, et al. Reorientation of Sputnik Planitia implies a subsurface ocean on Pluto. *Nature*, 540:94, 2016. [5] James T. Keane, et al. Reorientation and faulting of Pluto due to volatile loading within Sputnik Planitia. *Nature*, 540(7631):90–93, 2016. ISSN 1476-4687. doi:10.1038/nature20120.

ANOMALOUS RADAR PROPERTIES AT VENUS' MOUNTAINTOPS: REFINED SPATIAL RESOLUTION FROM STEREO ALTIMETERY. F. B. Wroblewski[1], A. H. Treiman[2], and S. S. Bhiravarasu[2], [1]Department of Environmental Geosciences, Northland College, 1411 Ellis Ave S, Ashland, WI 54806 (wroblf195@myemail.northland.edu), [2]Lunar and Planetary Institute, 3600 Bay Area Blvd, Houston, TX 77058.

Introduction: Radar properties of Venus' surface (emissivity, SAR backscatter) vary with elevation, and show strong transitions at a critical elevation of roughly ~5km. However, the characteristics of these transitions are different in the peripolar (Maxwell Montes) and near-equatorial (e.g., Ovda Regio) mountains. Causes of these transitions are not known, and could involve changes in mineralogy [1,2], or in roughness [3,2].

We studied Venus' radar properties on two contrasting mountain ranges: (1) Maxwell Montes (65.2°N 3.3°E), the highest mountain peak on Venus, with a SAR-bright "snowline" forming at the critical elevation; and (2) the Festoon Flow area (-5.9°N 95.6°E) of Ovda Regio, which hosts a SAR-dark transition alongside a lava flow unit.

In the absence of recent data, we used recorded data from the Magellan mission (1990-1994) to investigate these areas. The snowline feature of Maxwell Montes remains unique in comparison to other highlands, where elevations past the SAR-bright "snowline" gradually darken to intermediate values between the lowlands and the "snow" [Fig. 1]. The Festoon Flow contains flow features becoming SAR-dark by crossing the critical elevation, alongside a variety of sharp and gradational transitions within its margins [Fig. 1].

Using refined stereo DEMS [4], we associate changes in radar reflectance and emissivity to differences in surface properties. From these changes, we propose mechanisms causing these anomalies. In addition, new geological mapping of the Festoon Flow employs fractal analysis to derive host rock composition and to suggest new flow histories.

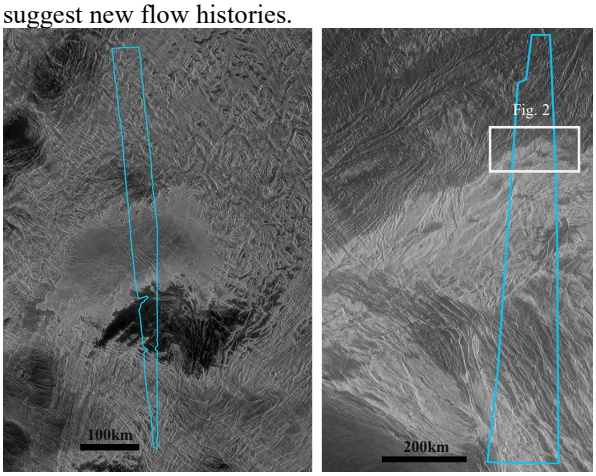

Figure 1: Left-look SAR Maps with Study Areas (blue boxes) of Ovda Regio (left) and Maxwell Montes (right). White box correlates to Fig. 2 extent. North is up.

Methods: Data used here are Magellan SAR backscatter, and emissivity, with high-spatial resolution DEM elevations from cycle-1—cycle-3 stereo [4]. We have utilized the Magellan SAR FMAP images at ~75m/pixel for generating backscatter maps and the USGS "ISIS" [5] for reprojecting them. For quantitative comparisons [6], we generated synthetic incidence angle images for both the study regions and then generated the true radar backscatter coefficient images using equation 4 of [7]. Stereo DEMs (~375 m/pixel) were used in place of Magellan altimetry (8x10 km/pixel) for greater spatial relation.

Within each mountaintop region, we selected study areas with continuous DEM swaths that were at least 10 km from DEM elevation discontinuities (stitching errors). Using ArcGIS 10.3.1, we selected polygonal areas in the swaths with consistent values of elevation and backscatter [Fig. 2], and calculated zonal mean values for each polygon.

The Festoon Flow on Ovda was mapped in detail onto left-look FMAP, emphasizing flow margins (internal and external) and orientations of festoon ripples. Flow margins, east- and west-facing, were traced by their high backscatter in left-look and right-look SAR images respectively. Elevation profiles across the flow were generated from the stereo DEM. Selected flow margins were analyzed for their fractal dimension [8].

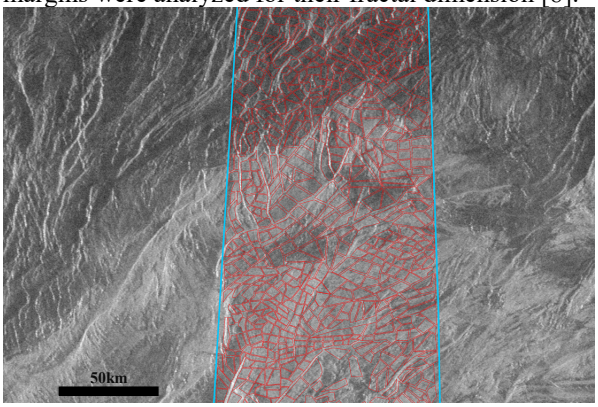

Figure 2: Polygonized Swath on Maxwell Montes. Blue lines are the study area, red lines represent polygons. North is up.

Maxwell Montes: Maxwell includes the highest elevations on the planet, so it has been of great interest for both tectonic origin and material properties. Maxwell is notable in having a 'snow line' of radar properties – an elevation at which SAR backscatter, emissivity, etc. changes abruptly [1,2]. The cause(s) of the 'snow line' have been controversial [2, 10-17], and most commonly

ascribed to the presence of semiconductor compounds (e.g., Te, PbS, BiTe) deposited from the atmosphere [12,13], or formed by rock reactions with the atmosphere (i.e. pyrite FeS_2 or magnetite Fe_3O_4) [14,15]. Variations in radar properties have also been ascribed to the presence/absence of ferroelectric substances like WO_3 or perovskite $CaTiO_3$ [18,17,16].

Results: Our results confirm earlier reports on the sharp increase in SAR backscatter (and decrease in radar emissivity) with increasing elevation up Maxwell Montes [1,Figs. 1,2]. In the analyzed swaths on the north flank of Maxwell, the drastic increase/decrease in backscatter/emissivity is at ~5 km, creating a "snowline" [Figs. 1,2]. The SAR-bright "snow" continues up to ~7.5 km elevation, above which backscatter/emissivity decreases/increases to values that are intermediate between those of the "snow" and the lowland plains [Fig. 3]. On the south flank of Maxwell, a "snow line" is still present at ~5 km elevation [Fig. 1]; above that, there are no clear relationships between elevation and radar properties [Fig. 3].

Discussion: Many conflicting theories have been offered to explain the radar properties of Maxwell Montes. However, these studies lumped data all across Maxwell, and thus had obscured local and regional trends in radar properties. By looking at a single swath and dividing it approximately by latitude [Fig. 3], we see that the 'snow line' on northern Maxwell is actually a gradual (albeit steep) change in radar properties over ~1 km elevation. On southern Maxwell, however, radar properties vary nearly independently of elevation [Fig. 3].

Of particular interest is that radar properties at the highest elevations on Maxwell are not those of the 'snow', but are intermediate between those of the 'snow' and the lowland plains. This change in radar properties at ~8 km (to lower backscatter & higher emis--sivity; Fig. 3), however, has rarely been discussed [17]. This transition does not happen at a constant elevation [17], and so could represent differences in lithology or to roughness of the mountainous topography [3,9].

On the studied swaths across Maxwell, radar properties are different north and south of the mountain crest (north- & south-facing slopes; Fig. 3). The cause(s) of this difference could be different rock materials or differences in atmospheric conditions. For the latter, we note that Venus' atmosphere has downwelling polar vortices [18], which could induce equator-ward meridional flow at low elevations [19]. If such a flow impinged on Maxwell, it might produce a "rain shadow" effect, with different conditions on north- and south-facing sides of Maxwell.

Festoon Flow: The Festoon Flow lies on the tessera terrain of central Ovda Regio [9,20,21,21, Fig. 4]. It covers an area of 53 km^2, and is up to 200 m thick at its margins. The Flow's surface shows large-scale ripples (festoons), and a complex series of overlapping flow lobes. The Flow straddles the elevation at which SAR backscatter decreases precipitously [1,9]. It post-dates nearly all faulting and deformation that affected the surrounding tessera. The Flow has been interpreted as representing a rhyolite (silicic) lava [20], which could suggest that the underlying tessera material is also silicic.

Results: The Festoon Flow is complex, with an intricate lobate margin, apparent flow fronts on the flow surface, kipukas exposing tessera material, and arcuate ridges (festoons). The flow margins are consistent with a fractal dimension of 1.26±0.07 (1σ) [8], see Fig. 4.

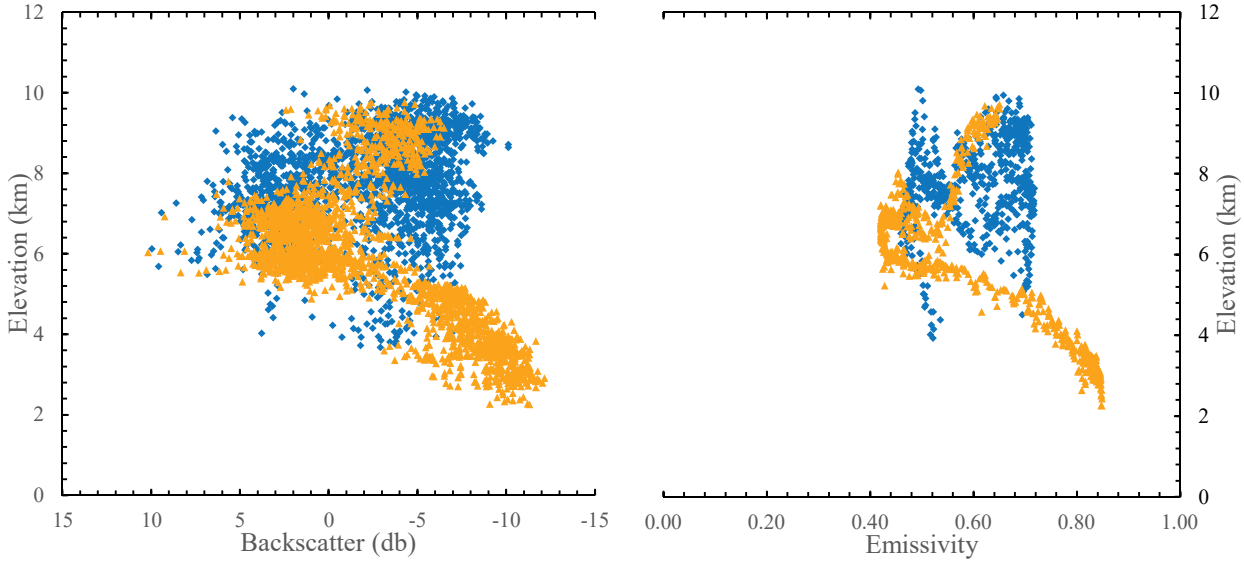

Figure 3: Backscatter (Left) and Emissivity (Right) vs. Elevation of Maxwell Montes. Orange symbols are for polygons north of the mountain crest, blue symbols are for polygons south of the mountain crest.

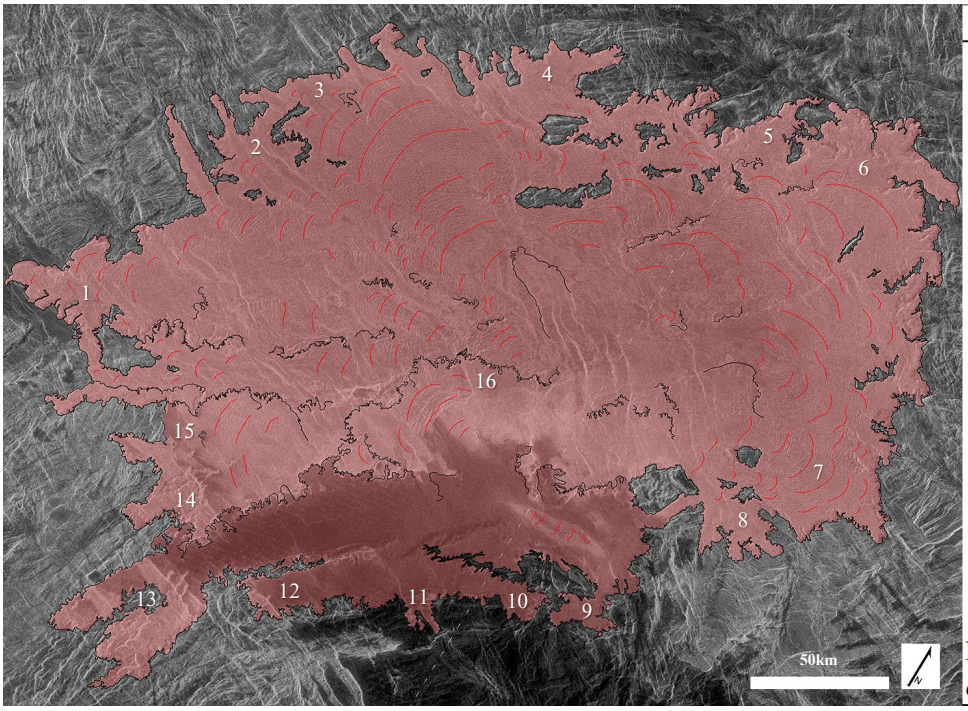

Lobe	D	R^2
1	1.22	0.88
2	1.28	0.98
3	1.28	0.98
4	1.15	0.94
5	1.21	0.98
6	1.28	0.91
7	1.25	0.98
8	1.18	0.97
9	1.30	0.94
10	1.25	0.99
11	1.42	0.97
12	1.20	0.97
13	1.22	0.94
14	1.39	0.85
15	1.30	0.99
16	1.21	0.97
Mean D	1.26	
σ	0.07	

Figure 4: (Left) Geologic map of the Festoon Flows. The mapped flow is in pink, with black lines showing recognizable flow margins. Red lines indicate 'festoon' flow folds orientated perpendicular to flow direction. Numbers denote flow lobes that were analyzed for fractal dimension (D). See table to right. R^2 is goodness of linear fit to the fractal dimension (D).

Elevations across the flow, from stereo DEM, show that the northern margin is ~200 m tall, the flow center is depressed ~500m from the margin, and that the southern edge of the flow (SAR-dark portion) is at higher elevations than the rest.

Discussion: The Festoon Flow has been considered to be of silicic (rhyolite) lava [9,20,21,22], but our data are more consistent with basaltic pahoehoe. Rhyolite flows have very high SAR backscatter compared to most deposits [25], and the Flow has backscatter similar to the surrounding tessera. Rhyolite flow margins are not fractal [8], while the Festoon Flow's margins are fractal with a dimension consistent with basalt. Festoons are common on silicic lava flows, but are also common on large thick basalt flows [23].

Flow direction may be defined by the convex of the festoons [Fig. 4]. Festoon orientations across the Flow are consistent with a single vent location (center of concave festoon directions), at high elevation near the Flow's south-east margin [Fig. 4].

The low elevation of the flow's center could be a result of flow inflation and then collapse. The overlapping of flow fronts atop the "main" flow itself may represent rootless flows constrained by the underlying topography [23,24, Fig. 5]. This could explain the density of flow margins to the south, where increased elevations (blocky terrain) would serve as levees for lava flows, and accumulate volume until failure would occur and flow out again, appearing as gradients within SAR [19,20].

References: [1] Treiman A.H. et al. (2017) *Icarus, 280,* 172-182. [2] Campbell et al. (1999) *J. Geophys. Res., 104,* 1897-1916. [3] Gilmore M.S. and Head J.W. (2018) *Planetary and Space Science, 154,* 5-20. [4] Herrick R. R. et al. (2012) *EOS, Transaction, AGU, 93(12),* 125-126. [5] isis.astrogeology.usgs.gov [6] Arvidson R.E. et al. (1994) *Icarus, 112,* 171-186. [7] Byrnes and Crown (2002) *J. Geophys. Res., 107, N.E10,* 5079. [8] Bruno et al. (1994) *Bul. Volcan., 56,* 193-206. [9] Campbell D. and Burns B. (1980) *J. Geophys. Res., 85,* 8271-8281. [10] Klose K. et al. (1992) *J. Geophys. Res.,* 16353-16369. [11] Pettengill G.H. et al. (1992) *Science 272,* 1628-1631. [12] Brackett, R.A. et al. (1995) *J. Geophys. Res., (91-12), 100,* 1553-1563. [13] Kohler E. et al. (2015) *LPSC XXXXV,* Abstract #2563. [14] Pettengill G.H. et al. (1996) *J. Geophys. Res., 97,* 13091-13102. [15] Fegley B. et al. (1997) *Venus II Geo., Geophys., Atmos., and Solar Wind Env.,* 591-636. [16] Fegley B. and Treiman A.H. (1992) *Venus and Mars: Atmos., Iono., and Solar Wind Int., 7-71.* [17] Wood J.A. and Klose K.B. (1991) *LPSC XII*, 1521-1522. [18] Garate-Lopez I. et al. Nature Geoscience, 6(4), ngeo1764. [19] Lebonnois, S. et al. (2016) *Icarus*, *278*, 38-51. [20] Schenk P. and Moore H.J. (1992) *LPSC XXIII,* Abstract #1597. [21] Permenter J.L. & Nusbaum R.L. (1994) LPSC XXV, 1067-1068. [22] Head J.W. & Hess P.C. (1996) LPSC XVII, 513-514. [23] Bleacher J.E. et al. (2017) *J. Volc. And Geother. Res., 342,* 29-46. [24] Chevrel M.O. et al. (2013) *Earth and Plan. Let., 384,* 109-120.

Notes

Notes

LPI Summer Internship Program in Planetary Science
Orientation - June 4, 2018

Lunar Curation - The lunar sample laboratory is where pristine lunar samples are prepared for shipment to scientists and educators. Nearly 400 samples are distributed each year for research and teaching projects.

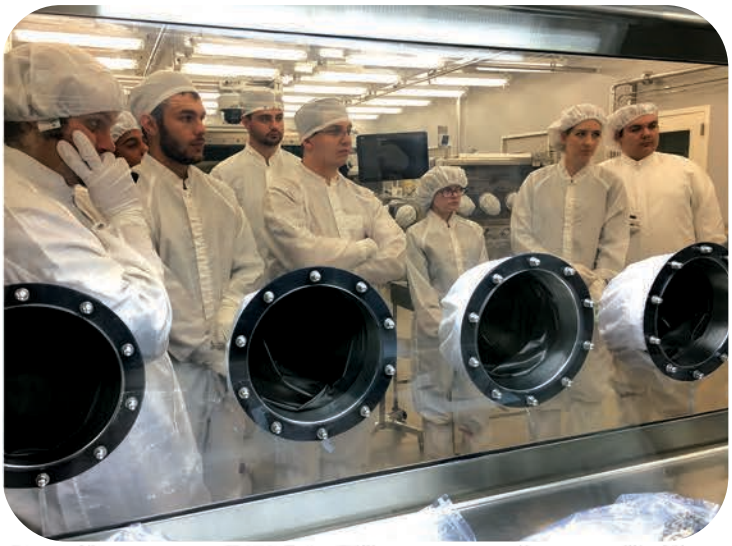

Stardust - a NASA Discovery-class mission, was the first to return samples from a comet and from interstellar space.

Genesis - Was a NASA sample-return probe that collected a sample of solar wind particles and returned them to Earth for analysis.

June 4, 2018

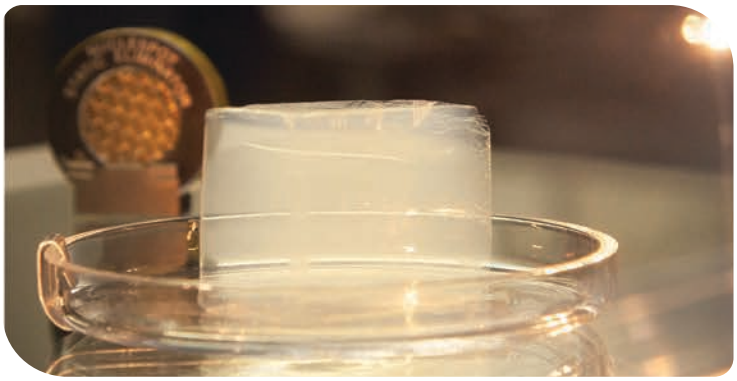

Meteortie Lab - The curation and collection of Antarctic meteorites is a U.S. funded, cooperative effort among NASA, the National Science Foundation and the Smithsonian Institution. Meteorites of greater interest and undergoing detailed study are kept at JSC for distribution to the scientific community, but irons are sent directly to the Smithsonian Institution.

June 28, 2018

Human Exploration Research Analog (HERA) is a unique three-story habitat designed to serve as an analog for isolation, confinement, and remote conditions in exploration scenarios.

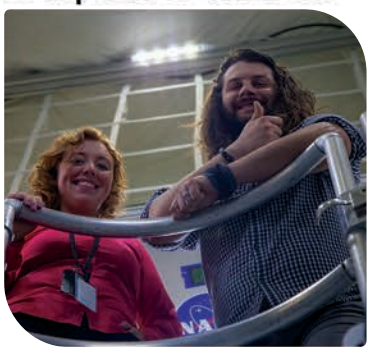

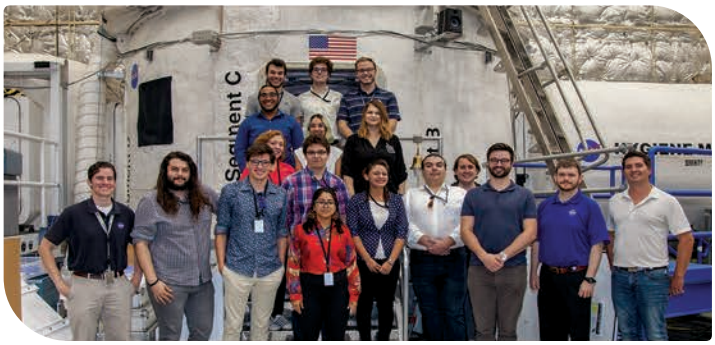

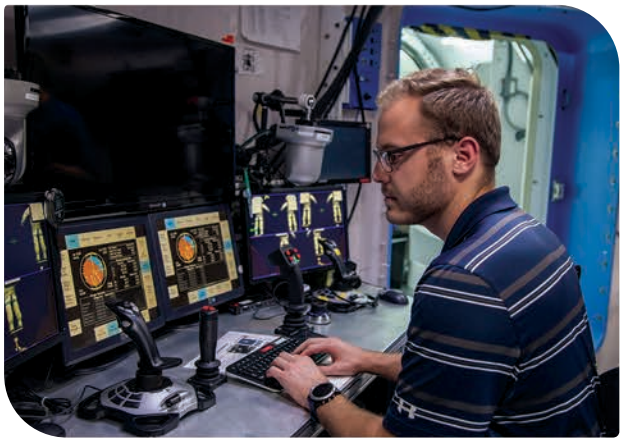

The Neutral Buoyancy Laboratory (NBL) is one of the world's largest indoor pools and can support multiple large scale operations utilizing both underwater and topside assets simultaneously. The NBL is utilized for mission planning, procedure development, hardware verification, astronaut training, and refinement of time-critical operations necessary to ensure mission success during spacewalks.

July 20, 2018

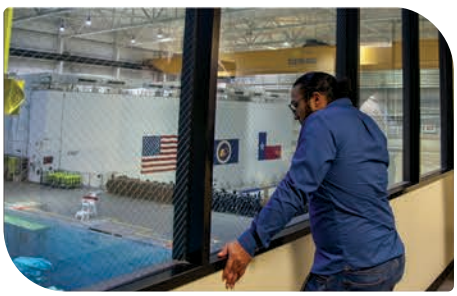






The full fleet of NASA crewed vehicles Orion, Crew Dragon and CST-100 Starliner mock-ups will be together in the Space Vehicle Mockup Facility and the Ascent Abort-2 (AA-2) hardware developed for the full-stress of Orion's Launch Abort System. This is the actual vehicle that will be launched in April 2019.

August 2 & 3, 2018



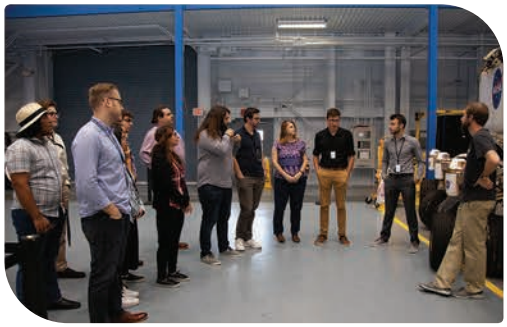





Mid-term reviews. July 6, 2018






Professional Development Seminar Series:
How to give a Science Talk

July 31, 2018



Preparing for upcoming conference.


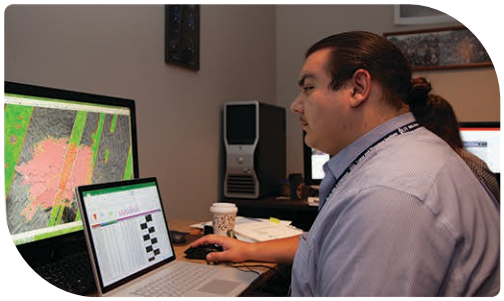


LPI Summer Interns 2018

Yoana Bolenga
Advisor: Goodrich
LPI Intern

Nathan Hadland
Advisors: Rampe, Tu / JSC
LPI Intern

Alexander Holmwood
Advisor: Righter / JSC
LPI Intern

Elisha Jhoti
Advisor: Liu
LPI Intern

Ethan Kuehl
Advisors: Jones, Castle
LPI Intern

Andy Lopez-Oquendo
Advisor: Rivera-Valentin
LPI Intern

Devin McQuaig
Advisors: Simon, Middlefehldt, Armytage / JSC
LPI Intern

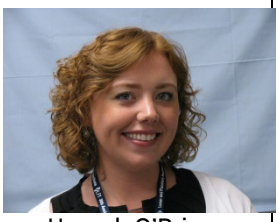

Hannah O'Brien
Advisors: Kring, Robinson
LPI Intern

Jacob Ott
Advisors: Rampe, Morris / JSC
LPI Intern

Mitzi Cruz Quijano
Advisors: Prockter, Kay
LPI Intern

Stephen Slivicki
Advisors: Kring, Schmieder
LPI Intern

Federico Stachurski
Advisors: Treiman, Liu
LPI Intern

Nicholas Wagner
Advisors: Schenk, Kay
LPI Intern

Frank Wroblewski
Advisor: Treiman
LPI Intern